A Hydrothermal Model for Metasomatism of Neoarchean Algoma-Type Banded Iron Formation to Massive Hematite Ore at the Soudan Mine, NE Minnesota

A Thesis

SUBMITTED TO THE FACULTY OF THE

UNIVERSITY OF MINNESOTA

BY

Adam Thompson

IN PARTIAL FULFILLMENT OF THE REQUIREMENTS

FOR THE DEGREE OF

MASTER OF SCIENCE

Adviser: Howard Mooers

Co-Advisers: Phil Larson, George Hudak

February, 2015

Acknowledgments

The author would like to thank his advisor, Dr. Howard Mooers and co-advisors Drs. George Hudak, and Phil Larson at the University of Minnesota Duluth. Thanks are also extended to Drs. Christian Schardt and David Saftner for serving on the advisory committee. Special thanks go out to Jim Essig (Park Manager), James Pointer (Interpretive Supervisor), and the entire mine interpreter crew at the Soudan Underground Mine State Park. Jim facilitated access to the mine and provided the resources needed for reconnaissance mapping and sample collecting. James and the interpreter crew provided training and acted as guides during trips down the mine.

Conversations between the author and other graduate students at the University of Minnesota Duluth were very beneficial to the writing of this thesis. Thank you to Paul Fix and Michael Doyle for your insights and genuine interest in this project.

The author would also like to thank the Society of Economic Geologists (SEG) for partially funding this project.

Most importantly, the author would like to thank his parents for always giving support and encouragement during their son's academic endeavors.

Abstract

The genesis of banded-iron-formation (BIF) hosted massive hematite ore deposits has been debated extensively in the literature. Recent advances in exploration and analytical techniques have led to a better understanding of the tectonic setting and characteristic hydrothermal fluids responsible for the metasomatic upgrading of BIF to hematite ore and associated wall rock alteration. As late as the 1990's the general consensus was that the massive ore-bodies observed in the Carajas District, Brazil, and the Hammersley Province of Western Australia, among others, formed predominantly through supergene processes responsible for silica leaching and magnetite oxidation to hematite within BIF during the Mesozoic (Hagemann et al., 2007). The relatively young age for the genesis of massive hematite ore was brought into question by Martin et al. (1998) through SHRIMP U-Pb age dating of zircons from volcaniclastic breccias of the Wyloo Group, which provided an age of 2209 +/- 15 Ma for hematite detritus of the Hammersley province. Ohmoto (2003) provided an alternative mechanism for oxidation by the reaction:

$$Fe_3O_4(mt) + 2H^+ \leftrightarrow FeO(hm) + Fe^{2+} + H_2O$$

the leaching of Fe^{2+} from magnetite by an acidic hydrothermal fluid. The enrichment and conversion of magnetite-dominant BIF to massive hematite through an acid-base reaction is of particular significance for Algoma-type BIF-hosted massive hematite deposits such as that at the Soudan Mine in northeastern Minnesota. It has been generally accepted that the hematite ore at Soudan is a product of D_2-shearing and subsequent hydrothermal activity active within the Mine Trend Shear Zone formed during the accretion of the Wawa-Abitibi terrain to the Superior Craton at ~2685-2690 Ma. The lack of a weathering profile (evidenced by supergene goethite) and the relatively low permeability and high specific gravity of Soudan ore relative to supergene ores precludes descending, oxygenated meteoric fluids driving alteration and mineralization of the massive hematite ores. Rather, a model of early calcic-sodic alteration during mature-arc rifting with progressive burial during subduction of the Wawa-Abitibi Terrane leading to potassic and Fe/Mg metasomatism is proposed here. Wall rock alteration assemblages, associated with the upgrading of magnetite-chert BIF through magnetite-siderite and hematite-ankerite precursor to massive hematite ore, is associated with early sericite (± paragonite), silica, and Mg-rich chlorite, with local secondary sericite, hematite, and Fe-enriched chlorite. Isocon analysis indicates a volume loss of 39% due to the leaching of silicate minerals from BIF, consistent with Fe-enrichment by silica subtraction, and breccia textures observed in massive hematite ore. LREE-

enrichment of wall rock adjacent to ore is observed, perhaps resulting from monazite precipitation of elements released due to the breakdown of apatite within the BIF. Late stage alteration appears to be post-D_2 and is associated with precipitation of microplaty hematite as breccia cement, as well as secondary Fe-enriched chlorite replacing earlier potassic alteration. This late alteration stage shows HREE-enrichment with a strong positive Eu anomaly for both the chlorite schists wall rock enveloping hematite ore, and the massive hematite ore.

Table of Contents

List of Figures

List of Tables

Introduction

The Soudan Member of the Ely Greenstone Formation is largely composed of Neoarchean age, Algoma-type iron formation that extends from east of Ely, Minnesota westward to Tower, Minnesota. While primarily being composed of laminated to medium-bedded magnetite-hematite-jasper-chert deposits, locally, in proximity to east-west trending, steeply dipping faults, the iron formation has been modified to semi-massive to massive hematite lenticular bodies. These hematite-bearing bodies were the first iron-ore mined in Minnesota at the Soudan Mine, which operated from 1882-1962. Mining operations began with surface open-pit mining, while transitioning to an underground operation down to a depth of ~ ½ mile. Similar hematite bodies were exploited in northeastern Minnesota until the late 1960s at other mines (e.g. Pioneer, Sibley, and Chandler in Ely). Although reserves at the Soudan Mine extend down to greater depths than the most recently developed and mined 2700 Level, advances in steel refining processes led to development of open pit taconite mining operations utilizing large, low grade, Middle Proterozoic age taconite bodies on the Mesabi Range. Such large scale open pit mining operations made underground mining of the Neoarchean massive hematite orebodies at Soudan and other northeastern Minnesota locations uneconomical. This led to closure of all Algoma-type mining operations in northeastern Minnesota by the late 1960s.

The Vermilion District massive hematite ore occurrences represent an anomalous group of ore deposits within the Canadian Shield. Since the exploitation of these ore bodies drew to a close in the 1960s, geological research attempting to explain the orogenic processes and associated hydrothermal fluids responsible for hematite ore genesis within the Vermilion District also came to an abrupt end. As a result, the genesis of the Neoarchean age massive hematite bodies in northeastern Minnesota continues to remain poorly understood. This thesis, which comprises field mapping along with petrographic and geochemical studies, has been designed and performed to better constrain the genesis of the massive hematite bodies at the Soudan Mine.

Previous studies at Soudan

Schwartz and Reid (1954) analyzed multiple sections of drill core deemed to represent the least altered greenstone within the Soudan Mine. They compared the geochemistry of these 'least altered greenstones' to that of unaltered Ely Greenstone in the area as well as with samples consisting of both sericite 'soap rock alteration' and hematite 'paint rock alteration'. They found that, relative to the unaltered Ely Greenstone within the Vermilion District, the least altered basalts of the Mine Trend Shear Zone show an increase in ferrous iron content by two to three times in terms of weight percent. Silica is also depleted relative to unaltered Ely Greenstone, and water content is doubled. A comparison of the least altered basalt to a sample altered to hematite 'paint rock' shows a further increase in iron content, but consisting predominantly of ferric iron (Schwartz and Reid 1954). They suggest this is due to Fe-rich chlorite being oxidized to hematite. Schwartz and Reid (1954) state that the sericite alteration poses a problem in that its close association to the Soudan Mine area indicates that sericite is a product of altered greenstone, but the geochemistry (low Fe and Mg) suggest a rhyolitic source rock.

Klinger (1960) observed three primary types of chlorite at the Soudan Mine. Magnesium rich clinochlore and penninite are the dominant type with lesser amounts of Fe-chlorite he deemed thuringite based on Hey's (1954) classification scheme (Figure 1). Klinger notes the striking contrast between the greenstone at Soudan and the unaltered Ely Greenstone; most notably, he notes the high amount of sericite and quartz and lack of calcic minerals within altered rocks associated with the Soudan Mine versus the relatively unaltered Ely Greenstone. Klinger also observed secondary chlorite replacing sericite and chlorite in the vicinity of ore, which he suggested may have been a product of iron mobility associated with ore formation.

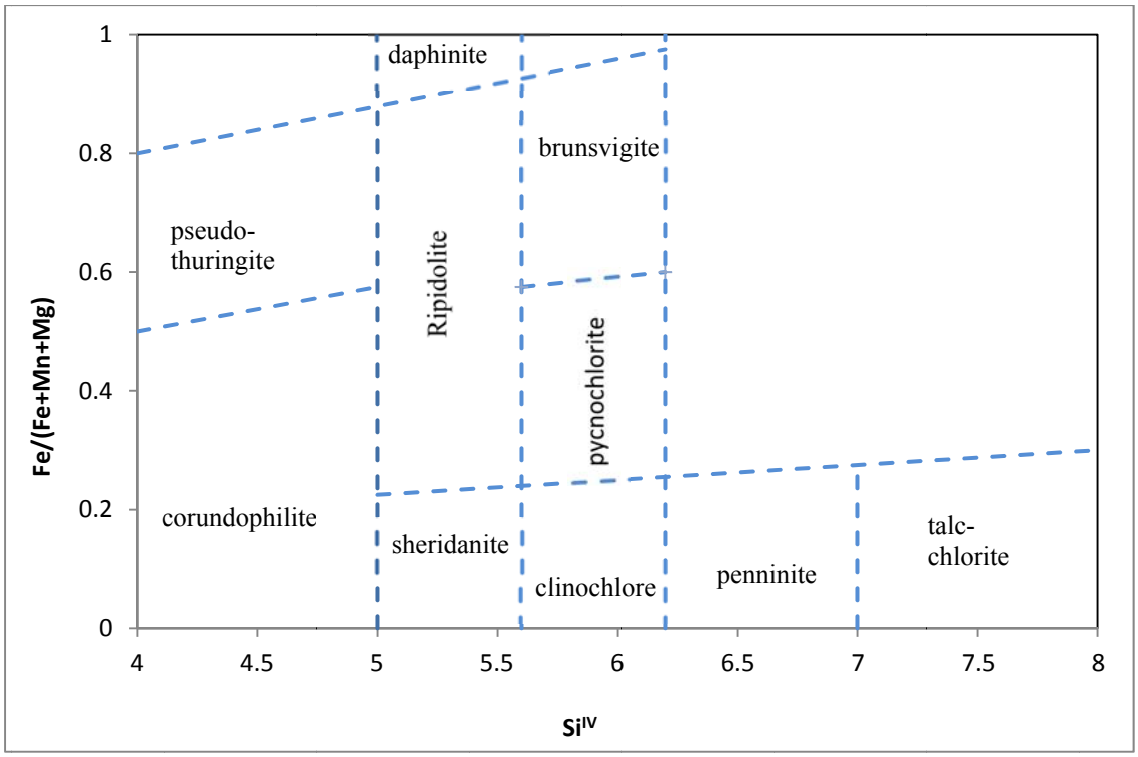

Figure 1. Compositional diagram for unoxidized chlorites that shows Si content versus Fe/Mg content in chlorites in wt% (Hey, 1954).

Statement of Problem

Through the work of Klinger (1960), Schwartz and Reid (1954), and others, it is generally understood that the BIF-hosted massive hematite ore at Soudan was formed by the removal of silica from the protore BIF with possible Fe-enrichment by hydrothermal fluids that were largely confined to steeply dipping regional shear zones in the Vermilion District. The sources and characteristics of these hydrothermal fluids have remained enigmatic.

At Soudan, large-scale surface and underground mapping has been conducted by Peterson and Patelke (2003), and students from the Precambrian Research Center (PRC) through the University of Minnesota Duluth (Radakovich et al., 2010; Vallowe et al., 2010; Heim et al., 2011). General alteration assemblages recognized by Schwartz and Reid (1954) have been mapped, but little work has been conducted to define the paragenetic sequence(s) associated with the upgrading of the Soudan BIF to massive hematite ore.

The focus of this study is to utilize detailed geologic mapping data from around the Montana Ore Zone on the 27th level of the Soudan Mine, along with petrographic and geochemical analyses of

the metavolcanics, oxide-bearing ore rocks, and oxide-bearing non-ore banded iron formations to define a paragenetic sequence for the formation of massive hematite ore at Soudan. Whole rock major and trace element lithogeochemical analyses of selected samples have been utilized to understand the chemical and volumetric aspects of hydrothermal alteration associated with the massive hematite bodies in an effort to better constrain the geochemical processes related to hydrothermal metasomatism associated with the genesis of the hematite ores. Algoma-type BIF-hosted hematite ore occurrences have been characterized at the Carajas District in Brazil and the Koolyanobbing Greenstone Belt in Western Australia through petrographic, geochemical, isotopic, and fluid inclusion analyses (Angerer et al., 2010; Figueiredo e Silva et al., 2013), however no single model can be used to accurately characterize hematite-ore occurrences worldwide.

Regional Geology

The Vermilion Greenstone Belt (VGB) occurs at the western end of the Wawa-Abitibi suprovince (Stott and Mueller, 2009) in northeastern Minnesota. It is divided on the basis of stratigraphic and structural setting into the Soudan Belt to the south, and the Newton Belt to the north (Peterson et al., 2001). The boundary between the two belts is marked by the Mud Creek shear zone and the Knife Lake Group (Figure 2). The Soudan Belt comprises the Ely Greenstone Formation, the Lake Vermilion Formation, and the Knife Lake Group. The Ely Greenstone Formation has been subdivided into three separate units. From stratigraphically oldest to youngest, these comprise: 1) the Lower Ely Member, which comprises the lower Fivemile Lake Sequence and upper Central Basalt sequences (Peterson and Patelke, 2003; Hudak et al., 2012), and is composed of calc-alkalic and tholeiitic pillowed to massive subaqueous basalt lava flows, massive, locally quartz +/- plagioclase-phyric-rhyolite lava flows, mafic to felsic tuffs and associated epiclastic rocks, and minor iron formations; 2) the Soudan Member, which is predominantly composed of laminated to medium-bedded Algoma-type magnetite-hematite-jasper-chert banded iron formations and local interbedded mafic to felsic lava flows and volcaniclastic rocks; and 3) the Upper Ely Member, composed of massive to pillowed tholeiitic basalt lava flows and minor intercalated Algoma-type iron formations (Peterson and Patelke, 2003; Hudak et al., 2007; Hoffman, 2007).

The Soudan Iron Formation is the predominant lithology within the Soudan Member of the Ely Greenstone Formation. The lower contact of the Soudan Iron Formation contains interlayered basaltic lava flows representing a transition to a period of volcanic and tectonic quiescence during

the deposition of the Soudan BIF. A gradational contact, occurring over several tens to a few hundreds of meters up, exists along the basal contact of the Soudan Member BIF and Lower Ely basalts (Hudak et al., 2007, 2012). The transition is marked by a decrease in the abundance of basalt lava flows and associated volcaniclastic rock, and an increase in the abundance and thickness of oxide-facies iron-formation horizons, moving towards the basal contact of the Soudan Member (Hudak et al., 2002b; Peterson and Patelke, 2003; Hudak et al., 2007; Hoffman, 2007; Hudak et al., 2012). Hudak and Peterson (2014) provide evidence for the deposition of the Soudan Member in a relatively quiet, deep subaqueous environment (>200 m and probably greater than 1400 m). This evidence includes:

1) the absence of primary mafic and felsic pyroclastic deposits within the stratigraphic sequence
2) a lack of multiple-selvage pillow lavas in the stratigraphic sequence
3) BIF stratigraphy dominated by planar laminations and bedding and lacking any wave-associated sedimentary bedforms
4) lithological and geochemical evidence for the development of an extensional tectonic environment, resulting in the deepening of the depositional environment for the uppermost sections of the Lower Ely basalts (Hudak and Peterson, 2014).

Stratigraphically overlying the Soudan Member BIF is the Upper Ely Member, which is composed of MORB-like basalts that consist of poorly vesicular to massive basalt pillows and sheet flows and associated mafic/felsic volcaniclastic rocks (Hudak and Peterson, 2014). Some mafic intrusives that occur within the Soudan Member have been interpreted as feeder dikes and synvolcanic sills associated with the genesis of the Upper Ely lava flows.

The nature of the geological contact between the Soudan Member and overlying Gafvert Lake Sequence felsic volcanic and volcaniclastice rocks, as well as the Upper Ely Member mafic volcanic and volcaniclastic rocks, remains in many places poorly constrained. Within Lake Vermilion State Park, approximately three kilometers northeast of the Soudan Mine headframe, detailed geologic mapping combined with geochronological studies now clearly show that the upper contact of the Soudan Member and overlying Gafvert Lake Sequence is an unconformity (disconformity). Lodge (2013) has analyzed the dacitic tuff breccia deposits which occur immediately north of the Soudan Member, and has obtained a U-Pb age of approximately 2690 Ma for these felsic volcaniclastic rocks.

The Soudan Mine area is characterized by two regional structural features: (1) the steeply west-plunging, overturned Tower-Soudan anticline, which has been interpreted to have formed during

D_1 compression; and (2) steep shear fabrics associated with the Murray and Mine Trend Shear Zones interpreted to have formed from D_2 transpressional shearing during accretion of the Wawa subprovince onto the Superior Craton (Peterson, 2001). There is also a third deformation event responsible for significant NE- and NW-trending faults that dissect the stratigraphic assemblages (Hudak et al, 2007). D_2 deformation is dated at 2674-2685 Ma based on regional penetrative metamorphic fabric (Boerboom and Zartman, 1993; Lodge et al., 2013).

Prior to D_1 compressional and D_2 transpressional deformation, synvolcanic hydrothermal alteration of the Lower Ely and Soudan Member took place. Subseafloor hydrothermal convections resulted in regional semiconformable alteration zones within the Lower Ely Member that are composed of quartz, epidote, zoisite/clinozoisite, Fe-chlorite, Mg-chlorite, actinolite, ferroactinolite, sericite/pyrophyllite, and albite (Hudak and Morton 1999; Odette et al. 2001; Peterson 2001; Hudak et al. 2002a). Pipe-like, northeast trending, disconformable alteration zones associated with VMS prospects have also been mapped in the area and consist of Fe-rich chlorite, sericite/pyrophyllite, actinolite and/or ferroactinolite (Peterson, 2001; Hudak et al., 2002a; Hocker et al., 2003).

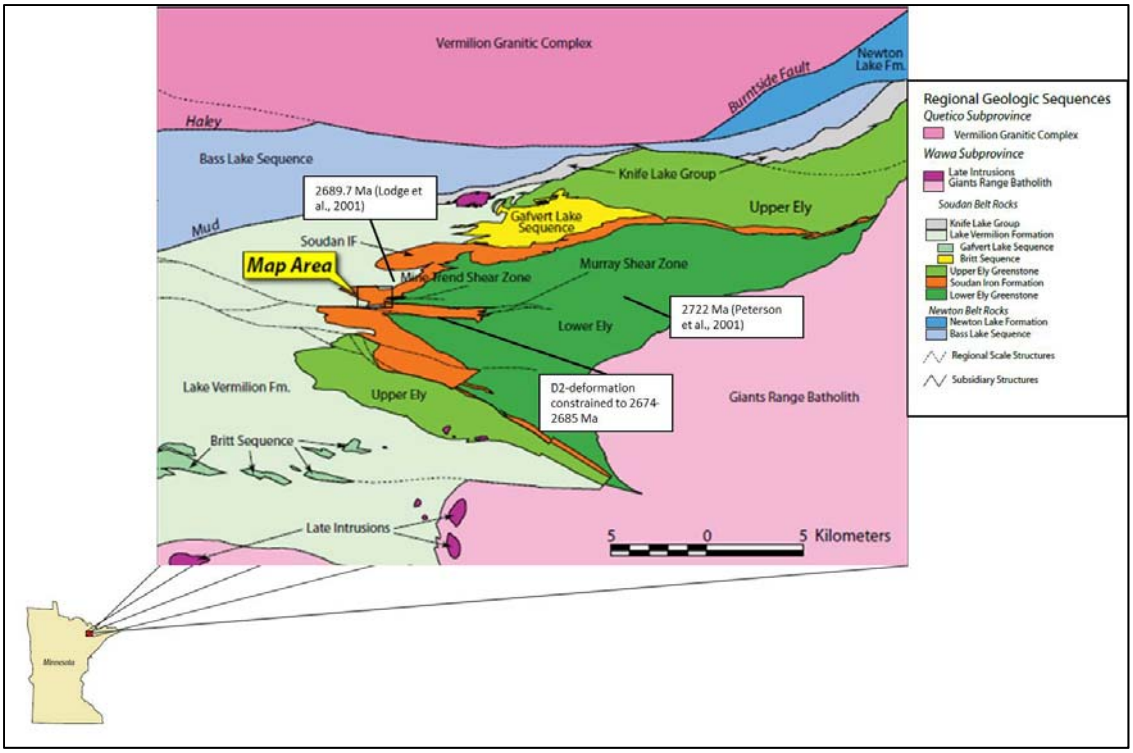

Figure 2. Regional geologic map of the western Vermilion Greenstone Belt (VGB). Modified from Peterson and Patelke (2003) and Hudak and Peterson (2014). Inset shows Soudan Underground State Park area mapped by Peterson, Patelke, and PRC students in 2010 shown in Figure 3.

Geology and Alteration at the Soudan Mine

The massive hematite ore of the Soudan Mine comprises a series of sub-vertical, elongated pockets of ore within the host Soudan Member banded iron formation protore. The hematite ore at Soudan lies along the north limb of the overturned, east-west trending Tower-Soudan anticline within the Mine Trend Shear Zone.

Rock units within the Soudan Mine predominantly consist of sericite- and chlorite-altered basaltic flows, hematite/jasper banded iron formation, and a heterolithic series of intercalated schistose rocks composed of chlorite schist, sericite schist, and jasper iron formation colloquially known as Schist 'n' BIF. Late intrusive rocks include a greyish-green to black, medium-grained, massive gabbro that exhibits a weak east-west fabric, and black to dark green, fine-grained diabase, both of which have been interpreted as feeder dikes to overlying volcanic strata (Peterson and Patelke, 2003). These intrusives commonly occur proximal to hematite ore (Klinger, 1961). Alteration

within the Soudan Mine is dominated by chlorite and sericite (Figures 3 and 4), with later hematite overprinting these locally near hematite ore.

Based on geologic mapping and samples collected for this project and historical geochemistry data from the Minnesota Department of Natural Resources (Dahlberg et al., 1989), there appears to be a transition within the banded iron formation from hematite/martite jasper BIF at depth to magnetite/siderite/chert BIF near the surface. Concurrent wall rock alteration transitions from a complete lack of calcium at depth (22-, 23-, and 27-levels) with increasing carbonate content and significant calcite stringers proximal to banded iron formation near the current surface. A silica-rich zone (70-80 wt%) is associated with mylonitic sericite/silica schists occurring along the margins of ore breccia zones. These zones of high deformation also show levels of sodic alteration (paragonite?) with Na_2O concentrations ranging from~ 1-4 wt%.

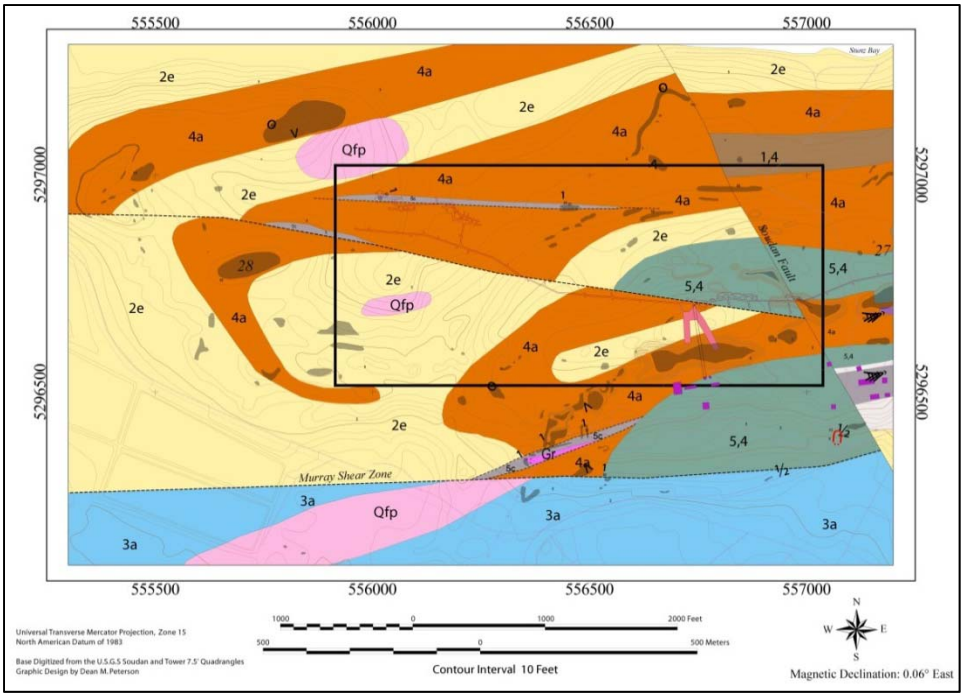

DESCRIPTION OF MAP UNITS

SHEARED ROCKS - Diverse series of curvilinear bands of schistose rocks found along discrete ductile to brittle-ductile structures.

5s Sericite Schist [5s] – Pale yellow-green to gray, very fine- to fine-grained, sericite schist.

5cs Chlorite-Sericite Schist [5cs] - Yellowish-green, fine-grained, highly foliated chlorite-sericite schist. A very distinctive map unit underground recognized by its color and high degree of deformation.

5c Chlorite Schist [5c] - Green to dark-green, very fine- to fine-grained chloritic schist.

5f Fragmental Schist [5f] - Green, medium-grained, foliated chlorite-sericite schist with distinctive 1-10cm stretched fragments of dacitic volcanic rocks. The protolith of this unit is interpreted to have originally been pyroclastic tuff breccia and/or debris flow deposits of the Gafvert Lake Sequence and or Map Unit 2e (lapilli tuff).

5,4 Schist 'n' BIF [5,4]- Complex series of schistose rocks composed of interlayered chlorite schist, sericite schist, and oxide facies iron-formation.

INTRUSIVE ROCKS - Intrusive rocks in the map area span the Late Archean geologic history of the immediate area from syn-volcanic (hypabyssal dikes and sills of mafic to felsic composition), syn-tectonic (felsic porphyry dikes), and post-tectonic (enigmatic lamprophyric bodies immediately east of the map area) timing. The timing of the intrusive rocks is based strictly on field observations of the D_2 fabric and very localized geologic setting.

Gr Granite [Gr] - Pink, medium-grained, biotitic-granite.

Qfp Quartz-Feldspar Porphyry [Qfp] - White to whitish-pink, medium-grained rock with sub-rounded white feldspar and clear to white quartz phenocrysts in a fine-grained quartzofeldspathic + mafic groundmass.

Gb Gabbro [Gb] - Dark green to black, fine- to medium-grained, equigranular and homogeneous gabbro consisting of chlorite-feldspar ± quartz ± calcite and trace pyrite.

UPPER SEQUENCE - Diverse series of rocks units associated with the Soudan Iron Formation and Lake Vermilion Formation. Series dominantly consists of tuffaceous and epiclastic rocks of dacitic composition and banded iron-formation. Basal units include basaltic rocks, and the whole sequence is overlain by deep water greywacke-argillite.

3a Greywacke [3a] - Grey, fine to medium grained, thin to medium bedded greywacke and slate. Outcrops occur south of the Murray shear zone on the southern margin of the maps.

2e Lapilli Tuff [2e] - Dirty white to light grey and in areas, sulfide stained , poorly bedded to massive.

1,4 Basalt and Iron-Formation [1,4] - Massive and foliated basaltic protolith rocks with lenses of cherty magnetic (and lesser hematitic) iron-formation.

4a Banded Iron-Formation [4a] - Dominantly thin-bedded (<1 mm up to 1 cm), interlayered jasper and steel-grey hematite.

Figure 3. Surface geology map of the Soudan Underground Mine State Park (Modified from Vallowe et al., 2010). Inset shows mapping of the western 27th level shown in Figure 4.

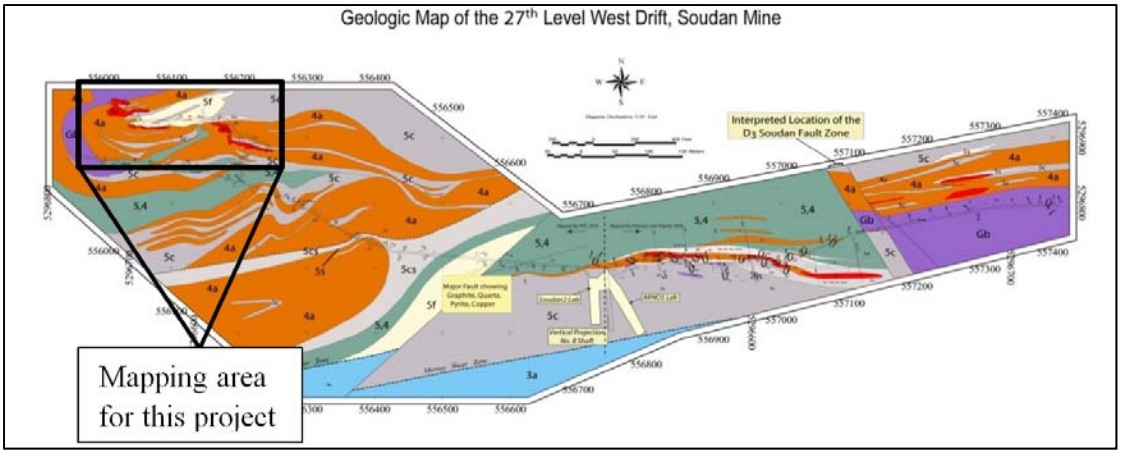

Figure 4. Geologic map of 27th level west end (after Peterson, Patelke, and PRC students, 2010). Map units correlate to units on surface map. Inset outlines Montana Ore Zone mapped for this project. Inset shows mapping area for this project.

Methods

Mapping

Mapping for this project was focused on the 2700 level of the Soudan Mine. Drift mapping consisted of laying out 50 foot (15.24 meter) sections with a tape measure in order to accurately define alteration zones of the meta-volcanics associated with the ore breccia zones. Major structures were mapped along with gradational changes within the oxide facies BIF. The drift was mapped starting at the eastern extent of the Montana Ore Zone down to the western stope area (Figure 5). Textural changes along major shear zones were also mapped to aid in formulating a sequence of wall rock alteration associated with the upgrading of jasper/hematite BIF to ore breccia.

Sampling

Results of mapping were used to target areas of less-altered rocks outside the breccia zones and altered rocks associated with the hematite ore zones. Transitions zones, shear zones, and oxide facies rocks were also sampled in an attempt to obtain a representative suite of rocks for both wall rock alteration and associated changes to the BIF and ore. A total of 60 hand samples were collected.

Analyses

Petrographic thin sections were prepared from selected hand samples by San Diego Petrographics (Emmett, Idaho). Petrographic analysis was performed to characterize the various lithologies

present in terms of mineralogy and textures. This included describing textural changes from the protore BIF to the micro-banded martite and microplaty hematite ores, as well identifying the alteration phases within the narrow shear zones in and around the massive ore lenses.

Based on the petrographic analyses, 44 samples were selected for geochemical analysis. Major element geochemistry for selected crushed hand samples was obtained by inductively coupled plasma atomic emission spectroscopy (ICP-AES) and trace element geochemistry, base metals, and REE through inductively coupled plasma mass spectrometry (ICP-MS). All samples were digested in 1:1:1 aqua regia prior to ICP-MS analysis, with sample sizes ranging 10-490 g. Analyses were performed by AcmeLabs of Vancouver, BC. The results of these analyses are given in Appendix B.

Based on mapping, petrographic, and geochemical data, a paragenetic sequence was developed to represent wall rock alteration associated with each oxide facies, from less-altered BIF through massive hematite ore. These stages of alteration were then used to select the samples used for the isocon analysis.

Grant's (1986) isocon method was used to define metasomatic changes associated with various alteration mineral assemblages in the wall rocks, BIF, and hematite ore. The results of these analyses are shown in Appendix C.

Selected samples were analyzed to determine chlorite compositions using scanning electron microscopy (SEM) at the University of Minnesota Duluth. Chlorite compositions of schists both proximal and intermediate to the hematite ore breccia zones were determined.

Results

Mapping and petrographic analysis in the Montana Ore Breccia Zones

Mapping for this study was focused around two ore breccia zones along the 27th level of the Soudan Mine; at (1) the Eastern Montana Cutback and (2) the stope area at the western extent of the Montana Ore Zone (Figure 5). Rock units outside the ore breccia zones consist predominantly of moderately foliated Schist n' BIF and fragmental schist (Gafvert Lake sequence protoliths), with sulfide stringers and disseminated sulfides occurring intermediate to ore zones along major shear contacts. Schist n' BIF consists of a complex series of foliated rocks composed of interlayered chlorite schist, sericite schist, and oxide facies iron formation, while the fragmental schist consists of foliated chlorite-sericite schist with distinctive 1-10 cm stretched

fragments of dacitic volcanic rocks (Peterson and Patelke, 2003). Alteration and deformation within these rock units has led to the development of chlorite- and sericite-schists. Along the margins of the sericite schists, remnant primary sericite/paragonite/silica alteration may be present. Adjacent to ore breccia, the sericite schists have been silicified as evidenced by their blocky/fractured texture, while within the ore breccia zones, BIF becomes increasingly hematized closer to the ore. Less altered BIF adjacent to silicified sericite schists contains significant en echelon quartz veining and smoky 'bull quartz' occurs in the brecciated BIF and ore as both veins and clasts. The BIF and ore breccia zones also contain significant amounts of micaceous chlorite and sulfides such as pyrite, pyrrohtite, and chalcopyrite. Chlorite lines vug walls containing quartz (Klinger, 1960) and occurs as veins in the ore, particularly near contacts with chlorite schist and hematite breccia zones.

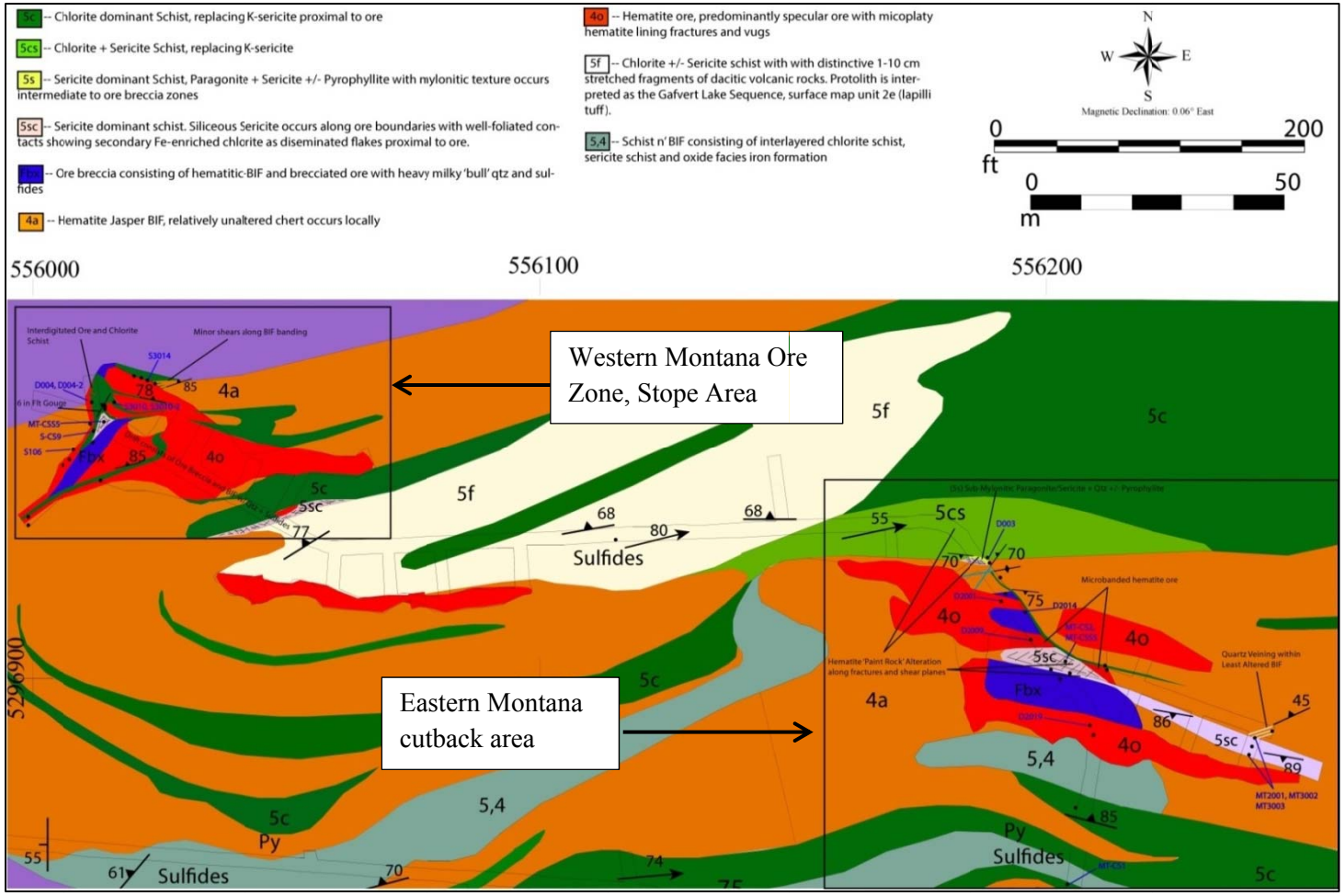

Figure 5. Montana ore zone map. Large-scale mapping conducted by Peterson, Patelke, and PRC students. Insets show areas of detailed mapping for this project shown in Figures 6 and 9.

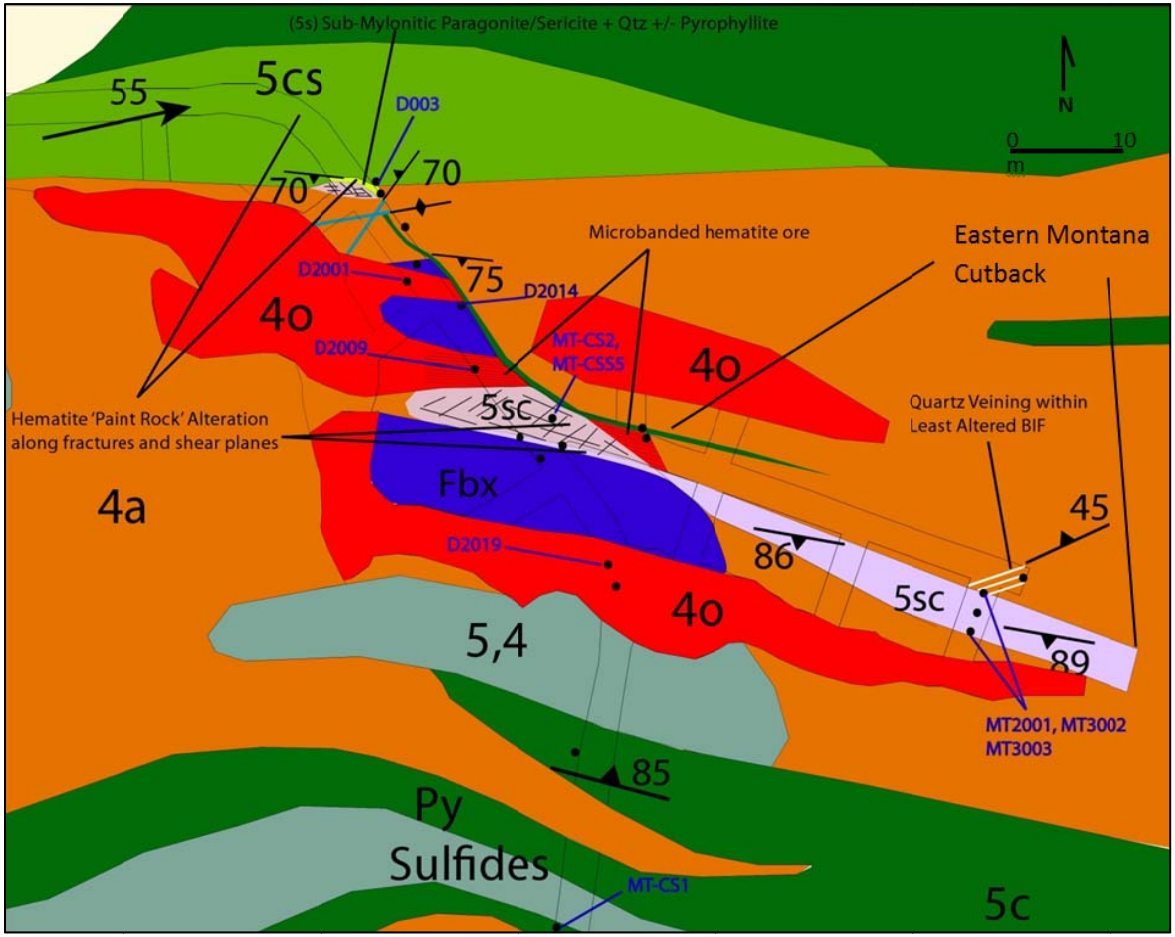

Figure 6. Eastern extent of the Montana Ore Zone. Sericite/chlorite schist (5sc) to the east along Montana cutback shows strong foliation in contact with BIF and substantial secondary Fe-rich chlorite alteration. Sericite/chlorite schist occurring around breccia zone is a weakly foliated, silicified, blocky sericite dominant schist. Sample locations marked by black dots with those used for isocon analysis labeled in blue.

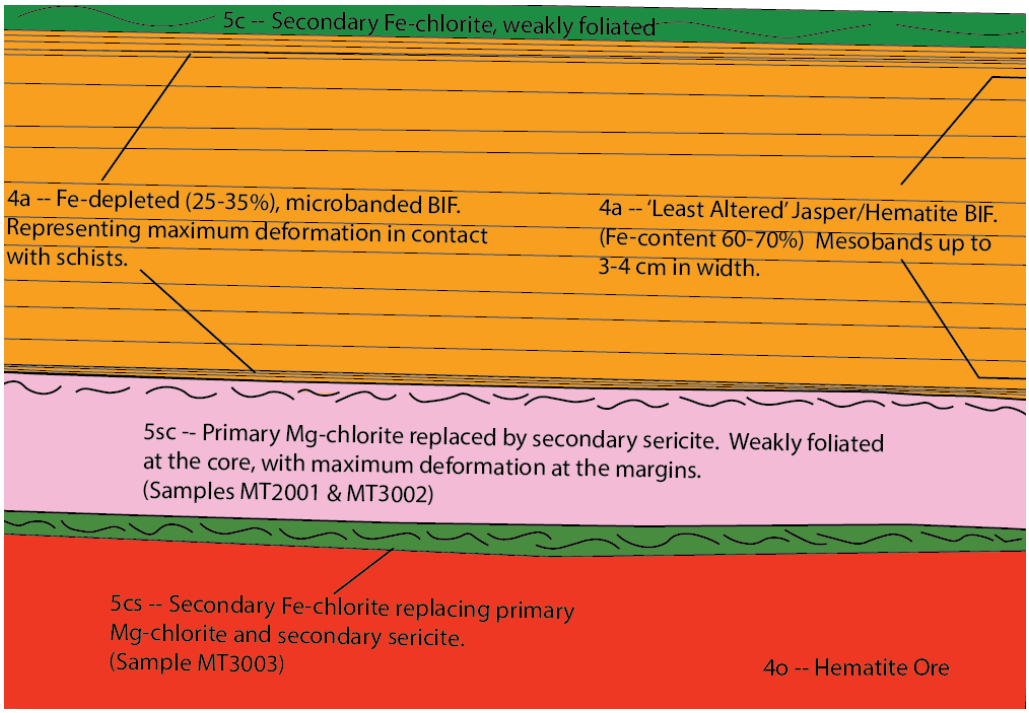

Figure 7. General cross-section through the eastern Montana cutback. East of the ore breccia zone along the main drift.

Eastern Montana Cutback

At the eastern Montana Cutback (Figure 6), relatively unaltered Soudan Member BIF trending east-west consists of mesobands (1-4 cm width) of oxidized jasper chert, less-altered chert, and hematite, and is bounded by narrow chlorite/sericite schists up to 10 ft (3.04 meters) in width (Figure 7). The shear zone to the south of the BIF outcrop is dominated by sericite alteration with maximum deformation occurring within 6-12 inches of the contact to BIF. From petrographic analysis, the narrow highly deformed sericitic schist in contact with hematite ore shows substantial primary chlorite occurring as disseminated flakes with strong dark brown/green birefringence colors (~50%) grading into dominantly sericite alteration (~60-70%) and less chlorite (<20%) away from this contact. Late veins of secondary chlorite cut foliation where in contact with the ore. Petrographic studies indicate that his chlorite is fine-grained, with weak pleochroism from light yellow to green and weak blue birefringence (Figure 8). The schist to the north of the BIF outcrop is dominated by chlorite that occurs as fine-grained aggregates replacing sericite. It is weakly foliated relative to the moderate to strongly foliated sericite-dominant schist to the south. Deformation of the Jasper-BIF is constrained to the nearest 6-12 inches in contact with shear zones. The BIF in these highly deformed zones consist of microbands depleted in

iron. At the western extent of the eastern Montana cutback there is a disconformity indicated by a transition from unaltered BIF to microbanded massive hematite ore offset by a narrow chlorite/sericite shear zone (Figure 6).

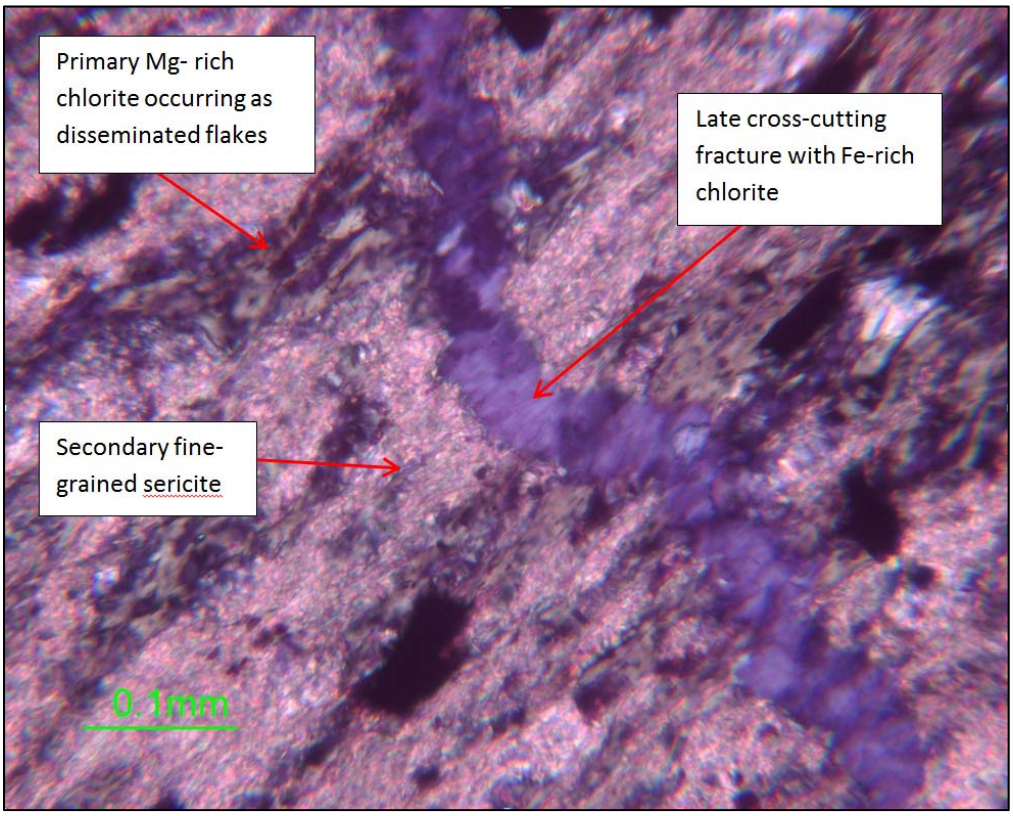

Figure 8. Sample MT-3003. Crossed-polar, transmitted light photomicrograph of chlorite/sericite schist in Montana Cutback at the eastern extent of the Montana Ore Zone showing primary Mg-rich chlorite, and secondary sericite and Fe-rich chlorite.

Western Stope Area

The stope area at the western extent of the Montana ore zone consists of massive specular hematite ore cut by secondary chlorite dominated schists (Figure 9). The chlorite shear zones appear to pinch out at the western extent of the ore body, while opening up to the east where they are separated by a large breccia zone. Locally, minor chlorite shears, up to 2 inches width, occur along bedding of the banded iron formation in contact with the ore body (Figure 9). Some chlorite schist in contact with hematite ore contains disseminated martite grains up to 0.1 mm. The breccia zone along the eastern extent of the stope area contains significant sulfides and micaceous chlorite. Additionally, a fine, crystalline, black to brownish black mineral, which may be a manganese oxide, can be observed lining vug walls within hematite ore.

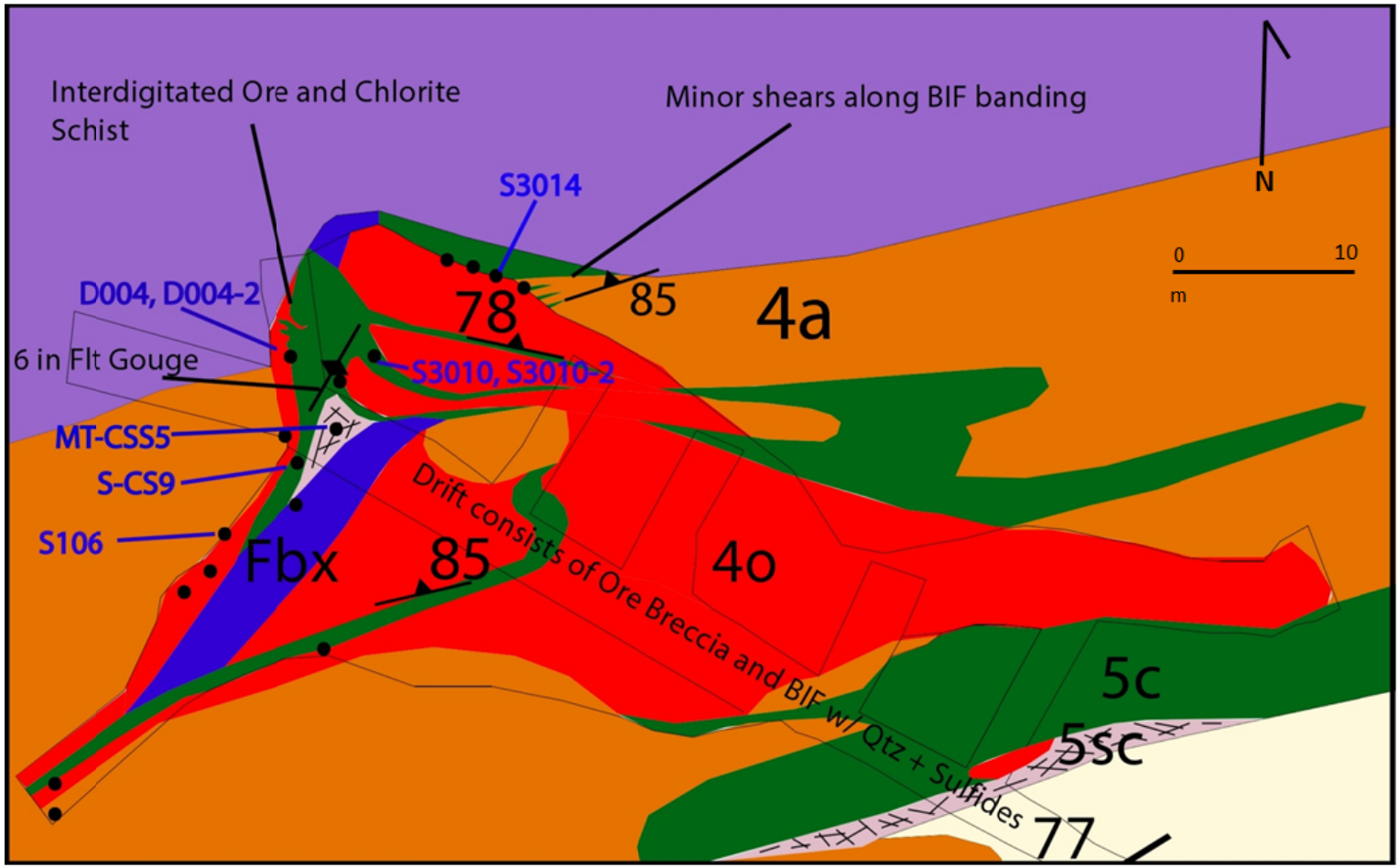

Figure 9. Western extent of Montana Ore Zone. Mapping indicates field observations within main stope area. Underlying drift shows same pattern of alteration as that to ore occurrence to the east as ore breccia and BIF with silicified sericite schist present along breccia boundaries. Sample locations marked by black dots with those used for isocon analysis labeled in blue.

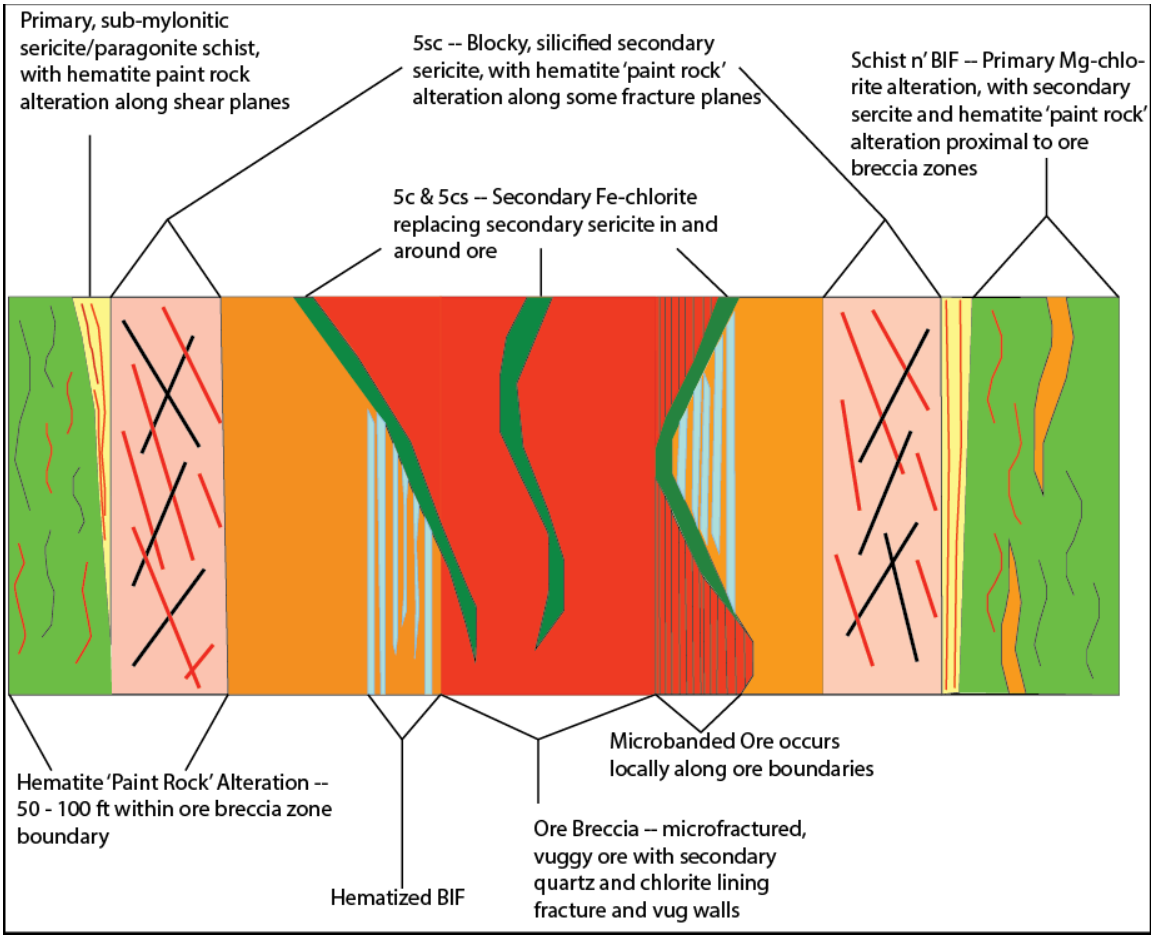

Figure 10. Generalized cross-section of drifts below ore occurrences at the eastern and western extents of the Montana Ore Zone.

Hematite "paint rock" alteration occurs at the breccia zone boundaries, along fractures within the silicified schist, and along shears in the Mg-chlorite/sericite schists intermediate to the ore (Figure 10). Hematite alteration appears to replace primary chlorite and sericite schists, as well as secondary sericite alteration. This microcrystalline hematite alteration is concentrated locally along ore breccia margins and dissipates rather abruptly moving laterally away from the massive hematite (Figure 10).

Separating the siliceous zone from the massive hematite is a narrow zone of alteration consisting of secondary chlorite schist replacing secondary sericite schist (Figure 11). These dark-green Fe-enriched schists both envelop and occur as xenoliths(?) internal to the massive hematite ore bodies.

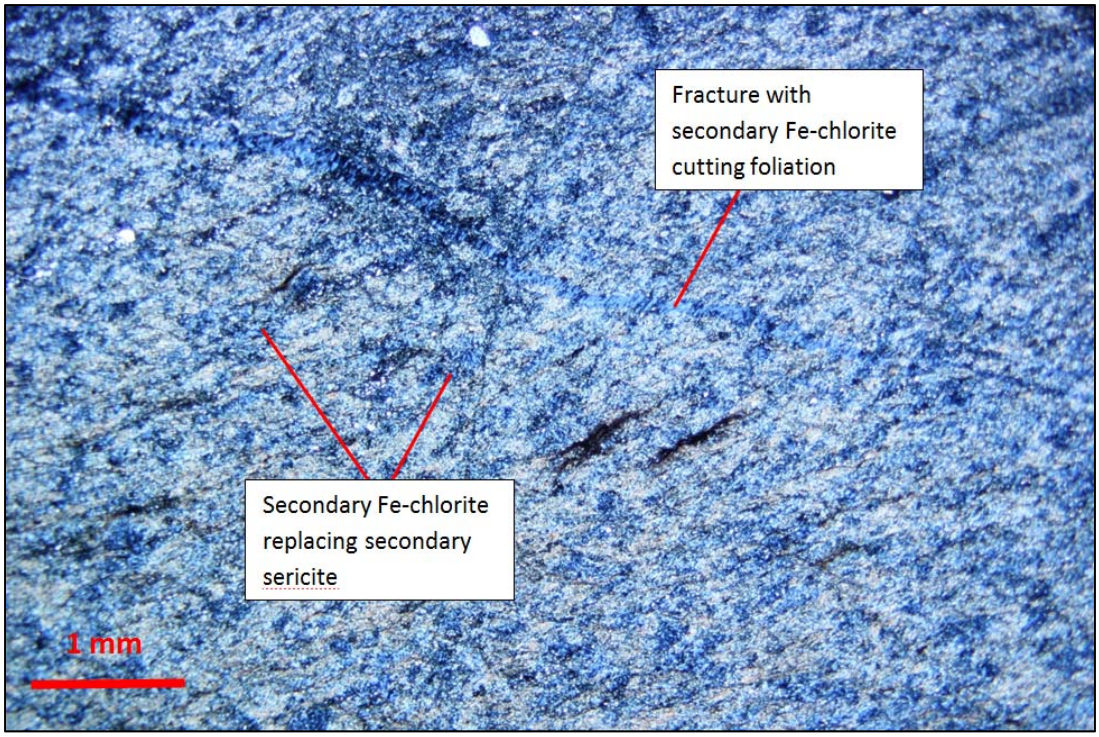

Figure 11. Cross-polar photomicrograph of sample S3010-2, chlorite replacing sericite with late cross-cutting chlorite-filled fracture cutting foliation.

Structure

Moderately foliated, chlorite- and sericite-dominated schists trend east to west and are truncated by ore breccia zones exhibiting brittle deformation. Altered meta-volcanics present at the margins of the breccia zones are composed of a pink colored, moderately foliated sericite with local silicification (blocky and fractured texture) occurring directly adjacent to laminated ore. Well-developed foliation occurs within these schists near the contact to oxide facies BIF. En echelon fractures with quartz infilling also occur within BIF in contact with these sericite altered schists. Creamy yellow, highly sheared sericite/paragonite/silica schists are present along the margins of the pink sericitic schists. These sericite/paragonite/silica schists exhibit sub-mylonitic textures (Figure 12) and appear to be a product of sericite replacing paragonite, with relatively equal parts Na and K.

No major structural contacts were observed between Fe-chlorite schists and hematite ore. The Fe-chlorite schists occur as inclusions within, and envelope, the hematite ore, and are locally interdigitated with the ore. Fe-chlorite also occurs as minor shears (< 2 inches (0.05 meters) width) along BIF bedding, at the margins of ore lenses.

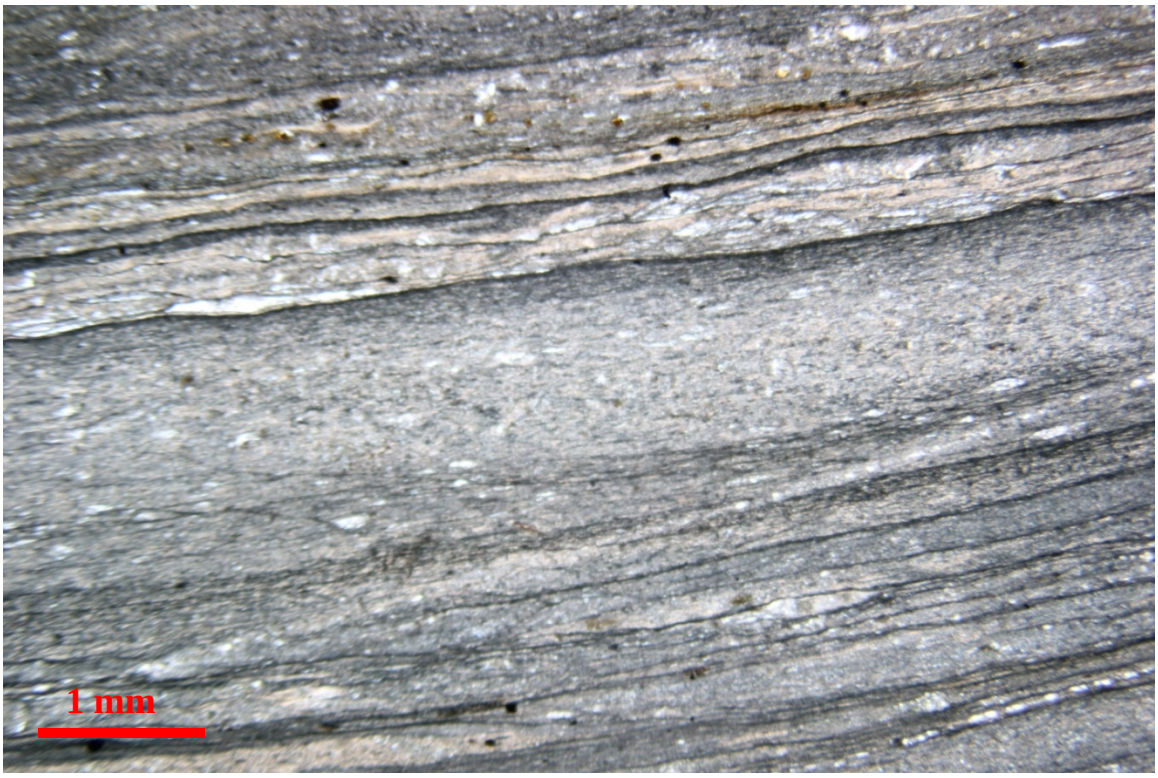

Figure 12. Cross-polar photomicrograph image of sample D003 (sericite/paragonite/silica schist) showing spaced cleavage domains (30-40 vol%).

Ore Textures

Klinger (1960) described two types of banding within the microbanded hematite ore: 1) *pseudo morph bands* with martite occurring after magnetite; and 2) *replacement* bands in which silicates and carbonates within chert have been leached and, in the case of siderite, oxidized to form bands of microcrystalline and coarser irregular hematite.

Ore breccia occurs as coarse irregular massive hematite within a fine-grained hematite matrix, with the hematite fragments ranging in size from < 1 mm to roughly 1 cm and consisting of porous, coarse platy hematite intergrown with subhedral martite (Figure 13A). Replacement bands may exhibit signs of compressive failure as bands pinching out between two pseudo morph bands (Figure 13B) or as slump structures (Figure 13C). Microbanded BIF occurs locally along ore margins and may contain microfractures with microplaty hematite (MpHem) lining fracture walls (Figure 13D). Along the ore margins, hematization of chert banding occurs, with hematite replacing silicate minerals within cherty bands (13E).

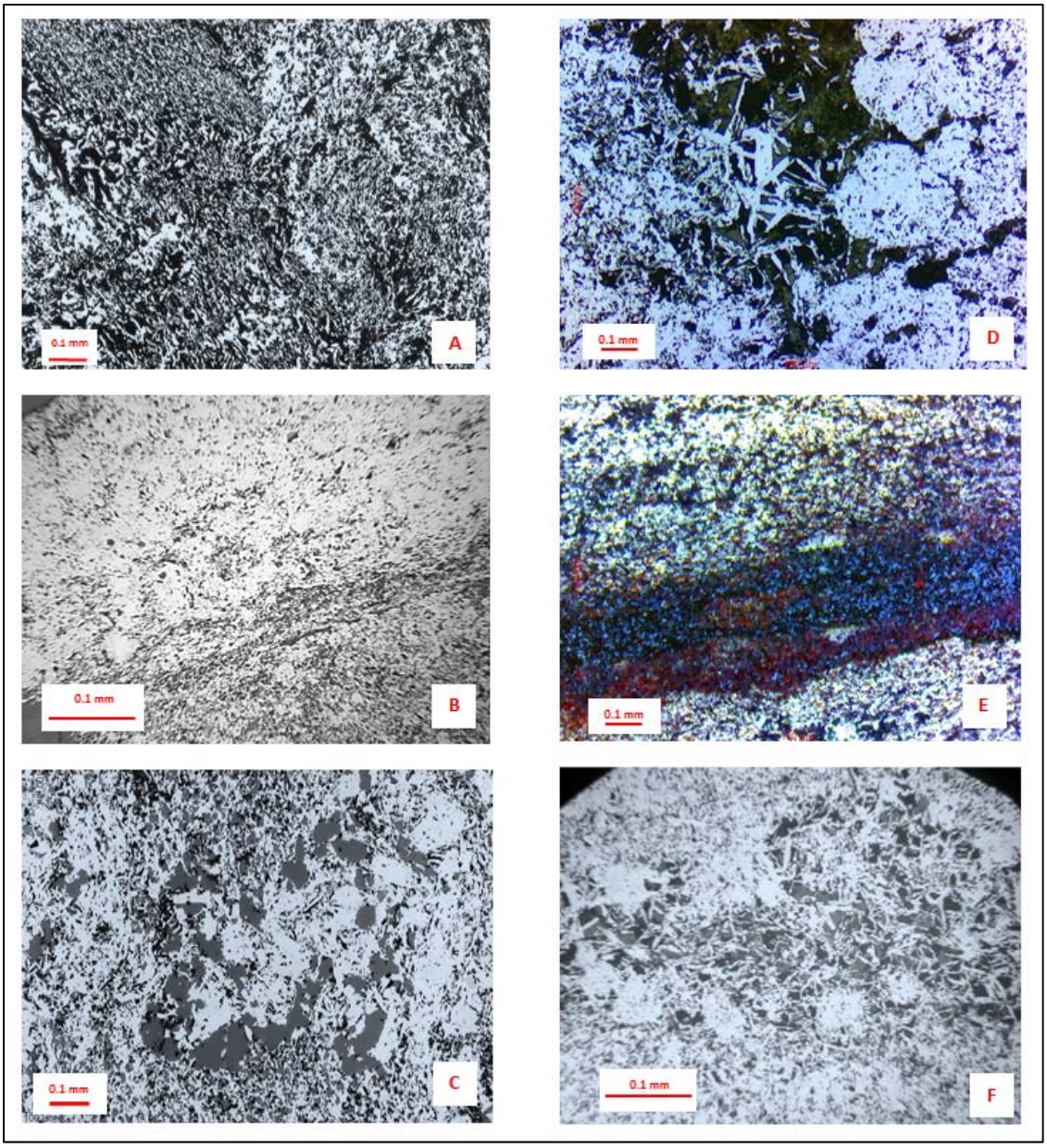

Figure 13. Photomicrograph reflected light images showing ore textures. A) Sample D2001, ore breccia with irregular hematite in fine-grained hematite matrix. B) Sample D2014, microbanded ore with replacement bands of fine-grained irregular hematite showing evidence of shearing along banding, with thinning occurring along pseudomorph band boundary. C) Sample D2009 showing slump structure of hematite within microbands. D) Sample D2016, ore breccia with microbanded hematite ore cut by fracture lined with Microplaty Hematite (MpHem). E) Sample MT-LBIF8, microbanded BIF showing hemitization of chert banding. F) Sample D2016, ore breccia with pseudomorph martite (Mt) and replacement hematite as finer, irregular grains with later MpHem lining vug walls within fine-grained hematite.

Chlorite Composition by Scanning Electron Microscopy (SEM)

The scanning electron microscope (SEM) at the University of Minnesota Duluth Research Instrumentation Lab was utilized in order to differentiate the compositions of the primary and secondary chlorites. Preparation included carbon coating (15 nm) polished thin sections. The system consisted of a JEOL JSM-6590LV SEM, combined with an INCA X-ACT energy dispersive spectroscopy system (EDS) and complimentary software. Operating conditions were optimized independently for imaging in backscattered and EDS mode, with an accelerating voltage of 15 keV producing optimal results. EDS calibration was performed on metallic Cu and is considered semi-quantitative. Sample MT3003 taken from the eastern extent of the Montana cutback, was selected as it shows primary chlorite and secondary sericite with late micro-fractures, cutting foliation, and filled by secondary chlorite. Sample S102, taken from a schist in contact with hematite ore in the stope area, was selected to represent secondary chlorite replacing secondary sericite proximal to ore.

The results of the analyses indicate primary chlorite alteration to be Mg-rich, with Fe-rich chlorite associated with late-stage alteration proximal to ore. The stoichiometric compositions for the chlorites were calculated based on 28 oxygens from Hey (1954) and are shown below (Figure 14), along with the composition of a chorite taken from a vug in the hematite ore by Kingler (1960). As indicated by the plot, Fe content of the chlorite schists appears to increase proximal to the massive hematite ore.

The analysis of sample MT3003 indicates an elevated Fe content for the secondary chlorite vein cross-cutting primary Mg-rich chlorite and secondary sericite (Figure 15). The sample S102 of Fe-chlorite schist in contact with hematite ore shows two ‘generations’ of iron mobility; coarse subhedral to euhedral martite and later MpHem. This sample also shows monazite occurring with MpHem intruding the chlorite schist (Figure 16).

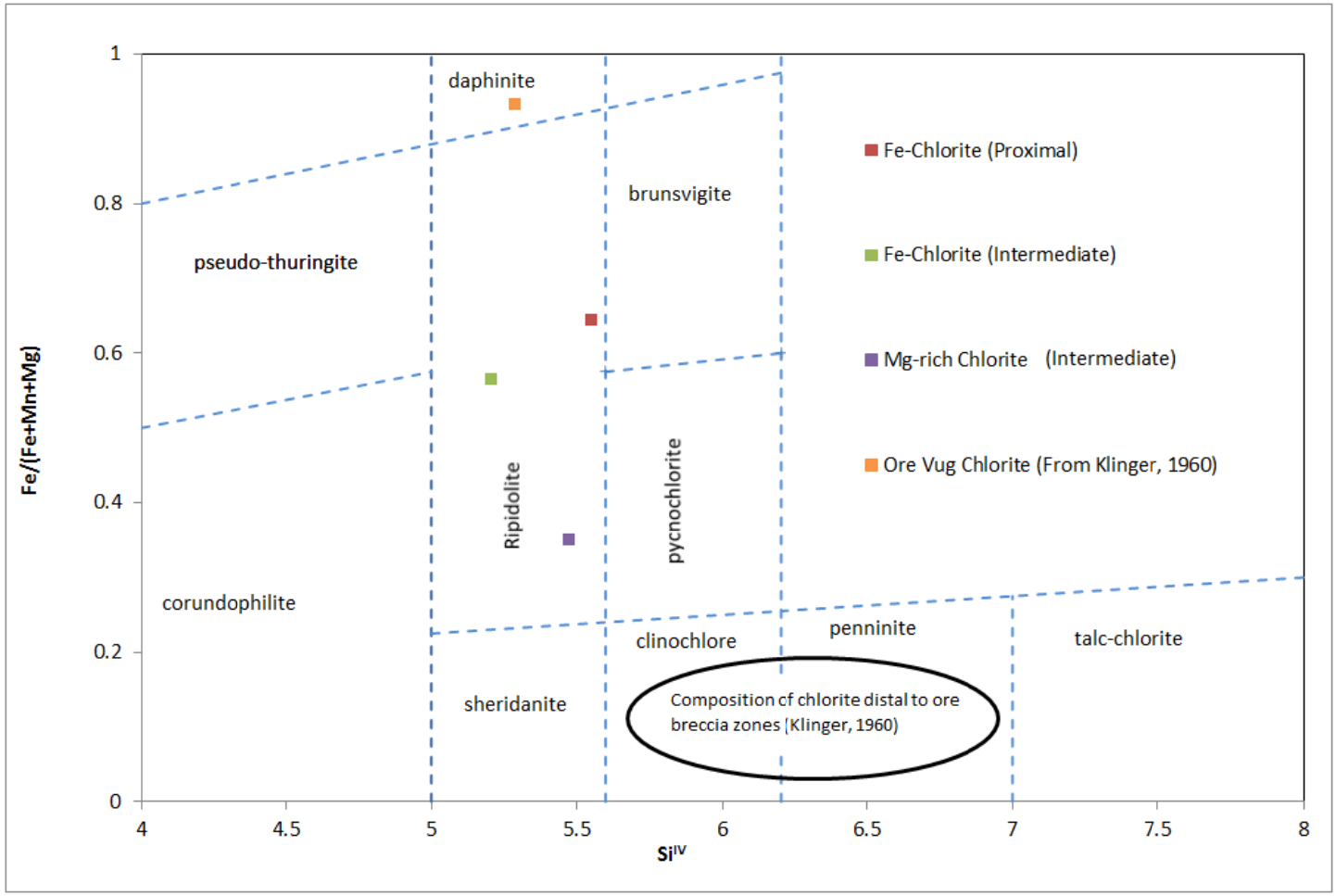

Figure 14. Chlorite compositional field according to Hey, 1954. Samples distal to hematite breccia zones were characterized through petrographic analysis by Klinger to fall within the clinochlore and penninite compositional fields.

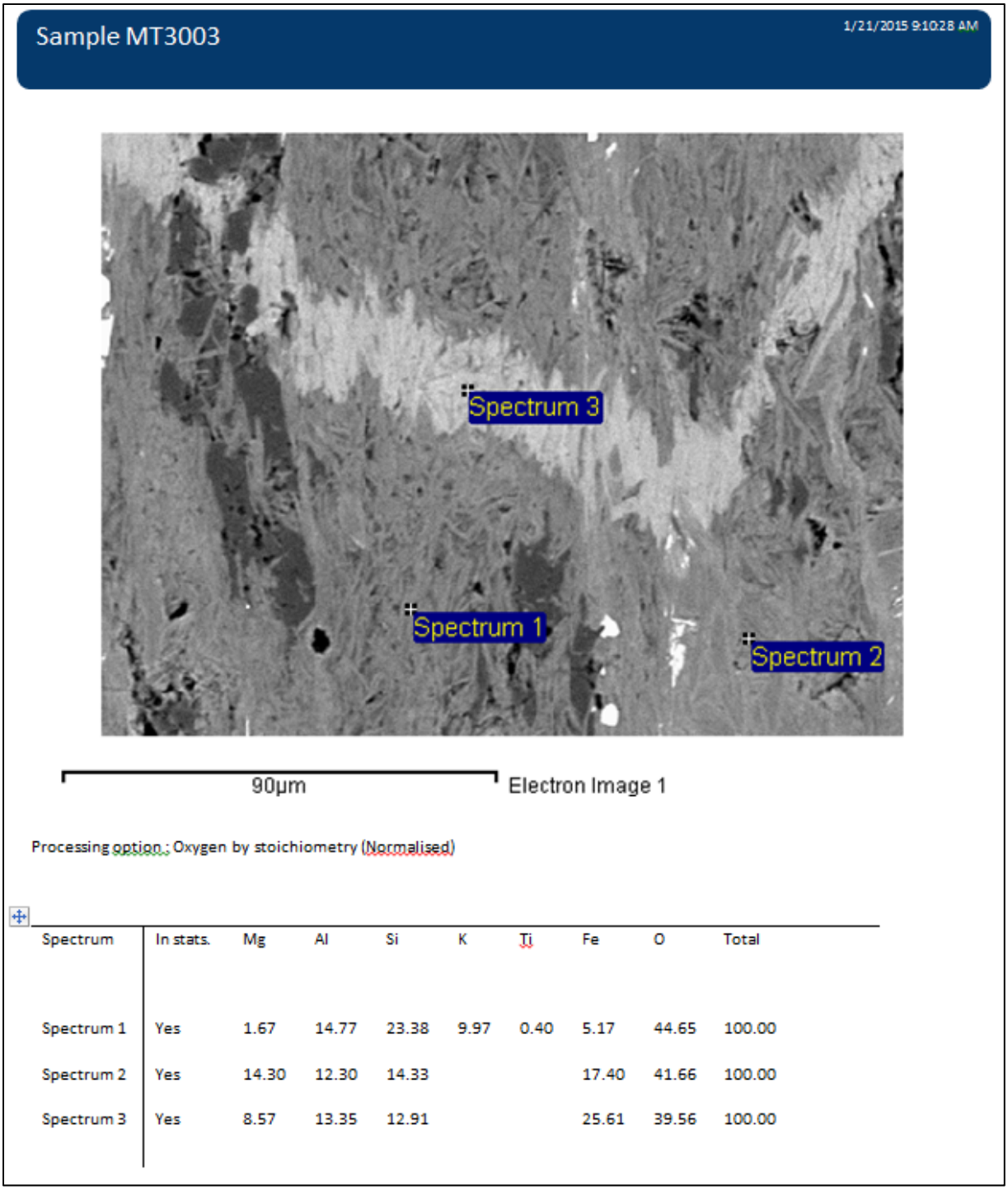

Processing option : Oxygen by stoichiometry (Normalised)

Spectrum	In stats.	Mg	Al	Si	K	Ti	Fe	O	Total
Spectrum 1	Yes	1.67	14.77	23.38	9.97	0.40	5.17	44.65	100.00
Spectrum 2	Yes	14.30	12.30	14.33			17.40	41.66	100.00
Spectrum 3	Yes	8.57	13.35	12.91			25.61	39.56	100.00

Figure 15. SEM Image of sample MT-3003. Spectrum 1: sericite replacing Mg-rich chlorite (ripidolite). Spectrum 2: Mg-rich chlorite (ripidolite). Spectrum 3: Fe-rich chlorite (ripidolite). Results in weight percent.

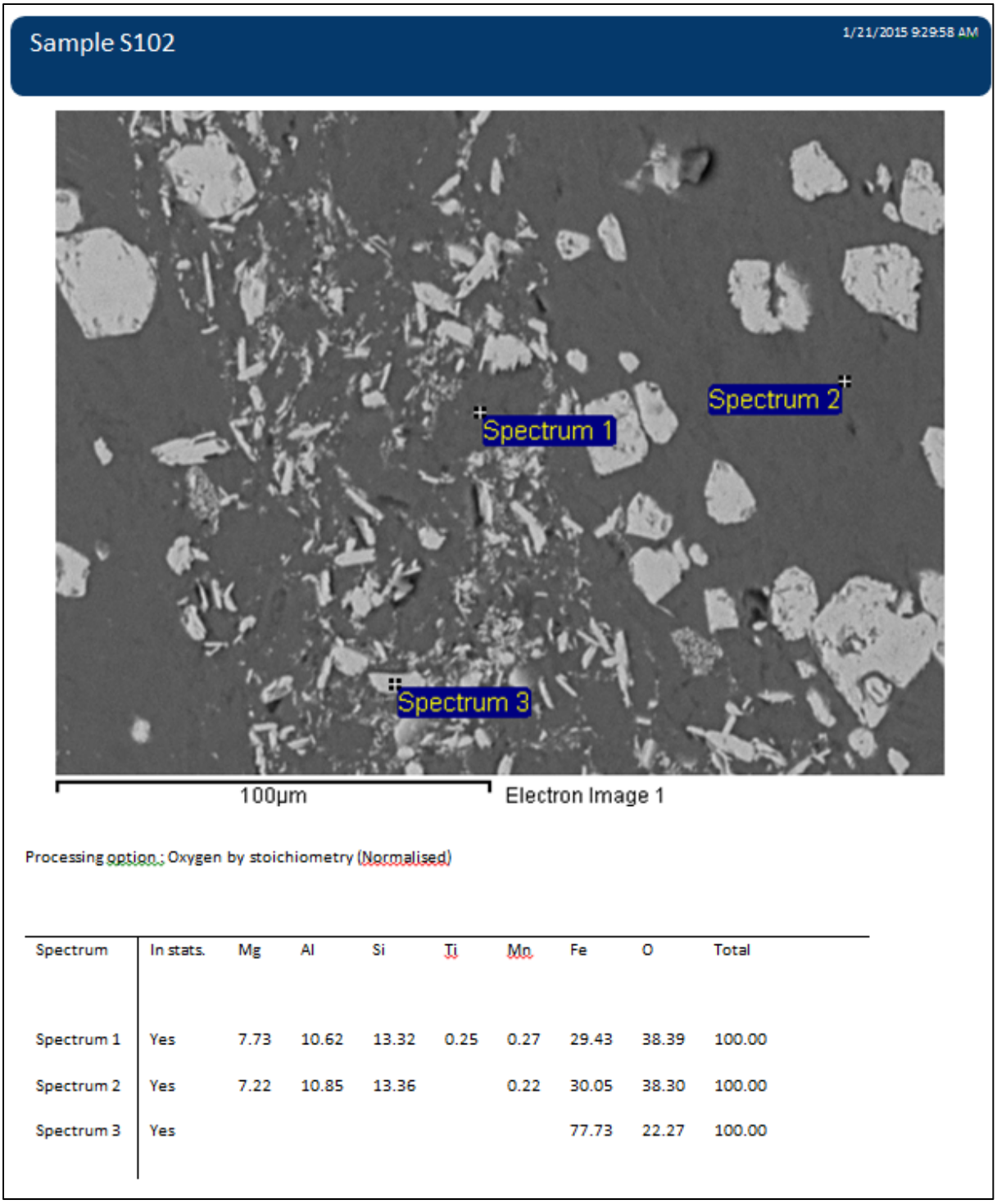

Processing option : Oxygen by stoichiometry (Normalised)

Spectrum	In stats.	Mg	Al	Si	Ti	Mn	Fe	O	Total
Spectrum 1	Yes	7.73	10.62	13.32	0.25	0.27	29.43	38.39	100.00
Spectrum 2	Yes	7.22	10.85	13.36		0.22	30.05	38.30	100.00
Spectrum 3	Yes						77.73	22.27	100.00

Figure 16. SEM Image of sample S102. Spectrum 1 and 2: Secondary Fe-rich chlorite (ripidolite) has completely replaced sericite. Spectrum 3: Tabular subhedral microplaty hematitie (MpHem) occurring after coarser martite (Mt). Results in wt percent.

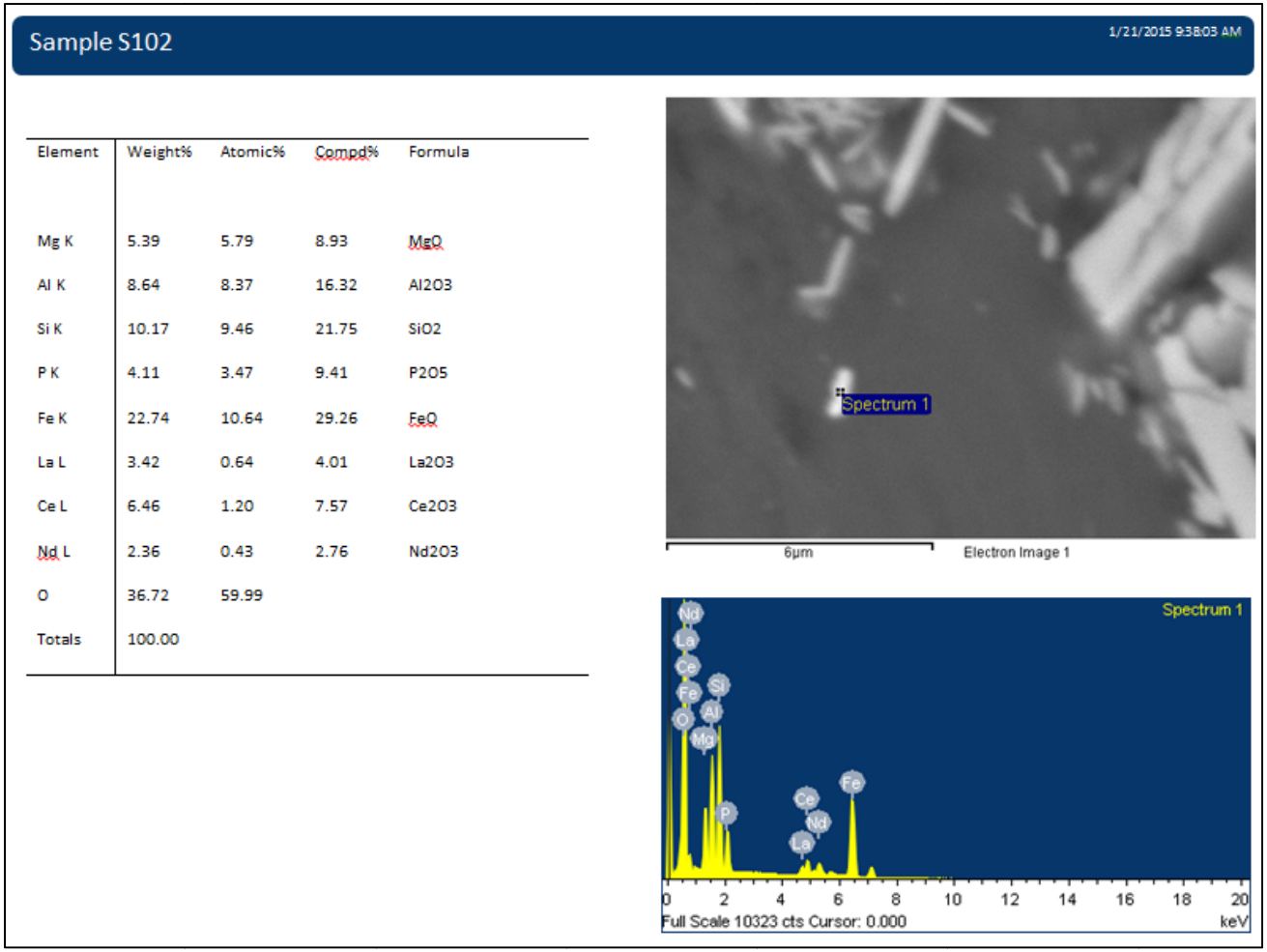

Figure 17. SEM Image of sample S102 showing monazite occurring with microplaty hematite (MpHem). Major elements detected by K-alpha emission and lanthinides by L-alpha emission. Ce-monazite stoichiometric composition: $(Ce_{0.53}\ La_{0.28}\ Nd_{0.19})\ PO_4$.

Isocon analysis

Geologic mapping indicates that massive hematite ore is spacially associated with sericite- and chlorite schists. Based on this observation it is apparent that upgrading of BIF to hematite ore is associated with K, Fe, Mg, and Si metasomatism. To evaluate chemical, mineralogical, and spatial trends, potassium (as K_2O) and magnesium (as MgO) were plotted versus iron (as Fe_2O_3) content normalized to silica on a log-log scale (Figure 18 and Figure 19). This was done in order to determine patterns of the defined alteration assemblages associated with the Montana Ore Zone. The plot of K_2O/SiO_2 versus Fe_2O_3/SiO_2 shows distinct trends for both the iron-formation and meta-volcanic samples. The plot of MgO/SiO_2 versus Fe_2O_3/SiO_2 shows two distinct trends within both the iron-formation and meta-volcanic samples. These trends represent: 1) the upgrading of jasper/hematite BIF to ore breccia associated with potassic alteration overprinting primary chlorite and sericite/paragonite alteration (IF1, V1SC and V1SS respectively); and 2) ore breccia with chlorite associated with secondary chlorite alteration overprinting secondary potassic alteration proximal to ore (IF2 and V2C).

These trends were used to define the suite of samples best representing each stage of the paragenetic sequence associated with the upgrading of BIF to hematite ore. Samples D001 and D003 define the trend (V1SS) for primary to secondary sericite alteration, while sample MT-CS1 defines the trend for primary chlorite to secondary sericite alteration (V1SC). Samples MT-2001, MT-3002, MT-3003, S-SCS3, MT-CSS5, and MT-CS2 were used to represent secondary sericite alteration for these two trends. Secondary chlorite alteration overprinting secondary sericite alteration (V2C) is represented by samples S-CS9, D004-2, and S3010-2.

The upgrading of jasper/hematite BIF to hematite ore, associated with potassic alteration (IF1) is represented by BIF samples S106 and D2019 altering to ore breccia samples D2001 and D2014 (Figure 18 and Figure 19). Ore breccia + secondary chlorite alteration is represented by the transition to samples D004, S3010, and S3014 (Figure 19).

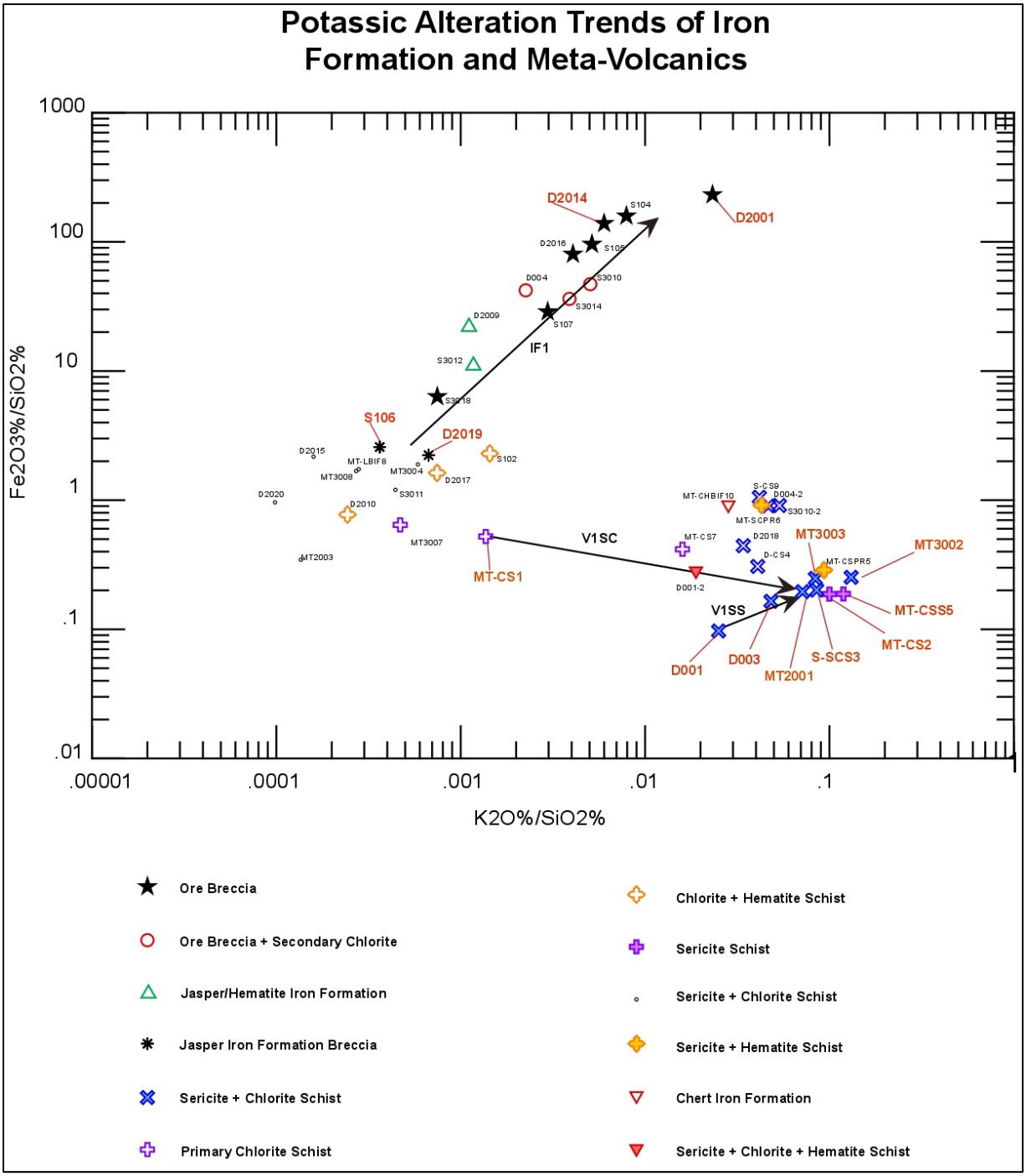

Figure 18. K/Si versus Fe/Si plot showing alteration trend of Iron-Formation (IF) and meta-volcanics during potassic alteration associated with upgrading of IF to Ore Breccia. Secondary sericite overprinting primary chlorite (V1SC) and sericite/paragonite/silica schist (V1SS). Jasper/Hematite BIF upgrading to Ore Breccia (IF1). Samples used for isocon analysis shown in red.

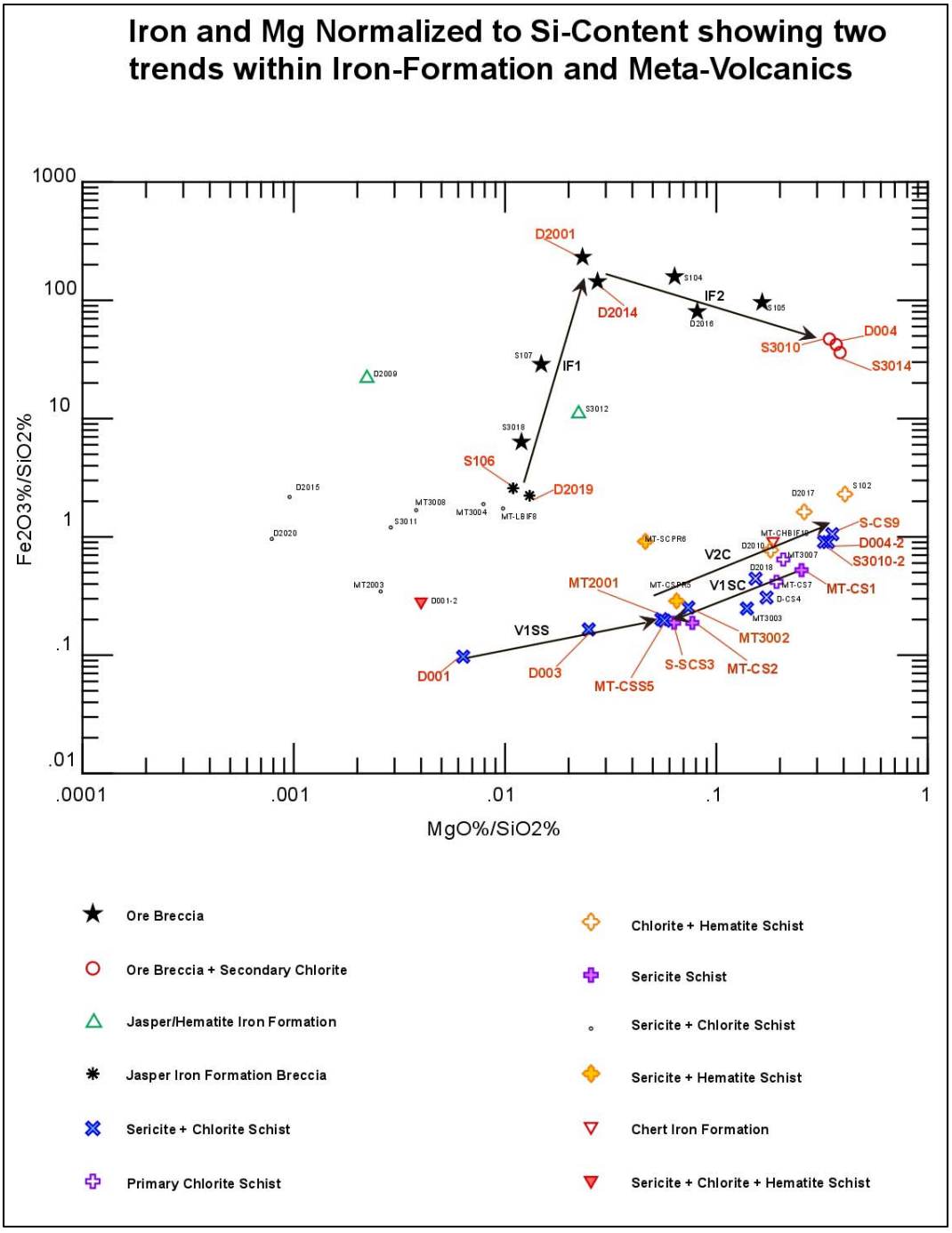

Figure 19. Mg/Si versus Fe/Si plot showing alteration trends in the Montana Ore Zone. Meta-volcanics consists of secondary Sericite overprinting primary Sericite/Paragonite/Silica Schist (V1SS), primary Chlorite Schist (V1SC) and secondary Chlorite overprinting secondary Sericite (V2C). Iron-formation consists of jasper/hematite BIF upgrading to Ore Breccia (IF1) and Ore Breccia altering to Ore + Secondary Chlorite (IF2). Samples used for isocon analysis shown in red.

The isocon method (Grant, 1986) provides a way to quantitatively estimate elemental gains and losses associated with hydrothermal alteration. From Grant (1986), the relation of compositional-mass changes can be written as:

$$C_i^A = M^O/M^A(C_i^O + \Delta C_i)$$

where C_i is the concentration of species 'i', while 'O' refers to the original rock and 'A' to the altered rock. M^O and M^A are equivalent masses before and after alteration. For each stage of alteration there exists immobile elements for which $\Delta C_i = 0$, and thus $C_i^A = (M^O/M^A)C_i^O$ defines the isocon through the origin. M^O/M^A would then be the slope of the line and represents the overall mass loss or gain associated with the alteration of the original rock 'O' to the altered rock 'A'. Once the isocon is defined, elemental gains and losses for each stage of alteration may be calculated as:

$$\Delta C_i/ C_i^O = M^A/ M^O(C_i^A/ C_i^O) - 1$$

where C_i^A/ C_i^O represents the slope of the line from the origin to data point 'i'. Graphically speaking, elements plotting above the isocon represent mass gains and those below the isocon mass losses.

If the density of a representative sample for each alteration stage is known , then the volume loss or gain can be calculated as:

$$V^A/V^O = M^A/M^O(\rho_o/\rho_A)$$

where V^O is the volume of the original rock before alteration and V^A is the volume of the rock after alteration. Original rock density is defined as ρ_o and altered rock density as ρ_A.

Rock densities of meta-volcanics and oxide facies rocks were measured for each stage of alteration used to define the isocon analyses. The results of which can be seen below in Table 1.

Table 1. Measured densities for altered basalts and oxide rocks (27th lvl of Soudan Mine).

Primary Sericite	Primary Chlorite	Secondary Sericite	Secondary Chlorite	BIF	Ore Breccia	Ore Breccia + Secondary Chlorite	Hematite Schist
2.5g/cm^3	2.5g/cm^3	2.6g/cm^3	2.8g/cm^3	3.1g/cm^3	4.6g/cm^3	4.4g/cm^3	3.0g/cm^3

Potassic Alteration

The isocons for potassic alteration of primary sericite/paragonite and chlorite are defined by immobile Al_2O_3, TiO_2, Hf, and Zr (Figure 20 and Figure 21). Al_2O_3 and TiO_2 are generally thought to be immobile oxides in hydrothermal systems. Hf and Zr are high field strength elements that are highly charged with a relatively small ionic radius, and are considered to be among the most immobile elements in aqueous solutions (Rollison, 1993).

Both analyses for secondary sericite alteration overprinting primary chlorite and primary sericite/paragonite/silica schists give an overall mass loss of 8%. The isocon for the replacement of chlorite by secondary sericite shows a minor gain in Si and significant gains in K_2O, Ba, Rb, Sr, Cu, and the LREE. Minor losses associated with the sericitization of chlorite schists include CaO, P_2O_5, and Ni, with significant losses in Fe_2O_3, Co, Zn, and MgO (Figure 20).

The isocon for potassic alteration of sericite/paragonite/silica schists shows minor gains in the LREE and significant gains in Fe_2O_3, MgO, K_2O, Rb, Ba, CaO, P_2O_5, Zn, and Ni. The only significant losses associated with the potassic alteration of the sericite/paragonite/silica schist are in Na_2O and Sr, with minor losses in SiO_2 and Cu (Figure 21).

Associated with potassic alteration, the increase of potassium could result from the reaction of a K-rich solution with alumino-silicate minerals such as pyrophyllite and the replacement of Na_2O by K_2O in paragonite. The replacement of chlorite by sericite would also produce a gain in K_2O and precipitous loss in Fe_2O_3 and MgO. K_2O, Ba, and Rb are all categorized as large-ion lithophile elements (LILE) and typically behave similarly in hydrothermal systems. Gains in both Ba and Rb for the alteration of sericite/paragonite and chlorite to secondary sericite mirror the gain in K_2O. A gain in Fe_2O_3 for the potassic alteration of sericite/paragonite schists can be attributed to a higher chlorite content of secondary sericite schists. Secondary Fe-rich chlorite was observed in thin-section, occurring in microfractures within secondary sericite schists (Figure 8).

The isocon analyses for secondary sericite replacing primary sericite/paragonite and chlorite also shows the HREE to be relatively immobile. HREE, Y, and V were thus used to define the isocon for the upgrading of Jasper/Hematite BIF to ore breccia associated with potassic alteration of the meta-volcanic wall rocks (Figure 22). The upgrading of BIF to hematite ore is associated with an overall mass loss of 9% with a gain in Fe_2O_3 and significant losses in SiO_2, Al_2O_3, MgO, CaO , P_2O_5, and LREE.

An almost complete loss in silica content (98%) and associated removal of phyllosilicate minerals, such as chlorite, within chert results in a loss in MgO and Al_2O_3 as well. Excluding Fe_2O_3, all major and trace elements show losses as they are dominant within siliceous chert bedding in BIF (Figure 22). Similar losses in CaO, P_2O_5, and LREE suggest the LREE occur as monazite in apatite. The gain in Fe_2O_3 content may be attributed to later hematite alteration observed cutting secondary sericite proximal to ore.

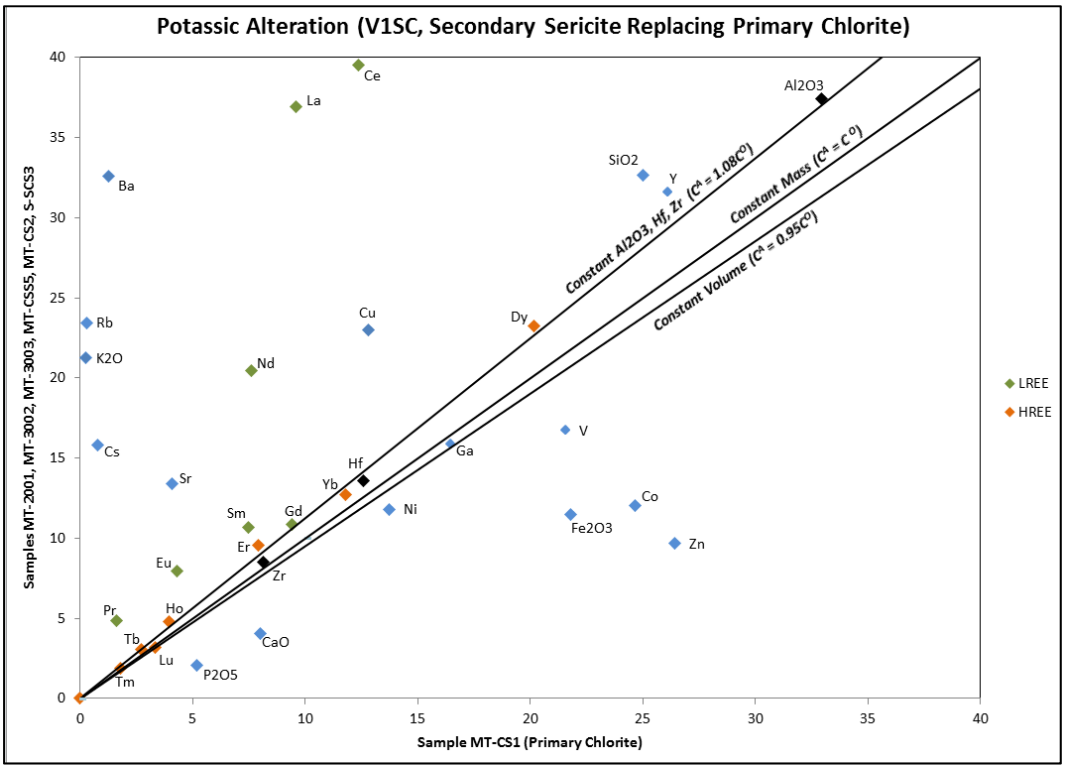

Figure 20. Isocon plot for sericite replacing Mg-chlorite alteration proximal to hematite ore.

The slope of the isocon for the upgrading of BIF to ore breccia (Figure 19) yields $M^O/M^A = 1.1$, which equates to a mass loss of 9%. Thus the volume loss can be calculated using the change in density from BIF to ore shown in Table 1 as: $V^A/V^O = 0.91(\rho_o/\rho_A)$ or 0.91*(3.08/4.62) = 0.61, equivalent to a volume loss of 39%.

The results of the isocon analyses for the sericitization of earlier Mg-rich chlorite and sericite ±paragonite +silica schists and associated upgrading of BIF to hematite ore can be seen below in tables 2 and 3, respectively.

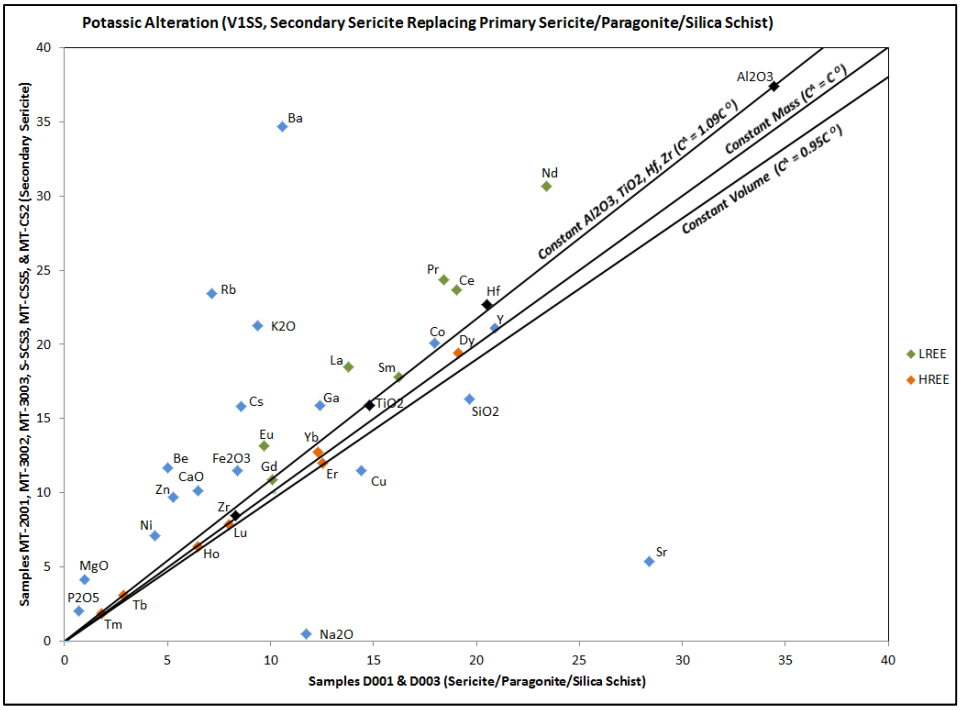

Figure 21. Isocon plot for sericite replacing primary sericite/paragonite/silica alteration intermediate to hematite ore.

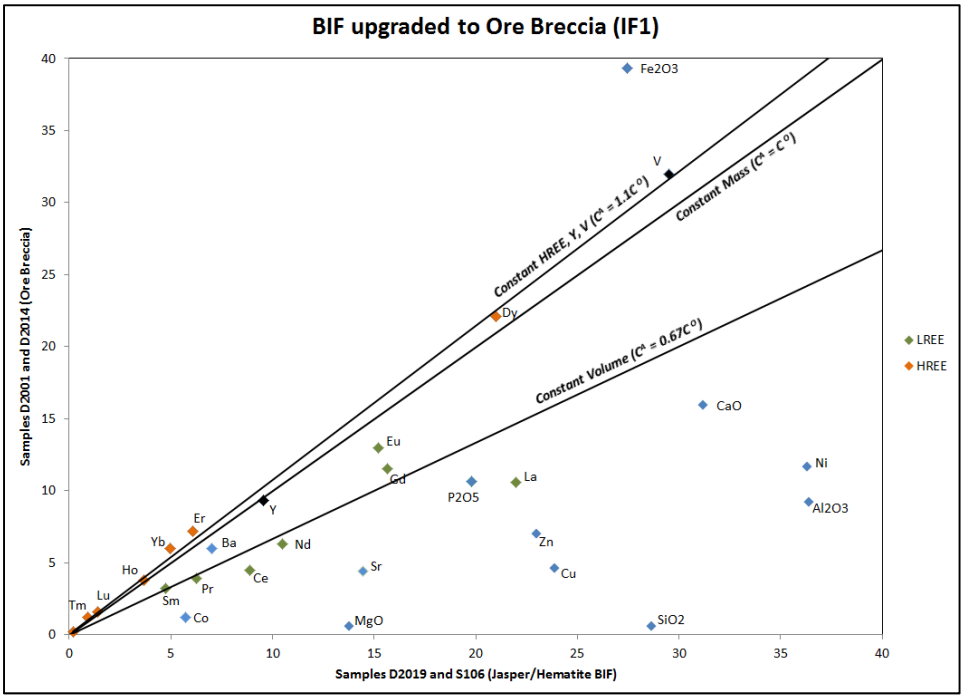

Figure 22. Isocon plot for upgrading of hematite/jasper BIF to ore breccia related to sericite alteration.

Table 2. Chemical changes associated with sericitization of earlier formed sericite/paragonite/silica (5s) and Mg-rich chlorite (5c) alteration based on constant Al_2O_3, Hf, and Zr.

Component	% Change	
	5s	5c
SiO_2	-22.6	20.1
Al_2O_3	1.4	4.59
Fe_2O_3	27.5	-51.5
MgO	298	-63.7
CaO	46	-53.2
Na_2O	-96	N/A
K_2O	112	8061
TiO_2	0.27	-34
P_2O_5	176.6	-63.4
MnO	33.3	-67.1
Ba	206.8	2250
Sr	-82.4	201
Rb	206.5	7648
Hf	3.2	-0.62
Zr	-4.87	-3.97
V	60.3	-28.6
Y	-5.8	11.65
La	24.9	254
Ce	16.3	193
Pr	23.5	173
Nd	22.3	147.6
Sm	2.4	31.4
Eu	27	68.8
Gd	0.26	6.2
Tb	-1.3	4.6
Dy	-5.5	6.2
Ho	-7.8	11.6
Er	-11	11.3
Tm	-4	-5.4
Yb	-3.4	-0.64
Lu	-8.2	-13.8
Cu	-25.5	65.4
Ni	50.7	-20.7
Zn	70.8	-66.2
Co	4.6	-55
LOI	30.5	-43
Mass	-8	-8

Table 3. Chemical changes associated with upgrading of jasper/hematite BIF to microbanded hematite ore based on constant V, Y, and HREE. Components measuring at or near detection limits omitted.

Component	% Change BIF
SiO_2	-98.2
Al2O3	-77
Fe2O3	30
MgO	-96
CaO	-54
Na2O	N/A
K2O	N/A
TiO2	N/A
P2O5	-51
MnO	N/A
Ba	-22
Sr	-72
Rb	-82
Hf	N/A
Zr	-21
V	-1.6
Y	-11.7
La	-56
Ce	-55
Pr	-43
Nd	-46
Sm	-39
Eu	-23
Gd	-33
Tb	-16
Dy	-4.5
Ho	-7.3
Er	7
Tm	21
Yb	9.9
Lu	3.7
Cu	-82.5
Ni	-71
Zn	-72
Co	-81
LOI	-51
Mass	9

Hematite 'Paint Rock' Alteration

The isocon representing hematite alteration replacing primary sericite is defined by constant Al_2O_3, TiO_2, and Zr (Figure 23). This isocon for hematite alteration gives an overall mass gain of 33% for sericite altered to hematite. Elemental mass gains include Fe_2O_3, MgO, V, Cu, Ni, Zn, LREE, and HREE. Mass losses include SiO_2 (11%), Na_2O (83%), and K_2O (21%).

The slope of the isocon for sericite altered to hematite (Figure 23) yields $M^O/M^A = 0.75$, which equates to a mass gain of 33%. Thus the change in volume can be calculated using the change in density from sericite to hematite altered schists shown in Table 1 as: $V^A/V^O = 1.33(\rho_o/\rho_A)$ or 1.33*(2.5/3) = 1.1, equivalent to a gain in volume of 10%.

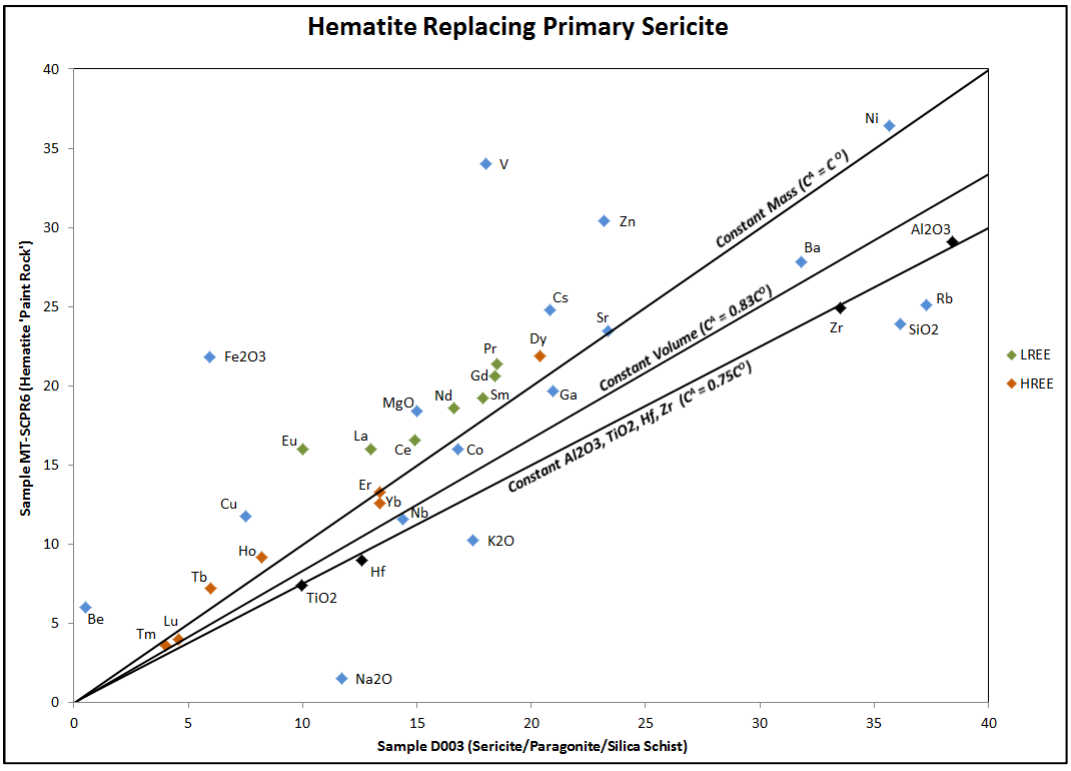

Figure 23. Isocon plot for hematite replacing sericite/paragonite/silica alteration.

With the removal of Na_2O accounting for the only significant loss, the system continued to effectively remove previous sodic minerals during this stage of alteration. A gain in MgO may represent the formation of chlorite associated with dissolved iron reacting with phyllosilicate minerals. HREE and LREE are similarly enriched, with Eu showing relative enrichment versus the other REE. Hematite appears to be replacing sericite and paragonite, reflected by similar losses in SiO_2, K_2O, and Na_2O. The gain in mass can be attributed to Fe_2O_3, with greater atomic mass, replacing silicate minerals. The results of the isocon analysis for the hemitization of sericite schists can be seen below in table 4.

Table 4. Chemical changes associated with hematite alteration based on constant aluminum, titanium, and zirconium. Components measuring at or near detection limits omitted.

Component	% Change
	Hematite Schist
SiO_2	-10.7
Al2O3	2.3
Fe2O3	396
MgO	65.7
CaO	N/A
Na2O	-82.7
K2O	-20.7
TiO2	0.87
P2O5	N/A
MnO	N/A
Ba	18
Sr	35.5
Rb	-9
Hf	-3.5
Zr	0.39
V	155
Y	60
La	66
Ce	50
Pr	56
Nd	51
Sm	45
Eu	116
Gd	51
Tb	62
Dy	45
Ho	52
Er	34
Tm	22
Yb	27
Lu	17
Cu	112
Ni	38
Zn	77
Co	29
LOI	55
Mass	33

Fe-Chlorite Alteration

For the isocon representing secondary chlorite replacing secondary sericitic (potassic) alteration, constant Al_2O_3 and TiO_2 as well as constant Hf and Zr are related to the constant mass and constant volume isocons (Figure 24). For the isocon defined by Al_2O_3 and TiO_2 an overall mass loss of 11% is given. However, the isocon defined by Hf and Zr appear to match up well with constant mass and volume. These isocons show a 0 to 5% overall mass gain for meta-volcanic rock altered to secondary chlorite. Significant gains include Fe2O3, MgO , MnO, Cu, Zn, Eu, and HREE, with losses in SiO_2, K_2O, and Ni.

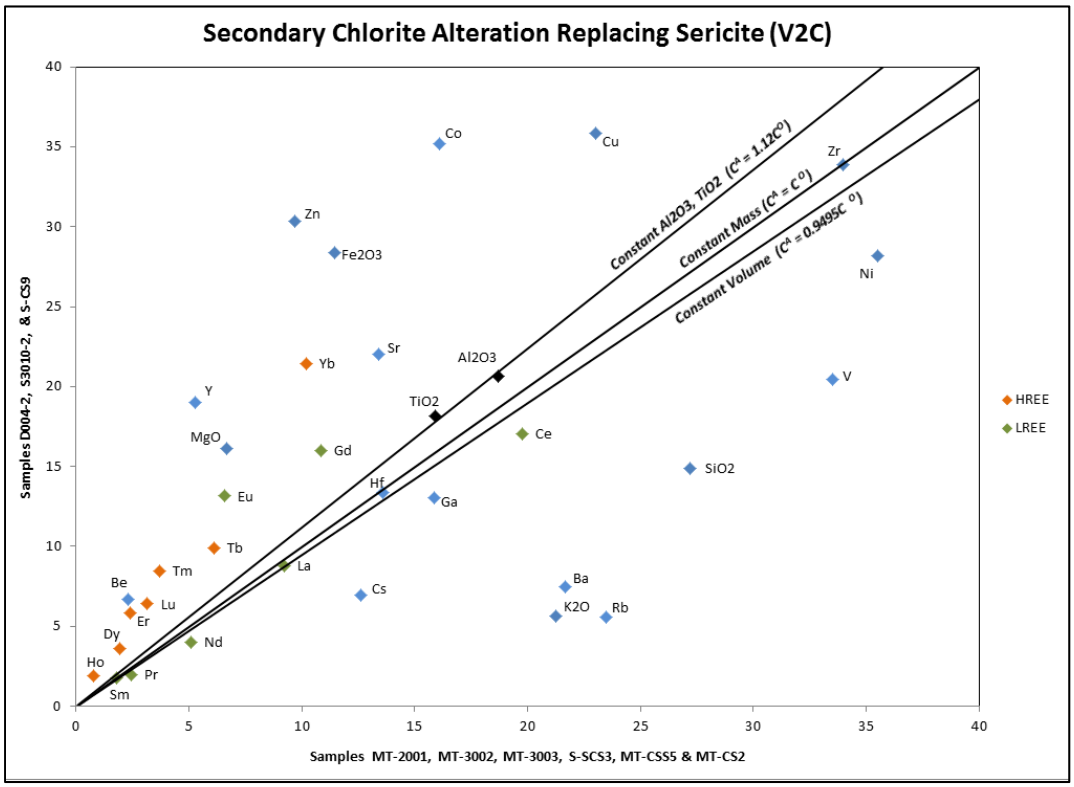

Figure 24. Isocon plot for Fe-chlorite alteration replacing secondary sericite (potassic alteration) proximal to hematite ore.

Gains in Fe_2O_3 and MgO and losses in K_2O, Ba, and Rb reflect the replacement of sericite by chlorite. In thin-section fine-grained Fe-chlorite is seen replacing sericite in schists enveloping and intruding hematite ore. The LREE appear to be immobile during this stage of alteration, with the exception of Eu, which shows enrichment similar to that of the HREE.

The isocon for the associated hematite ore breccia + secondary Fe-Chlorite is defined by constant mass and constant volume and shows an overall mass loss for the ore of 0-5% (Figure 25). Mass gains associated with the addition of chlorite to ore include SiO2 (271-289%), CaO (12-17%), P_2O_5 (8-13%), LREE (52-127%), HREE (158-333%), Zr (287-306%), Zn (400-424%), Ni (215-230%) and nearly all Al_2O_3, MgO, and TiO_2. Mass losses include Fe_2O_3 (5-10%), CaO (34%), and Cu (7-11%).

The results of the isocon analysis for Fe-chlorite alteration and associated development of ore breccia can be seen in tables 5 and 6, respectively.

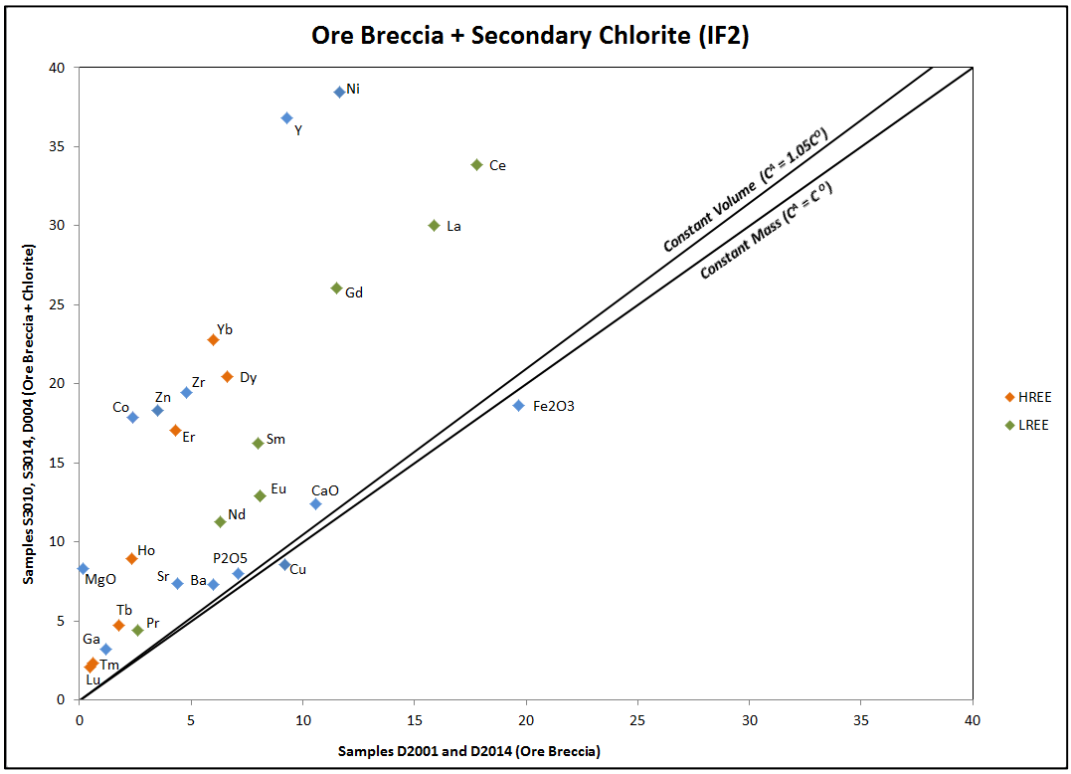

Figure 25. Isocon plot for the addition of Fe-chlorite within ore breccia adjacent to chlorite schist.

Table 5. Chemical changes associated with Fe-chlorite (5c) alteration based on constant hafnium and zirconium. Components measuring at or near detection limits omitted.

Component	% Change
	5c
SiO_2	-45
Al2O3	11
Fe2O3	149
MgO	144
CaO	N/A
Na2O	N/A
K2O	-76
TiO2	15
P2O5	N/A
MnO	283
Ba	-65
Sr	66
Rb	-76
Hf	-0.58
Zr	0.58
V	-38
Y	264
La	-4
Ce	-13
Pr	-18
Nd	-21
Sm	0
Eu	101
Gd	49
Tb	63
Dy	87
Ho	139
Er	147
Tm	131
Yb	113
Lu	105
Cu	57
Ni	-20
Zn	216
Co	121
LOI	78
Mass	nil

Table 6. Chemical changes associated with transition from microbanded hematite ore to ore breccia with Fe-chlorite based on constant mass.

Component	% Change Ore Breccia
SiO_2	289
Al2O3	635
Fe2O3	-5
MgO	5433
CaO	17
Na2O	N/A
K2O	N/A
TiO2	533
P2O5	13
MnO	256
Ba	22
Sr	67
Rb	N/A
Hf	400
Zr	306
V	55
Y	296
La	89
Ce	90
Pr	67
Nd	79
Sm	103
Eu	60
Gd	127
Tb	170
Dy	208
Ho	280
Er	294
Tm	290
Yb	280
Lu	333
Cu	-7.25
Ni	230
Zn	424
Co	644
LOI	389
Mass	nil

The results of the isocon analyses, indicating relative mass losses and gains associated with each stage of wall rock alteration during the upgrading of BIF to hematite ore, can be seen below in Table 7. Also shown are elemental losses and gains for each stage of alteration.

Table 7. Results of Isocon Analyses. Immobile elements are distinguished as those with calculated mass gains or losses 0-10%.

			Elemental Trends		
Comparison	Lithology	ΔMass	Gains	Losses	Immobile
(Potassic Alteration) Paragonite/sericite/silica to sericite alteration	Soudan Basalt	Minor loss	K, Ba, Rb, V Zn, Ni, LREE	Na, Si, Cu, Sr	Al, Ti, Hf, Zr, HREE
(Potassic Alteration) Mg-rich chlorite to sericite alteration	Soudan Basalt	Minor loss	K, Si, Ba, Rb, Cu, Sr, Cs, LREE	Fe, V, Co, Zn	Al, Hf, Zr, HREE
Martite/hematite BIF to microbanded hematite ore	BIF	Minor loss	Fe	Si, Al, Mg, Ca, P, Ni, Zn, Sr, LREE	HREE, Y, V
Paragonite/sericite/silica to hematite altered schist	Soudan Basalt	+33%	Fe, Mg, V, Cu, Zn, LREE, HREE	K, Na, Rb, Si	Al, Ti, Hf, Zr
Sericite to Fe-chlorite altered schist	Soudan Basalt	nil	Fe, Mg, Zn, Cu, Co, Sr, Eu, HREE	K, Ba, Rb, Si, V, Ni, Cs	Hf, Zr, LREE (La, Ce, Pr, Nd)
Laminated ore to ore breccia + Fe-chlorite	BIF	nil	Mg, Si, Zn, Co, Ni, HREE, LREE	None	Fe?

REE Geochemistry

REE concentrations were normalized to C1 chondrite values obtained from Anders and Grevfor (1989) for each stage of wall rock alteration associated with the upgrading of BIF to hematite ore (Figure 26Figure 27, Figure 28Figure 29). Samples taken outside ore breccia zones along the 27th level consist of primary sericite/paragonite/silica schist and chlorite schist intermediate to hematite ore occurrences. The normalized REE plot of primary chlorite-sericite altered schists (Figure 26) shows elevated LREE concentrations relative to HREE and a slight negative Eu anomaly. Secondary sericite (potassic alteration) is associated with LREE enrichment (20 to > 200 wt%) as well as a positive Eu anomaly for a few samples taken within these schists (Figure 27). Hematite altered schists occurring within both primary sericite/paragonite and Mg-rich chlorite at breccia zone boundaries and secondary sericite alteration along fractures and shear planes adjacent to ore show similar enrichment of both LREE and HREE and a minor positive Eu anomaly for all samples (Figure 28). Secondary Fe-rich chlorite surrounding the hematite ore shows elevated HREE concentrations relative to the LREE and a stronger positive Eu anomaly (Figure 29).

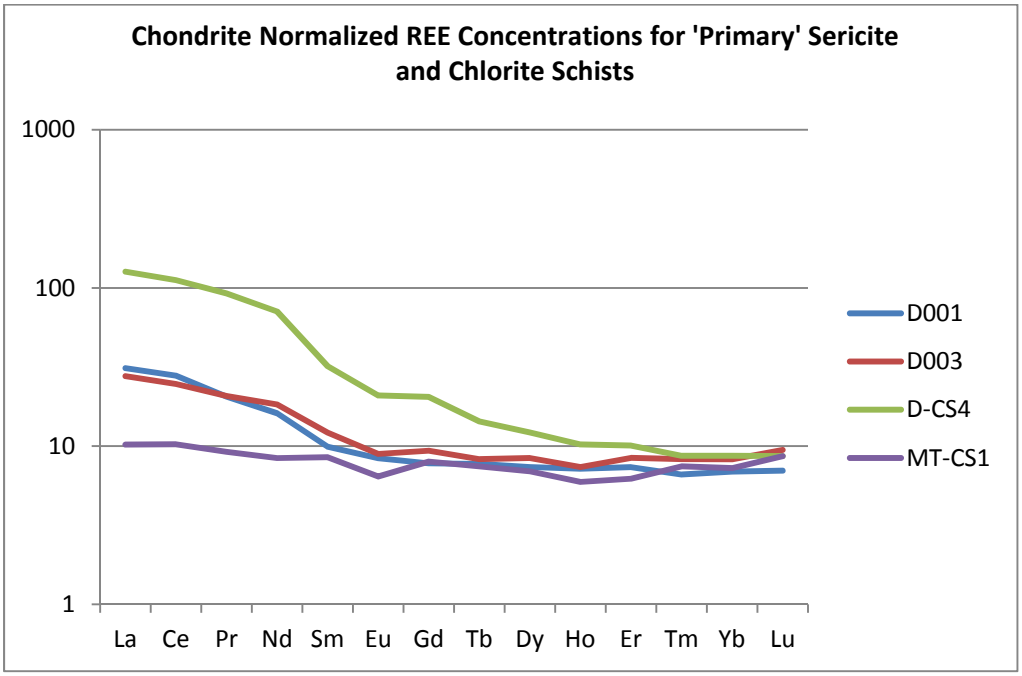

Figure 26. C1 chondrite normalized REE concentrations of altered basalts outside hematite ore breccia zones, intermediate to ore. These samples represent primary sericite/chlorite alteration occurring prior to

upgrading of Jasper-BIF to hematite ore. Samples D001 D001 and D003 consist of sericite/paragonite altered rocks and samples D-CS4 and MT-CS1 consist of Mg-chlorite altered rocks.

HREE are less compatible than the LREE due to their smaller ionic radii, and can become fractionated during hydrothermal metasomatism. Bau (1991) concluded that because of the difference in ionic radii of the REE, a fluid-rock interaction controlled by sorption mechanisms would produce a fluid displaying $La_n/Lu_n > 1$. Wood (1990) showed that at elevated temperatures REE-fluoride complexes dominate in a hydrothermal system. Bau (1991) points out that because the of increase of stability constants from La to Lu for REE-flouride complexes, transport of the REE as fluoride complexes would result in the REE pattern of the fluid displaying $La_n/Lu_n < 1$.

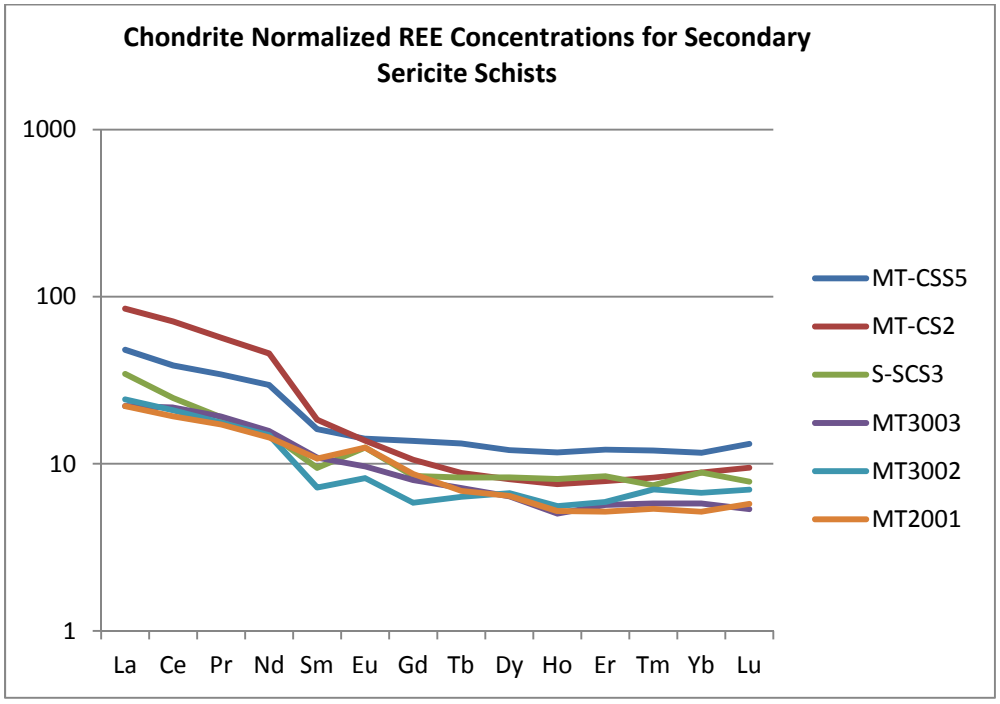

Figure 27. C1 chondrite normalized REE concentrations of secondary sericite schists (Potassic alteration) occurring at the outer edges of ore breccia zones.

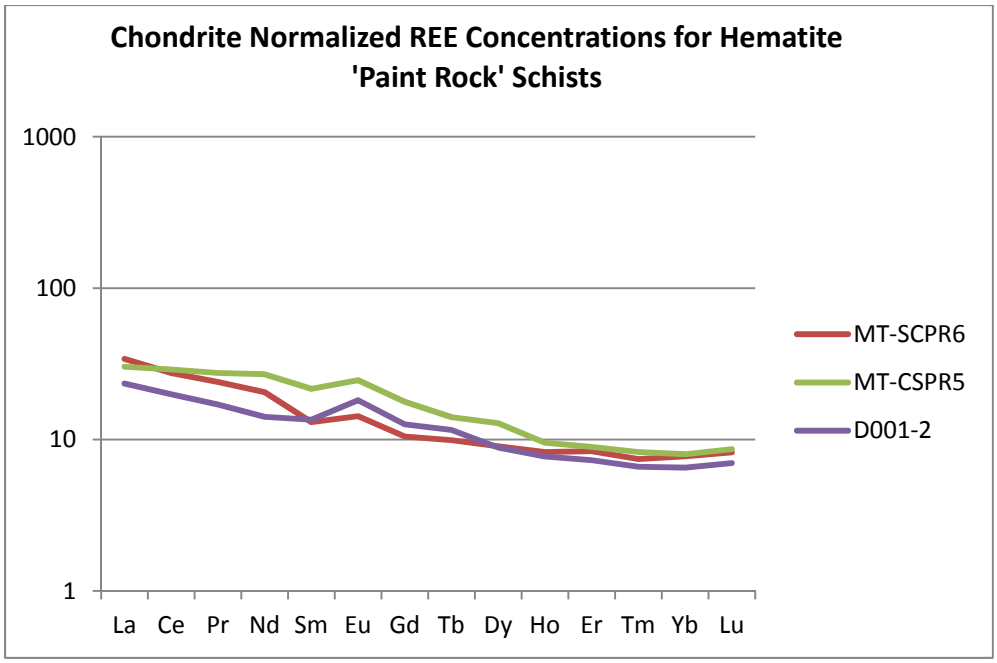

Figure 28. C1 chondrite normalized REE concentrations of primary and secondary sericite replaced by hematite alteration. Samples D001-2 and MT-SCPR6 consist of hematite replacing primary sericite/paragonite alteration. Sample MT-CSPR5 consists of hematite replacing secondary sericite alteration.

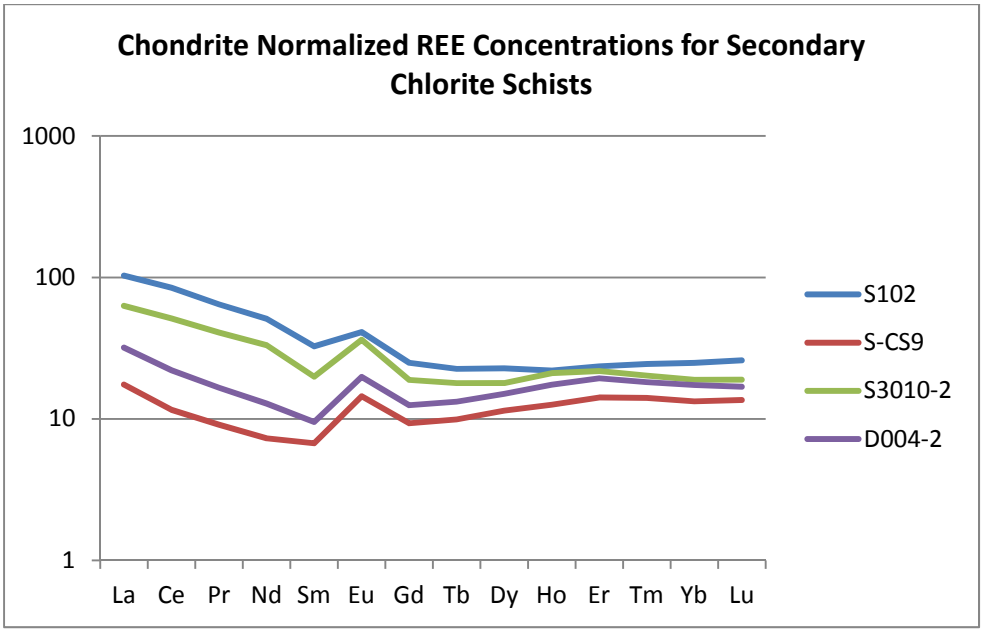

Figure 29. C1 chondrite normalized REE concentrations of Fe-chlorite schists enveloping and included in hematite ore.

Eu/Eu* and La/Lu values

Eu occurs in solution in either the 2+ or 3+ valence state, and is dependent on the redox conditions Peter et al., 2003). In natural systems, Eu^{3+} can be reduced to Eu^{2+}, leading to the fractionation of Eu from the other REE (Bau, 1991). Eu^{3+}/Eu^{2+} redox potential is most strongly tied to changes in temperature, with equilibrium shifting towards higher f_{O2} with increasing temperature. The Eu anomaly has been defined by Mclennan (1989) as: $Eu/Eu^* = Eu_n/(Sm_n*Gd_n)^{0.5}$, where *n* is the chondrite normalizing value. Early alteration assemblages (Mg-chlorite, paragonite/sericite, and secondary sericite) are associated with similar enrichment of Eu and LREE relative to the HREE, with Eu/Eu* values ranging 0.78-1.4 and average La/Lu values of 5.17. Hematite alteration is associated with similar gains in the LREE and HREE, with slight enrichment of Eu (Eu/Eu* = 1.15-1.4) and average La/Lu values down slightly to 3.66. Fe-chlorite alteration produced moderately positive Eu/Eu* values ranging 1.44-1.87 and enrichment of the HREE relative to the immobile LREE, lowering the La/Lu ratio to an average of 2.62.

Discussion

Paragenetic Sequence

Conversion of the magnetite-chert and altered hematite-jasper BIF to massive hematite most likely began with early D_2 deformation as evidenced by ore being restricted to the Mine Trend Shear Zone (MTSZ). Early deformation is associated with sericite/paragonite/silica and Mg-rich chlorite alteration possibly due to synvolcanic seafloor hydrothermal convection prior to the development of the MTSZ. With increasing subduction, metamorphic hydrothermal waters may have been produced by dehydration of volcanics lower in the strata. These early metamorphic, hydrothermal fluids may have been lower temperature fluids (250-300 °C), as indicated by the slightly negative to absent Eu anomalies (primary volcanic REE patterns). Eu most likely occurred in its trivalent state during these early alteration stages, signifying a lower temperature fluid. Fluids would have been drawn in and focused within the hematite breccia zones associated with local sericite alteration replacing earlier regional sericite/paragonite/silica- and Mg-rich chlorite altered schists. As observed by Klinger (1960), structural thinnings of the BIF controlled by narrow ductally deforming shear zones appears to be the main control of ore deposition. This is observed at the eastern extent of the Montana Ore Zone, where microbanded BIF occurs as a product of silica removal at the intersection of two narrow sericite/chlorite shear zones. A siliceous halo with heavy quartz veining exists proximal to microbanded ore as a by-product of

this silica removal from the BIF. Wall rock alteration outside this siliceous zone transitions to the moderately foliated primary Mg-chlorite + sericite schists.

Following the local leaching of silica from the japser-BIF, iron mobility is observed by its addition to both silica depleted BIF and adjacent wall rock. Within schists in contact with ore, secondary Fe-chlorite also occurs as a product of this iron mobility. Locally microcrystalline hematite 'paint rock' overprints secondary sericite and primary chlorite alteration intermediate to the hematite ore. This later hydrothermal fluid was most likely a higher temperature fluid (>300 °C), which would be required to produce the moderate positive Eu anomalies associated with hematite and Fe-chlorite alteration. As indicated by Bau (1991) and Peters (2003), the reduction of Eu to its divalent state is driven predominantly by a shift of the hydrothermal system to temperatures greater than 300 °C. The reducing nature of the system, indicated by a lack of oxidized minerals such as goethite, seems to indicate Fe mobility was driven by changes to the pH of the fluid. A sufficiently acidic fluid would be required to produce the saturated Fe concentrations that must have been present to produce the hematite altered schists.

Late stage D_2 deformation is associated with secondary Fe-chlorite replacing secondary sericite, within a narrow zone enveloping the hematite ore. Fe-chlorite occurs with quartz lining vein and vug walls within the massive ore. Microplaty hematite (MpHem) also occurs along vein and vug walls within the ore and in breccia zones. Hematite 'paint rock' alteration does not appear to overprint the late Fe-chlorite altered schists.

Massive hematite ore restricted within a narrow zone in the jasper-BIF indicates fluid was concentrated along structurally controlled fluid conduits during early syntectonic alteration of interlayered basalts within the banded iron formation. Laminated microbanded ore formed as a result of silica leaching focused at shear-zones where structural thinnings of the jasper-BIF occurred. Late-stage syn-tectonic alteration is associated with iron mobility resulting in hematite precipitation and Fe-chlorite alteration. Wall rock alteration is less pervasive during this stage, possibly due to fluid being drawn into and focused along early-forming breccia zones during the break-up of the microbanded hematite lenses of ore into smaller ore breccia zones.

The paragenetic sequence, illustrated below in figure 30, is thus: 1) Primary sericite/paragonite and Mg-rich chlorite alteration of the Ely basalts, associated with seafloor hydrothermal alteration. This stage of alteration may be associated with the formation of the carbonate-facies BIF (ankerite/hematite and siderite/magnetite) and calcite stringer veins in metavolcanics

observed within the MTSZ. 2) Local potassic alteration possibly associated with the conversion of magnetite-siderite BIF to martite/hematite/jasper BIF. During this stage, metamorphic fluids, restricted by deforming interlayered basalts within the BIF, leached silicate minerals from the BIF and produced a siliceous halo along the margins of the ore breccia zones. 3) Hematite 'paint rock' replacing primary Mg-rich chlorite and sericite alteration along the margins of ore breccia zones. 4) Fe-rich chlorite alteration forming within a narrow zone proximal to the hematite ore lenses.

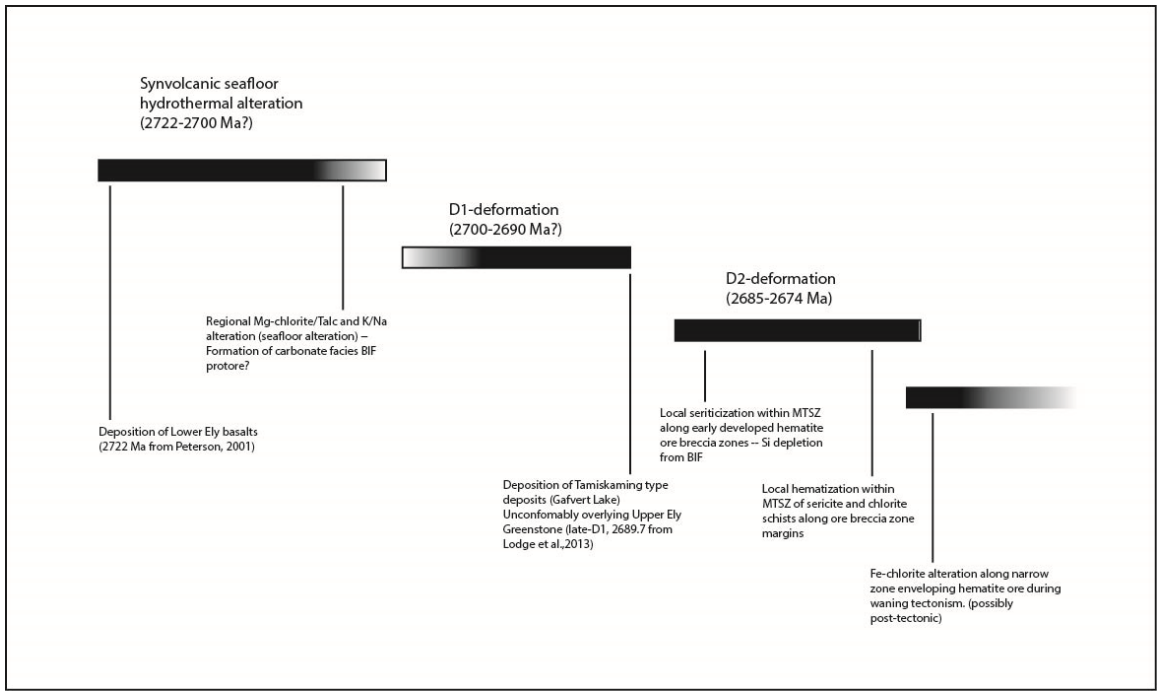

Figure 30. Paragenetic sequence for the upgrading of jasper/hematite BIF to massive hematite ore.

Shearing appears to be dominated by the intensely foliated sub-mylonitic sericite/paragonite/silica schist, which is interpreted to represent the primary alteration present prior to the upgrading of BIF to hematite ore. The high-strain shear zones separate the brittlely deformed ore breccias from surrounding weakly to moderately foliated schist n' BIF and fragmental schists. Silica removal from BIF during potassic alteration results in silicification of meta-volcanics along ore breccia zone margins. As stress was stored within the system the laminated ore began to fracture and form breccia zones joining the smaller pockets of ore. Strain on the system was lost as these breccia zones matured leading to a drop in pressure and the precipitation of silica.

A second system of higher temperature, metamorphic fluids may have been introduced as this fracture system translated to greater depths. Weakly foliated Fe-rich chlorite occurring as fine-

grained aggregates, replaces secondary sericite alteration within the schist in contact with ore. In the breccia zones, subhedral pyrrhotite appears to replace pyrite as possible evidence for a transition to a higher temperature fluid (Figure 31). Two stages of iron mobility is observed by the addition of MpHem and Mt grains up to 1 mm in size occurring within chlorite schist in contact with hematite ore, essentially wiping out any structural contacts.

Schist 'n' BIF surrounds the ore breccia systems as a ductilely deformed sequence dominated by chlorite and sericite schists with narrow lenses of jasper-BIF. Intermediate to the ore, at the ore breccia zone boundaries, secondary sericite Mg-rich chlorite. Also intermediate to hematite ore lenses, Cu-sulphide stringer veins and disseminated chalcopyrite occur along major shear contacts. The minor Cu mineralization observed at Soudan may have been associated with the fluids responsible for the upgrading of BIF to hematite ore, or it may represent the remobilization of early synvolcanic mineralization during syntectonic metasomatism.

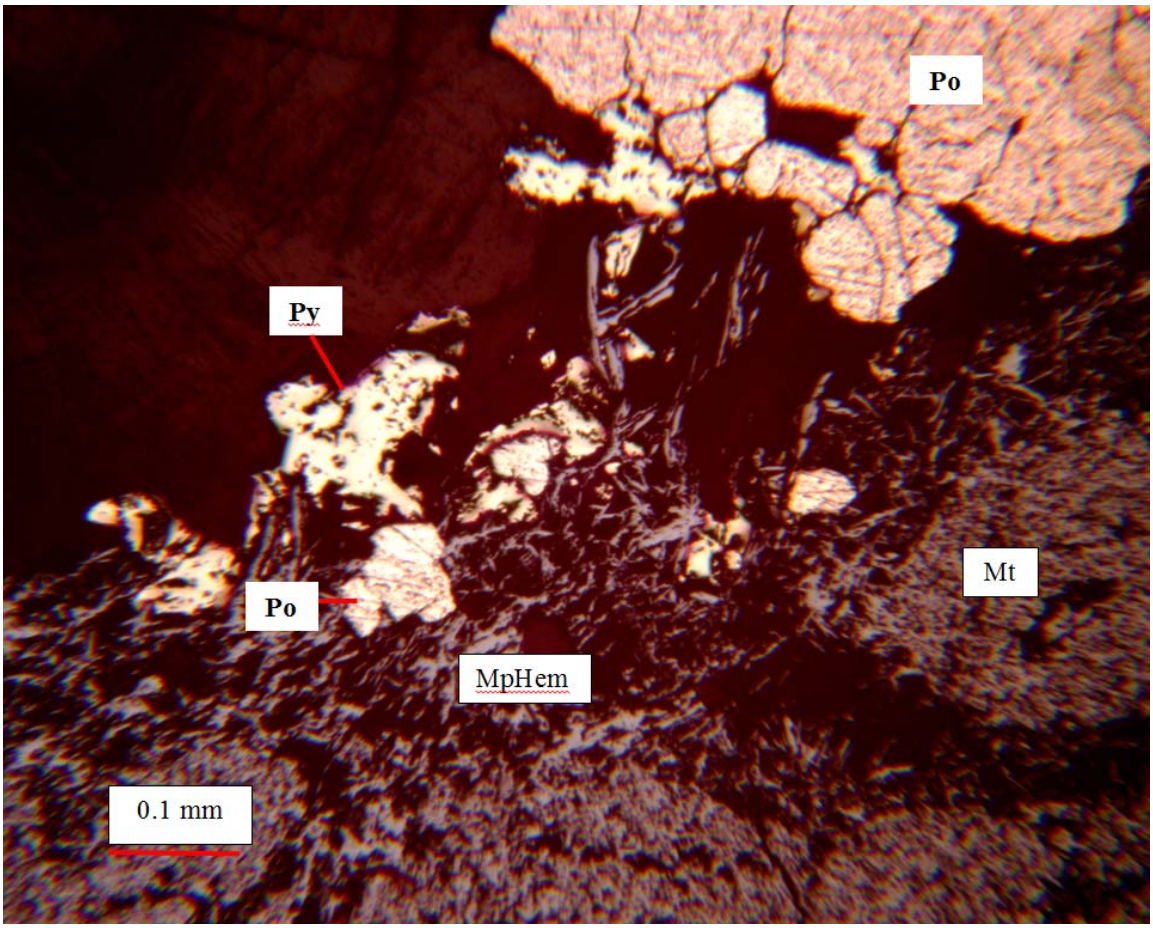

Figure 31. Reflected light image of sample S3017 showing subhedral pyrrhotite (Po) replacing anhedral pyrite (Py) in ore breccia zone with martite (mt) and microplaty hematite (MpHem).

Conclusion

Clout and Simonson (2005) classify iron formation-hosted iron ore deposits into three categories: (1) primary iron formation with typically 30 to 45 wt percent Fe, (2) martite-goethite ore with abundant hydrous iron oxides with roughly 56 to 63 wt percent Fe, and (3) high-grade hematite ores with 60 to 68 wt percent Fe. Primary iron formation, formed during syngenetic and diagenetic processes, appears to be associated with extensional tectonism. Supergene processes are generally accepted to be responsible for the formation of martite-goethite ores at Pilbara Marra Mamba and Brockman deposits in Western Australia (Taylor et al., 2001; Clout, 2002; Dalstra and Guedes, 2004). Supergene processes are also invoked to explain the formation of the soft, high-grade hematite Quadrilatero Ferrifero deposits in Brazil (Guedes et al., 2002; Pires, 2002; Spier et al., 2003; Rosiere and Rios, 2004). Microplaty hematite ores, such as Soudan

hematite, are thought to have formed by the replacement of carbonate and silicate minerals by metamorphic or magmatic hydrothermal fluids (Clout and Simonson, 2005).

Dalstra and Guedes (2004) emphasize the importance of magnetite-carbonate-amphibole, magnetite-carbonate, and hematite-carbonate percursors in the formation of high-grade hematite ores worldwide. They characterize protores to massive hematite as: 1) deep protores, formed at the highest temperatures and characterized by reduced magnetite-amphibole-siderite assemblages (Krivoy Rog); 2) intermediate protores, having a combination of reduced magnetite-siderite and oxidized hematite-ankerite assemblages (Mt. Tom Price) and; 3) shallowest and coolest protores, characterized by oxidized hematite-dolomite assemblages (Carajas, Thabazimbi). Their proposed genetic model suggests early hydrothermal depletion of silica in the host iron formation and introduction of carbonates, followed by supergene leaching of the carbonates to form high-grade hematite ore (Dalstra and Guedes, 2004).

At Soudan, the presence of both magnetite-siderite and hematite-ankerite precursors, along with intense Mg-Fe alteration to volcanics in the form of carbonate, chlorite, and talc (Klinger, 1960; Dahlberg et al., 1989) indicates these early hydrothermal systems were fluid dominated at temperatures ranging 150° to >300 °C. This mineral assemblage indicates that these were intermediate protore deposits. However, the removal of carbonate and silicate minerals from BIF protore at Soudan during the formation of massive hematite most likely resulted from the interaction of host-rock with hydrothermal metamorphic fluids associated with the subduction of the Soudan Member basalt and oxide facies BIF.

Klinger (1960) suggested a volume-for-volume replacement of iron formation by hematite due to a lack of porosity or the existence of slump structures within the hematite ore at Soudan. However, the isocon analysis indicates a 39% volume loss during the upgrading of altered jasper banded iron formation to microbanded ore as a result of Si depletion. The isocon analysis also shows a 9% mass gain in Fe during BIF upgrading to hematite ore. The upgrading of jasper-hematite BIF to ore can be seen as a two-stage process. Silicate minerals were first leached from the BIF, associated with potassic alteration and silicification of wall rock adjacent to ore. Subsequent iron mobility resulted in iron addition to the ore and the formation of secondary Fe-chlorite and hematite ‘paint rock’ alteration of schists proximal to hematite ore. Ore breccia zones exist between lenses of ore as the main fluid conduits associated with late hematite and secondary Fe-chlorite alteration.

Potassic altered volcanic wall rocks adjacent to ore are enriched in the LREE, while early forming ore breccia is depleted in LREE. The strong correlation between CaO, P2O5, and the LREE (particularly La, Ce, and Nd) during the upgrading of BIF to ore indicates that LREE mobility may be a product of sorption processes occurring during the removal of apatite from BIF. This stage of ore-upgrading is also associated with immobile HREE.

Iron enrichment resulting in the formation of hematite 'paint rock' schists within the ore breccia system may have been a reaction to a drop in pH. Both LREE and HREE mass gains match that of the overall mass gain (33%) of wall rock altered to hematite 'paint rock'. Fe-enrichment within the ore breccia zones is further indicated by a transition from Mg-rich chlorites outside the breccia zones to Fe-rich chlorites proximal to ore as indicated by the SEM analyses. Secondary chlorite alteration is not associated with any upgrading of the hematite ore as indicated by the isocon analysis (Figure 22). This late-stage alteration shows HREE-enrichment and a stronger positive Eu anomaly with relatively immobile LREE, and appears to occur during a period of waning tectonism as indicated by a lack of structural contacts between hematite ore and secondary chlorite schists.

An increase of the water/rock ratio may have resulted from the development of secondary permeability zones formed due to the 39% volume loss in BIF. HREE mobility could be explained by this higher water/rock ratio, as precipitation of secondary minerals from a fluid with a predominance of REE-complexes could lead to enrichment of the HREE. However, these were most likely reducing, moderately acidic, and higher temperature fluids, which would be required for Eu to be present in its divalent state ($Eu/Eu^* > 1$) and to produce an Fe-saturated solution.

Early seafloor hydrothermal alteration is pervasive throughout the shear zone, as the meta-basalts have all been altered to Mg-rich chlorite and sericite/paragonite/silica schists. Very little remnants of earlier calcic alteration associated with synvolcanic seafloor hydrothermal systems remains within the MTSZ. Early K-enrichment of the Soudan Member, observed in sericite/paragonite/silica schists, may have been a result of the fluid-dominated synvolcanic hydrothermal system. With increasing subduction the development of a K-rich, metamorphic hydrothermal fluid may have led to the local potassic alteration (pink sericite schists) resulting from fluid focusing along structurally controlled conduits. These structurally controlled thinnings of the BIF are the sites for the sericitization of meta-basalts along the margins of early forming hematite ore breccia zones. During this stage of alteration, silicate minerals were removed from

the BIF under high pressure (3-4 kb) and lower temperatures (250-300 °C). Ductile deformation of the meta-basalts led to the eventual brittle 'failure' of the silica-depleted BIF. As the laminated hematite ore began to fracture across the system the pressure within this breccia zone would have drastically decreased, leading to the precipitation of silica as smoky 'bull quartz' and the silicification of the sericitic schists in contacts with the hematite ore. As these structure systems translated to greater depths, a higher temperature, lower pH fluid would have been necessary, in this reducing system, to transport the Fe required for the formation of the hematite schists and Fe-chlorite observed within a narrow zone around the hematite ore bodies. This late system was less pervasive, as fluids were drawn in from surrounding wall rock to this low pressure, high permeability zone. The mineralogy throughout the hematite ore breccia zone, from the surface down to the 27th level (~0.5 mile depth) is rather homogenous, with only minor variations to wall rock alteration proximal to ore occurrences. The conditions at which the hematite ore formed throughout the breccia system must therefore have been relatively similar, with a low pressure and temperature gradient across the system.

The source and characteristics of these two hydrothermal systems remains enigmatic, as the pressure and temperature conditions these fluids were under remain rather poorly constrained. The pH/Eh conditions appear to favor a reducing/acidic fluid, however further work is needed to try and buffer these systems. Fluid inclusion studies could help constrain the temperature and chemistry of the ore-forming fluids, while isotope analyses could shed light on their source.

References

Anders E. and Grevesse N. (1989). Abundances of the elements: Meteoritic and solar. *Geochimica et Cosmochimica Acta* (53), p. 197-214.

Angerer, Thomas, and Steffen G. Hagemann. The BIF-hosted high-grade iron ore deposits in the Archean Koolyanobbing greenstone belt, Western Australia: structural control on synorogenic-and weathering-related magnetite-, hematite-, and goethite-rich iron ore. *Economic Geology* 105.5 (2010): p. 917-945.

Angerer, T., Hagemann, S. G., and Danyushevsky, L. V. (2012). Geochemical evolution of the banded iron formation-hosted high-grade iron ore system in the Koolyanobbing greenstone belt, Western Australia. *Economic Geology*, *107*(4), p. 599-644.

Bau, M. (1991). Rare-earth element mobility during hydrothermal and metamorphic fluid-rock interaction and the significance of the oxidation state of europium. *Chemical Geology*, 93(3), p. 219-230.

Beard, B. L., and Johnson, C. M. (2004). Fe isotope variations in the modern and ancient earth and other planetary bodies. *Reviews in Mineralogy and Geochemistry*, 55(1), p. 319-357.

Beukes, N. J., Gutzmer, J., and Mukhopadhyay, J. (2003). The geology and genesis of high-grade hematite iron ore deposits. *Applied Earth Science: Transactions of the Institutions of Mining and Metallurgy: Section B*, 112(1), p.18-25.

Beukes, N. J., Mukhopadhyay, J., and Gutzmer, J. (2008). Genesis of high-grade iron ores of the Archean Iron Ore Group around Noamundi, India. *Economic Geology*, 103(2), p. 365-386.

Boerboom, T. J., and Zartman, R. E. (1993). Geology, geochemistry, and geochronology of the central Giants Range Batholith, northeastern Minnesota. *Canadian Journal of Earth Sciences,* v. 30, p. 2510-2522.

Clout, J. M. F., (2002). Upgrading processes in BIF-derived iron ore deposits—implications for ore genesis and downstream processing. Australasian Institute of Mining and Metallurgy Publication Series 7/2002, p. 237–242.

Clout, J. M. F., and Simonson, B. M. (2005). Precambrian iron formations and iron formation-hosted iron ore deposits. *Economic geology*, 100, p. 643-679.

Dahlberg, E. H., Peterson, D., and Frey, B. A. (1989). Drill Core Repository Sampling: Soudan Mine, NE Minnesota. Minnesota Department of Natural Resoures Project 265. 155 pages.

Dalstra, H., and Guedes, S. (2004). Giant hydrothermal hematite deposits with Mg-Fe metasomatism: a comparison of the Carajás, Hamersley, and other iron ores. *Economic Geology*, 99(8), p. 1793-1800.

Danielson, A., Möller, P., and Dulski, P. (1992). The europium anomalies in banded iron formations and the thermal history of the oceanic crust. *Chemical Geology*, 97(1), p. 89-100.

Figueiredo e Silva, R. C., Lobato, L. M., Rosière, C. A., and Hagemann, S. (2013). Petrographic and geochemical studies at giant Serra Norte iron ore deposits in the Carajás mineral province, Pará State, Brazil. *Revista Geonomos*, 19(2).

Grant, J. A. (1986). The isocon diagram; a simple solution to Gresens' equation for metasomatic alteration. *Economic Geology*, 81(8), p. 1976-1982.

Grant, J. A. (2005). Isocon analysis: a brief review of the method and applications. *Physics and Chemistry of the Earth,* Parts A/B/C, 30(17), p. 997-1004.

Green, J. C., Ojakangas, R. W., and Sims, P. K. (1970). Stratigraphy of the Lower Precambrian rocks in the Vermilion district, northeastern Minnesota. University of Minnesota.

Gross, G. A. (2009). Iron Formation in Canada, Genesis and Geochemistry. *Geological Survey of Canada*, Open file 5987, 164 pg, doi:10.4095/226638.

Guedes, S. C., Roseire, C. A., Barley, M., Lobato, L., 2002, Carbonate alteration associated with the Carajas high-grade hematite deposits, Brazil. In Proceedings of Iron Ore 2002, p. 62–65.

Gutzmer, J., Mukhopadhyay, J., Beukes, N. J., Pack, A., Hayashi, K., and Sharp, Z. D. (2006). Oxygen isotope composition of hematite and genesis of high-grade BIF-hosted iron ores. *Geological Society of America Memoirs*, 198, p. 257-268.

Hagemann, S., Dalstra, H. I., Hodkiewicz, P., Flis, M., Thorne, W., and McCuaig, C. (2007). Recent advances in BIF-related iron ore models and exploration strategies. In Proceedings of Exploration'07: Fifth Decennial International Conference on Mineral Exploration (B. Milkereit, ed.), Ore Deposits and Exploration Technology, Paper 54, 811 (Vol. 821).

Heim, N., Scott, H., Kilduff, R., Rahtz, C., Vial, A., Young, S., Mahr, C., and Hudak, G., (2011). Preliminary bedrock geology map of the eastern part of Lake Vermilion State Park, St. Louis County, NE Minnesota: Precambrian Research Center Map Series Map PRC/Map – 2010-01, 1:5000 scale.

Hudak, G. J., and Morton, R. L., (1999). Mineral Potential Study, Minnesota Department of Natural Resources Project 326, Bedrock and Glacial Drift Mapping for VMS and Lode Gold Alteration in the Vermilion – Big Fork Greenstone Belt, Part A: Discussion of Lithology, Alteration, and Geochemistry at the Five Mile Lake, Eagles Nest, and Quartz Hill Prospects: Minnesota Department of Natural Resources Division of Minerals Project 326 Report, 136 p.

Hudak, G. J., Heine, J., Newkirk, T., Odette, J., and Hauck, S., (2002a). Comparative geology, stratigraphy, and lithogeochemistry of the Fivemile Lake, Quartz Hill, and Skeleton Lake VMS occurrences, Vermilion District, NE Minnesota: A report to the Minerals Coordinating

Committee, DNR, Minerals Division, State of Minnesota: Natural Resources Research Institute Technical Report NRRI/TR-2002/03, 390 pages.

Hudak, G. J., Heine, J., Hocker, S. M., and Hauck, S., (2002b). Geological mapping of the Needleboy Lake – Sixmile Lake area, northeastern Minnesota: a summary of volcanogenic massive sulfide potential: Natural Resources Research Institute Report of Investigation NRRI/RI-2002/14, 15 p.

Hudak, G.J., Heine, J., Jirsa, M., Peterson, D., (2004). Volcanic stratigraphy, hydrothermal alteration, and VMS potential of the lower Ely Greenstone, Fivemile Lake to Sixmile Lake area; *in* Institute on Lake Superior Geology, 50th Annual Meeting, Thunder Bay, ON, v. 50, Part 2, pp. 1-44.

Hudak, G. J., Hoffman, A. T., Peterson, D. M., and Heine, J., (2007). Recent developments understanding the volcanic, magmatic, tectonic, and metallogenic evolution of the Ely Greenstone Formation, Vermilion District, NE Minnesota: 53rd Annual Meeting, Institute on Lake Superior Geology, Proceedings Volume 53, Part 1 – Program and Abstracts, p. 42-43.

Hudak, G., Heim, N., Scott, H., Kilduff, R., Vial, A., Rahtz, C., and Mahr, C. (2011). Lake Vermilion State Park Capstone Project.

Hudak, G. J., Heine, J., Lodge, R. W. D., and Jansen, A., (2012). Recent developments understanding the volcanic, magmatic, tectonic, and metallogenic evolution of the Ely Greenstone Formation, Vermilion District, NE Minnesota: Geological Association of Canada – Mineralogical Association of Canada, Abstracts and Programs, v. 35, p. 59.

Hudleston, P. J., Schultz-Ela, D., and Southwick, D. L. (1988). Transpression in an Archean greenstone belt, northern Minnesota. *Canadian Journal of Earth Sciences*, 25(7), p. 1060-1068.

Johnson, T. K. (2009). Structural, Kinematic, and Hydrothermal Fluid Investigation of the Gold-Bearing Murray Shear Zone, northeastern Minnesota: M.S. Thesis, University of Minnesota, Duluth, Minnesota, 133 p.

Klinger, F. L. (1960). Geology and ore deposits of the Soudan Mine, St. Louis County, Minnesota: Ph. D. dissertation, University of Wisconsin, Madison, Wisconsin, 96 p.

Lodge, R. W. D. (2013). Regional volcanogenic massive sulfide metallogeny of the Neoarchean greenstone belt assemblages on the northwest margin of the Wawa subprovince, Superior province: Ph. D. dissertation, Laurentian University, Sudbury, Ontario, 290 p.

Odette, J. D., Hudak, G. J., Suszek, T., and Hauck, S. A., (2001). Preliminary evaluation of hydrothermal alteration mineral assemblages and their relationship to VMS-style mineralization in the Five-Mile Lake area of the Archean Vermilion Greenstone Belt, NE Minnesota: Institute on Lake Superior Geology, 47th Annual Meeting, Proceedings Volume 47, Part 1 – Program and Abstracts, p.75-76.

Ohmoto, H. (2003). Nonredox transformations of magnetite-hematite in hydrothermal systems. *Economic Geology*, 98(1), p. 157-161.

Peterson, D. M., (2001). Development of Archean lode-gold and massive sulfide deposit exploration models using geographic information system applications: targeting mineral exploration in northeastern Minnesota from analysis of analog Canadian mining camps: unpublished Ph. D. dissertation, University of Minnesota, Duluth, Minnesota, 503 p.

Peterson, D. M., Gallup, C., Jirsa, M. A., and Davis, D. W., (2001). Correlation of Archean assemblages across the U.S. – Canadian border: Phase I geochronology: 47th Annual Meeting, Institute on Lake Superior Geology, Proceedings Volume 47, Part 1 – Programs and Abstracts, p. 77-78.

Peterson, D. M., and Patelke, R. L., (2003). National Underground Science and Engineering Laboratory (NUSEL): Geological site investigation for the Soudan Mine, northeastern Minnesota: Natural Resources Research Institute Technical Report NRRI/TR-2003/29, 88 p.a.

Pires, F. R. M., (2002). Distribution of hard hematite ore at the Quadrilatero Ferrifero, Minas Gerais, Brazil and its possible genetic significance. In Proceedings of Iron Ore 2002, p. 71–76.

Radakovich, A. L., Parent, C. T., Partridge, M. E., Ritts, A. D., Pierce, R., and Hudak, G. J., (2010). Reconnaissance bedrock geological map of the northern part of Soudan Underground Mine State Park and the northwestern part of Lake Vermilion State Park, St. Louis County, Minnesota: Precambrian Research Center Map Series Map PRC/Map – 2010-04, 1:5000 scale.

Rasmussen, B., Fletcher, I. R., Muhling, J. R., Thorne, W. S., & Broadbent, G. C. (2007). Prolonged history of episodic fluid flow in giant hematite ore bodies: evidence from in situ U–Pb geochronology of hydrothermal xenotime. *Earth and Planetary Science Letters*, 258(1), p. 249-259.

Rollinson, H. R. (1993). Using geochemical data: evaluation, presentation, interpretation. Routledge.

Rosière, C. A., and Rios, F. J. (2004). The Origin of Hematite in High-Grade Iron Ores based in Infrared Microscopy and Fluid Inclusion Studies: The Example of the Conceição Deposit, Quadrilátero Ferrífero, Brazil. *Economic Geology*, 99, p. 611-624.

Roy, S., & Venkatesh, A. S. (2009). Mineralogy and geochemistry of banded iron formation and iron ores from eastern India with implications on their genesis. *Journal of Earth System Science*, 118(6), p. 619-641.

Schwartz, G. M., and Reid, I. L. (1954). Replacement and Rock Alteration in the Soudan Iron Ore Deposit, Minnesota. AIME.

SIMS, P. K. (1976). Early Precambrian tectonic-igneous evolution in the Vermilion district, northeastern Minnesota. *Geological Society of America Bulletin*, 87(3), p. 379-389.

Spier, C. A., Oliveira, S. M. B., and Rosire, C. A. (2003). Geology and geochemistry of the Águas Claras and Pico iron mines. Quadrilátero Ferrífero, Minas Gerais, Barzil. *Mineralium Deposita*, 38, p. 751-774.

Stott, G., and Mueller, W., (2009). Superior Province: The nature and evolution of the Archean continental lithosphere: Precambrian Research, v. 168.

Taylor, D. H., Dalstra, J. A., Harding, E. G., Broadbent, C., and Barley, M. E. (2001). Genesis of high-grade hematite orebodies of the Hamersley Province, Western Australia. *Economic Geology*, 96, p. 837–873.

Thorne, W., Hagemann, S., Vennemann, T., and Oliver, N. (2009). Oxygen isotope compositions of iron oxides from high-grade BIF-hosted iron ore deposits of the Central Hamersley Province, Western Australia: Constraints on the evolution of hydrothermal fluids. *Economic Geology*, 104(7), p. 1019-1035.

Webb, A. D., Dickens, G. R., and Oliver, N. H. (2004). Carbonate alteration of the Upper Mount McRae Shale beneath the martite-microplaty hematite ore deposit at Mount Whaleback, Western Australia. *Mineralium Deposita*, 39(5-6), p. 632-645.

Vallowe, A. M., Thalhamer, E. J., Rhoades, D. L., and Peterson, D. M., (2010). Surface and subsurface geologic maps of the Soudan Underground Mine State Park, St. Louis County, northeastern, Minnesota: Precambrian Research Center Map Series Map PRC/Map – 2010-01, 1:2500 and 1:5000 scale.

Varajão, C. A., Bruand, A., Ramanaidou, E. R., and Gilkes, R. J. (2002). Microporosity of BIF hosted massive hematite ore, Iron Quadrangle, Brazil. *Anais da Academia Brasileira de Ciências*, 74(1), p. 113-126.

Williams-Jones, A. E., Migdisov, A. A., and Samson, I. M. (2012). Hydrothermal mobilisation of the rare earth elements–a tale of "ceria" and "yttria". *Elements*, 8(5), p. 355-360.

APPENDIX A

PETROGRAPHIC ANALYSES

MT3007 Fe/Mg-Chlorite + Quartz + Fe-Oxides

Weakly foliated fine-grained aggregates of Fe/Mg-chlorite + quartz occurring in fine-grained chlorite matrix with euhedral martite grains up to 0.1 mm throughout ~ 10-15% Fe-oxides, showing local foliation through aggregate mineral grain alignment along dominant shear zones

MT 3003 Sericite + Quartz > Fe-Chlorite + Hematite

Pervasive well foliated sericite alteration enveloping fine-grained disseminated Quartz + Sericite + Pyrophyllite replacing K-spar showing less degree of foliation. Secondary Fe-Chlorite fiamme throughout parallel to foliation with associated anhedral to subhedral tabular Microplaty hematite. Late cross-cutting vein of chlorite showing slight off-setting due to shearing.

MT 2001 Sericte >> Fe-Chlorite + Fe-Oxide + Quartz

Pervasive sericite + pyrophyllite alteration with minor amount of secondary Fe-chlorite and quartz. Fe-oxides associated with areas of high shear (foliation planes) predominantly anhedral to subhedral martite and hematite with minor amounts of Mphem showing mineral alignment along shears.

D 2009 Microbanded Hematite Ore

Alternating bands of coarse (up to 1mm) , dense subhedral martite bands and more porous microcrystalline hematite (Mihem) with minor amorphous hematite grains. Mihem bands show slump structures (photo) and pinching out in areas

D 2014 Microbanded Hematite Ore

Coarse, dense martite/Mphem bands alternating with more porous anhedral hematite/Mihem bands with minor subhedral grains of martite 0.1-0.5 mm. Shearing occurs along banding boundaries indicated by mineral grain alignment (photo). Late cross-cutting quartz/Fe-Chlorite viens with Mphem precipitating on vein walls.

D2001 Microbanded hematite ore + Microplaty hematite

Remnant banding of dense aggregate massive subhedral martite + hematite ore and fine-grained anhedral hematite + Mihem, cut by porous ore breccia consisting of randomly oriented, coarse Mphem and Martite, coarse Mphem associated with veining cutting banding

D2010 Hematite + chlorite + quartz

Primary Mihem (Paint Rock) alteration with minor amounts (<5%) subhedral martite grains up to 0.1 mm. Secondary chlorite + quartz alteration occurring as veins and coarse aggregates

D2012 Sericite > Fe-Chorite + Quartz +/- Fe_Oxides

Primary selective pervasive, fine-grained and weakly foliated sericite alteration replacing fine-grained aggregates of Fe-Chlorite and coarse anhedral quartz. Minor Fe-Oxides (~5%) occurring as subhedral martite and tabular hematite associated with chlorite alteration.

S3010 Fe/Mg Chlorite + Quartz > Sericite

Disseminated flakes of Fe/Mg-Chlorite with minor quartz replacing weakly foliated fine-grained sericite. Fe/Mg-Chlorite also occurring as veins cutting foliation.

S3013 Altered Banded Iron Formation

Dense martite microbands with siliceous chert microbands being replaced by microcrystalline hematite and coarser irregular hematite. Sulfides occurring within chert replacement bands in the form of anhedral to subhedral pyrite and minor chalcopyrite.

MT2003 Fe-Depleted Microbanded Banded Iron Formation

Microbands of siliceous chert with fine quartz and microcrystalline hematite. Late quartz veins cutting banding with secondary fine-grained irregular hematite occurring with disseminated Fe-chlorite.

D2009 Microbanded Hematite Ore

Microbands of coarse, irregular hematite/martite (Pseudo morph bands) alternating with microbands of fine to microcrystalline hematite with recrystallized quartz (Replacement bands). Replacement bands pinchout in places and show minor slump structures with coarser hematite/martite cutting fine-grained bands.

D2016 Microbanded ore with late MpHem

Coarse martite microbands alternating with fine-grained anhedral hematite. Cut by later coarse MpHem occurring with secondary fine quartz and microcrystalline hematite.

S3015 Less altered Banded Iron Formation

Micro to Meso-banded jasper BIF with bands up to 1 cm in width. Oxide bands characterized by coarse grains of martite up to 0.1 mm with fine-grained, irregular hematite averaging 0.01 mm. Halo of microcrystalline hematite chert surrounds oxide bands. Alternating bands of siliceous chert with minor hematite/martite grains. Late secondary quartz veins cuts banding.

S102 Fe-chlorite + Fe-oxides

Fine-grained chlorite, with light-green to yellow pleochroism and light-blue birefringence colors. Disseminated grains of sub-euhedral martite grains up to 0.1 mm, with later concentrated MpHem (0.01-0.05 mm) cutting foliation.

D001 Sericite + Paragonite? +/- Pyrrophyllite + Quartz >> Chlorite + Hematite

Moderately foliated, fine-grained sericite/paragonite? schist replacing fine-grained chlorite, with quartz displaying bulging recrystallization and mineral grain alignment. Locally fine-grained microcrystalline hematite replaces chlorite, with some hematite alteration occurring along microfractures cutting foliation.

D003 Sericite + Paragonite? +/- Pyrrophyllite + Quartz >> Chlorite + Hematite

Strongly foliated, fine-grained sericite/paragonite schist with spaced cleavage domains up to 30-40 vol%. Primary chlorite occurring along cleavage domains, with minor quartz showing strong mineral alignment. Locally hematite alteration occurs along shear and microfractures.

D002 Sericite/Chlorite altered Debris Flow

Moderately foliated debris flow, with clasts showing grain alignment along foliation. Clasts grain sizes from 1 mm up to > 1 cm with selectively-pervasive replacement by sericite. Fine-grained chlorite/sericite matrix, with veins of recrystallized quartz and disseminated flakes of chlorite showing strong pleochroism from light yellow to light green.

S3017 Ore Breccia with sulfides

Hematite ore breccia with martite altering to hematite along grain boundaries. Quartz veins lined with secondary microplaty hematite occurring with sulfides in the form of anhedral pyrite and sub to euhedral pyrrhotite.

S104 Ore breccia + chlorite

Coarse subhedral martite grains (0.1 mm) oxidizing to hematite along grain boundaries, within fine-grained irregular hematite matrix. Later, coarse microplaty hematite occurring along fracture and vug walls. Chlorite occurring as disseminated flakes and quartz also present with microplaty hematite.

S106 Hematite/Jasper BIF

Oxide bands consist of alternating layers of coarse, euhedral martite and microcrystalline hematite. Silicate bands consist of fine-grained Fe-silicate minerals, with heavy iron ‘staining’ of silicate minerals in contact with oxide bands. Banding offset by fractures with coarse, irregular hematite and chlorite occurring as disseminated flakes showing weak pleochroism and birefringence from pale yellow to dark green.

S2002 Ore breccia + chlorite

Dense bands of subhedral matite (0.1-0.2 mm) alternating with bands of fine-grained, microplaty hematite occurring within a microcrystalline hematite matrix. In contact with chlorite schist, showing moderate foliation. Chlorite displays weak pleochroism from light yellow to light green, with light blue birefringence.

D2008 Ore breccia + chlorite

Dense martite with intergrown microplaty hematite within a fine-grained hematite matrix. Very little remnants of banding still observed. Microplaty hematite occurring along vein walls with quartz and micaceous chlorite. Chlorite displays weak pleochroism from yellow to green and bluish-green birefringence.

S3014 Ore breccia + chlorite

Porous subhedral martite, with fine-grained microplaty hematite occurring with chlorite within veins and vugs. Chlorite occurs as coarse, disseminated flakes, with weak pleochroism from light yellow to green and bluish-green birefringence.

APPENDIX B
GEOCHEMISTRY DATA

GEOCHEMISTRY DATA	Method	WGHT	LF200	LF200	LF200	LF200	LF200	LF200	LF200	LF200	LF200	LF200	LF200	LF200	LF200	LF200	LF200
	Analyte	Wgt	SiO2	Al2O3	Fe2O3	MgO	CaO	Na2O	K2O	TiO2	P2O5	MnO	Cr2O3	Ni	Sc	LOI	Sum
	Unit	KG	%	%	%	%	%	%	%	%	%	%	%	PPM	PPM	%	%
	Detection Limit	0.01	0.01	0.01	0.04	0.01	0.01	0.01	0.01	0.01	0.01	0.01	0.002	20	1	-5.1	0.01
Sample	Lithology																
D003	Sericite/Paragonite	0.02	60.26	19.21	9.91	1.5	0.06	1.17	2.91	0.83	<0.01	0.05	0.02	89	28	4	99.94
D004	Ore	0.03	2.22	1.7	93.55	0.82	0.12	0.02	<0.01	0.03	0.04	0.06	<0.002	71	4	1.4	99.96
D004-2	Fe-Chlorite	0.03	29.54	22.18	26.66	9.99	0.09	0.07	1.38	0.9	<0.01	0.2	0.023	83	29	8.7	99.77
D2001	Ore	0.05	0.43	0.27	98.15	0.01	0.51	0.01	0.01	<0.01	0.35	0.02	0.007	75	1	0.2	99.99
D2009	Ore	0.04	4.5	0.27	94.79	0.01	0.09	0.01	<0.01	0.02	0.06	0.03	0.002	44	2	0.2	99.99
D2010	Hematite+Chlorite	0.11	41.04	12.68	31.73	7.42	0.1	0.02	0.01	0.6	0.05	0.16	0.021	89	16	6	99.84
D2014	Ore	0.17	0.73	0.19	98.59	0.02	0.02	0.01	<0.01	<0.01	<0.01	0.01	0.002	<20	<1	0.4	99.98
D2015	BIF	0.06	31.36	0.14	68.09	0.03	0.04	<0.01	<0.01	<0.01	<0.01	<0.01	0.009	<20	<1	0.3	100
D2016	Ore	0.04	1.23	0.43	97.23	0.1	0.24	0.03	<0.01	<0.01	0.15	0.02	<0.002	31	1	0.5	99.96
D2017	Hematite+Chlorite	0.07	26.82	14.39	43.54	6.99	0.17	0.04	0.02	0.67	0.08	0.16	0.023	146	21	6.9	99.81
D2018	Chlorite	0.14	47.38	15.39	21.02	7.27	0.05	0.02	1.62	0.66	<0.01	0.13	0.025	43	25	6.2	99.81
D2019	BIF	0.09	29.85	1.06	66.57	0.39	0.79	0.03	0.02	0.02	0.52	0.02	0.003	58	2	0.7	99.99
D2020	BIF	0.04	50.81	0.16	48.69	0.04	0.11	<0.01	<0.01	<0.01	0.06	0.01	0.006	<20	<1	0.1	100.01
D001	Sericite/Paragonite	0.03	70.93	15.23	6.88	0.45	0.07	1.18	1.78	0.65	0.03	0.02	0.027	64	17	2.7	99.96
D001-2	Hematite+Sericite	0.07	62.44	13.41	18.21	0.25	0.06	1.23	1.18	0.61	<0.01	0.02	0.021	56	19	2.5	99.95
S102	Fe-Chlorite	0.04	20.82	15.15	47.84	8.47	0.06	0.02	0.03	0.23	<0.01	0.2	<0.002	151	8	6.9	99.75
S104	Ore	0.06	0.63	0.25	98.38	0.04	0.07	0.02	<0.01	<0.01	0.03	0.02	0.005	28	1	0.5	99.97
S105	Ore	0.1	0.97	0.57	91.64	0.16	3.48	0.05	<0.01	<0.01	2.44	0.03	0.003	60	2	0.6	99.96
S106	BIF	0.14	27.44	0.76	70.63	0.3	0.25	0.02	<0.01	<0.01	0.14	0.02	0.009	54	1	0.4	99.99
S107	Ore	0.06	3.37	0.21	95.39	0.05	0.19	0.03	<0.01	<0.01	0.09	0.02	0.004	20	2	0.6	99.97
S3010	Ore	0.23	1.98	1.51	92.97	0.68	0.66	0.02	<0.01	<0.01	0.5	0.05	0.012	75	3	1.6	99.95
S3010-2	Fe-Chlorite	0.16	30.97	19.98	28.15	10.02	0.07	0.03	1.66	0.88	<0.01	0.19	0.027	93	29	7.8	99.75
S3011	BIF	0.07	45.09	0.3	54.14	0.13	0.08	<0.01	0.02	0.01	0.03	0.01	0.008	<20	<1	0.2	100.01
S3012	Ore	0.05	8.52	0.65	89.96	0.19	0.02	0.03	<0.01	<0.01	<0.01	0.02	0.002	<20	2	0.6	99.98
S3014	Ore	0.07	2.57	1.86	92.74	0.99	0.15	0.01	<0.01	0.06	0.06	0.05	0.005	47	3	1.4	99.95
S3018	Ore	0.13	13.37	0.56	83.51	0.16	1.19	0.02	<0.01	0.04	0.8	0.02	0.007	91	2	0.3	99.99
MT2001	Sericite+Chlorite	0.03	57.47	17.23	11.58	3.16	0.26	0.05	4.91	0.63	0.17	0.05	0.045	352	26	4.3	99.89
MT2003	BIF	0.02	73.61	0.43	25.38	0.19	0.03	<0.01	0.01	<0.01	0.01	0.02	0.011	<20	1	0.3	100.01
MT3002	Sericite+Chlorite	0.13	50.74	20.7	12.79	3.74	0.04	0.05	6.66	0.79	<0.01	0.05	0.041	50	35	4.2	99.84
MT3003	Sericite+Chlorite	0.02	50.88	18.02	12.61	7.11	0.16	0.04	4.28	0.78	0.09	0.04	0.035	203	29	5.7	99.8
MT3004	BIF	0.16	34.12	0.46	64.58	0.27	0.03	<0.01	0.02	<0.01	<0.01	0.01	0.009	<20	1	0.5	100
MT3007	Fe-Chlorite	0.29	42.52	13.8	27.28	8.83	0.04	0.01	0.02	0.58	<0.01	0.16	<0.002	48	9	6.6	99.8
MT3008	BIF	0.49	36.83	0.33	61.82	0.14	0.03	<0.01	0.01	<0.01	<0.01	<0.01	0.014	<20	1	0.8	100
MT-SCPR6	Hematite+Sericite	0.06	39.84	14.55	36.42	1.84	0.07	0.15	1.71	0.62	0.02	0.08	0.02	92	29	4.6	99.89
MT-CS1	Chlorite	0.07	41.69	16.47	21.79	10.55	0.2	0.01	0.06	1.11	0.13	0.14	0.027	153	26	7.6	99.75
MT-CSS5	Sericite+Chlorite	0.04	53.22	20.75	10	3.36	0.05	0.07	6.35	0.96	0.03	0.05	0.032	65	33	5	99.83
MT-CSPR5	Hematite+Sericite	0.02	53.28	16.78	15.28	3.46	0.73	0.03	4.99	0.75	0.49	0.06	0.024	160	29	3.9	99.83
MT-CS2	Sericite+Chlorite	0.04	54.23	19.32	10.15	4.18	0.05	0.06	5.43	0.91	0.01	0.05	0.027	44	33	5.4	99.82
MT-LBIF8	BIF	0.08	35.72	0.81	61.92	0.35	0.05	0.01	0.01	0.04	0.02	0.02	0.005	20	2	1	99.97
MT-CHBIF10	Chert	0.04	36.66	13.9	34.73	6.8	0.04	0.06	1.04	0.59	<0.01	0.09	<0.002	35	11	5.9	99.8
D-CS4	Debris Flow	0.1	49.61	15.75	15.21	8.58	1.1	0.02	2.03	0.72	0.04	0.12	0.047	233	25	5.9	99.11
S-CS9	Fe-Chlorite	0.07	28.75	19.76	30.28	10.18	0.08	0.04	1.2	0.94	<0.01	0.18	0.024	121	26	8.3	99.75
S-SCS3	Sericite+Chlorite	0.05	59.84	16.23	11.7	3.4	0.05	0.04	4.28	0.7	<0.01	0.06	0.025	55	24	3.5	99.85

	Method	LF200	LF200	LF200	LF200	LF200	LF200	LF200	LF200	LF200	LF200	LF200	LF200	LF200	LF200	LF200
	Analyte	Ba	Be	Co	Cs	Ga	Hf	Nb	Rb	Sn	Sr	Ta	Th	U	V	W
	Unit	PPM	PPM	PPM	PPM	PPM	PPM	PPM	PPM	PPM	PPM	PPM	PPM	PPM	PPM	PPM
	Detection Limit	1	1	0.2	0.1	0.5	0.1	0.1	0.1	1	0.5	0.1	0.2	0.1	8	0.5
Sample	Lithology															
D003	Sericite/Paragonite	159	<1	16.8	5.2	13.1	2.1	3.6	93.2	<1	29.2	0.3	0.9	0.3	90	<0.5
D004	Ore	7	2	8.8	0.1	3.8	0.5	3.3	<0.1	1	5.2	0.2	0.3	<0.1	40	1.8
D004-2	Fe-Chlorite	76	3	33.3	5.6	11.9	2.2	4.1	47.8	<1	31.2	0.2	0.8	0.4	89	0.5
D2001	Ore	10	<1	1.1	<0.1	1.7	<0.1	0.1	0.1	<1	5.3	<0.1	<0.2	<0.1	30	2.7
D2009	Ore	6	<1	3.5	<0.1	<0.5	0.3	0.3	<0.1	<1	4.5	<0.1	<0.2	<0.1	34	2.2
D2010	Hematite+Chlorite	12	2	48.3	0.8	7.4	1.5	3	0.6	<1	12.9	0.2	0.6	0.2	76	<0.5
D2014	Ore	2	<1	1.3	0.2	<0.5	<0.1	0.6	<0.1	<1	3.5	0.1	<0.2	<0.1	34	2
D2015	BIF	3	<1	1.1	<0.1	<0.5	<0.1	0.2	<0.1	<1	2.3	<0.1	<0.2	<0.1	13	1.2
D2016	Ore	10	2	2.2	<0.1	<0.5	<0.1	0.5	<0.1	<1	5.8	0.4	<0.2	<0.1	35	3.2
D2017	Hematite+Chlorite	14	3	65.5	2.9	11.3	1.7	2.9	1.4	<1	46	0.2	0.5	0.4	95	<0.5
D2018	Chlorite	319	2	30.1	3	12.2	1.7	2.7	67.7	<1	8.4	0.2	0.6	0.2	134	<0.5
D2019	BIF	9	<1	8.6	<0.1	1.3	<0.1	0.2	0.7	<1	21.8	<0.1	<0.2	0.4	23	1.5
D2020	BIF	4	<1	2.5	<0.1	<0.5	<0.1	<0.1	<0.1	<1	6.2	<0.1	<0.2	<0.1	10	1.1
D001	Sericite/Paragonite	105	<1	19.1	3.4	11.7	2	4.6	49.7	<1	112.8	0.3	0.7	0.1	105	0.7
D001-2	Hematite+Sericite	86	<1	12.7	5.1	9.4	1.8	4.1	32.8	<1	85.6	0.3	0.7	0.3	161	<0.5
S102	Fe-Chlorite	5	4	54.7	2.1	10.9	10.1	16.2	1.2	3	15.2	1.6	7.5	1.5	29	<0.5
S104	Ore	5	2	2.1	<0.1	<0.5	0.2	0.2	<0.1	1	5.5	<0.1	<0.2	<0.1	42	2.4
S105	Ore	12	2	3.7	0.2	1	<0.1	0.1	0.3	<1	27.7	<0.1	<0.2	0.2	69	3.5
S106	BIF	5	1	2.9	<0.1	0.7	<0.1	<0.1	<0.1	<1	7.1	<0.1	<0.2	0.1	36	3.5
S107	Ore	7	2	1.6	1.6	<0.5	0.1	<0.1	2.5	<1	17.7	<0.1	<0.2	<0.1	52	6.7
S3010	Ore	9	<1	7.7	<0.1	2.6	<0.1	<0.1	<0.1	1	13	<0.1	<0.2	0.1	56	1.9
S3010-2	Fe-Chlorite	266	3	51.1	3	15.9	2.2	3.5	65.6	<1	13.6	0.3	0.7	0.3	131	<0.5
S3011	BIF	7	1	1.5	<0.1	<0.5	0.1	<0.1	0.4	<1	3.3	<0.1	<0.2	<0.1	18	0.8
S3012	Ore	14	<1	2.5	0.2	<0.5	<0.1	0.4	2	1	3.5	0.2	<0.2	<0.1	45	2.7
S3014	Ore	6	2	10.3	<0.1	1.6	0.2	0.3	<0.1	<1	3.9	0.1	<0.2	<0.1	53	0.5
S3018	Ore	7	<1	4.3	<0.1	1.6	0.2	<0.1	<0.1	1	19.3	<0.1	<0.2	0.5	39	1.7
MT2001	Sericite+Chlorite	334	<1	22.2	7.9	13.7	1.7	2.3	220.1	<1	13.9	0.2	0.5	0.1	162	<0.5
MT2003	BIF	1	<1	4.7	<0.1	<0.5	<0.1	0.2	<0.1	<1	2.1	<0.1	<0.2	<0.1	27	<0.5
MT3002	Sericite+Chlorite	530	2	14	10.5	16.8	2	3.1	301.4	<1	11.8	0.2	0.7	0.1	201	<0.5
MT3003	Sericite+Chlorite	389	1	44.7	8.2	14.5	1.9	3.4	192.9	<1	11.6	0.2	0.6	0.1	172	<0.5
MT3004	BIF	6	<1	1.2	<0.1	<0.5	<0.1	<0.1	0.5	<1	1.5	<0.1	<0.2	<0.1	18	2.1
MT3007	Fe-Chlorite	6	3	44.4	1	7.4	6.3	9	0.6	3	11.2	1.1	5.5	0.9	15	1
MT3008	BIF	3	<1	1.7	<0.1	<0.5	0.1	<0.1	0.1	<1	1.5	<0.1	<0.2	<0.1	18	1.6
MT-SCPR6	Hematite+Sericite	139	6	16	6.2	12.3	1.5	2.9	62.7	<1	29.3	0.2	0.6	0.2	170	<0.5
MT-CS1	Chlorite	17	<1	41.1	0.4	16.5	2.1	3.9	2.9	<1	4.1	0.2	0.4	0.1	216	<0.5
MT-CSS5	Sericite+Chlorite	418	1	13.8	7.6	16.6	3.2	5.2	268	<1	13.8	0.4	1	0.1	166	0.6
MT-CSPR5	Hematite+Sericite	496	4	23.7	7.2	14.8	1.8	3.4	241.3	<1	17	0.3	0.6	<0.1	198	<0.5
MT-CS2	Sericite+Chlorite	464	<1	11	7.7	19.7	2.8	4.9	243.4	<1	19.5	0.4	0.8	0.1	174	0.6
MT-LBIF8	BIF	11	<1	6.1	<0.1	0.8	0.3	0.2	0.6	<1	3	<0.1	<0.2	<0.1	17	1.4
MT-CHBIF10	Chert	93	4	8.7	5	11.2	6.6	9.4	37.6	3	27.4	0.8	5.3	1.2	21	1.2
D-CS4	Debris Flow	204	<1	41.4	1.8	12.8	1.6	3.9	59.9	<1	10.9	0.3	0.9	0.2	157	<0.5
S-CS9	Fe-Chlorite	105	4	47.5	4.5	11.3	2.3	4.2	54.4	1	21.3	0.3	0.7	0.3	87	<0.5
S-SCS3	Sericite+Chlorite	468	2	15	5.5	14	2	3.1	181.8	<1	9.8	0.2	0.6	0.1	130	0.6

	Method	LF200	LF200	LF200	LF200	LF200	LF200	LF200	LF200	LF200	LF200	LF200	LF200	LF200	LF200	LF200
	Analyte	Zr	Y	La	Ce	Pr	Nd	Sm	Eu	Gd	Tb	Dy	Ho	Er	Tm	Yb
	Unit	PPM	PPM	PPM	PPM	PPM	PPM	PPM	PPM	PPM	PPM	PPM	PPM	PPM	PPM	PPM
	Detection Limit	0.1	0.1	0.1	0.1	0.02	0.3	0.05	0.02	0.05	0.01	0.05	0.02	0.03	0.01	0.05
Sample	Lithology															
D003	Sericite/Paragonite	83.8	10.3	6.5	14.9	1.85	8.3	1.79	0.5	1.84	0.3	2.04	0.41	1.34	0.2	1.34
D004	Ore	17.9	81.7	6.6	11.3	1.48	6.9	2.22	1.71	4.4	0.93	7.19	1.95	6.31	0.89	5.11
D004-2	Fe-Chlorite	83	39.2	7.5	13.3	1.48	5.8	1.4	1.11	2.46	0.48	3.65	0.97	3.08	0.44	2.82
D2001	Ore	1.5	8	2.8	4.7	0.83	4.1	1.15	1.15	1.54	0.19	1.11	0.18	0.55	0.07	0.41
D2009	Ore	9	7	3.2	3.1	0.4	2	0.46	0.41	0.65	0.1	0.64	0.13	0.44	0.06	0.4
D2010	Hematite+Chlorite	57.9	19.5	9.2	19.7	2.34	9.8	2.19	1.36	2.41	0.42	2.63	0.58	1.81	0.27	1.68
D2014	Ore	3.3	10.6	2.5	4.2	0.48	2.2	0.45	0.47	0.76	0.16	1.1	0.29	0.89	0.13	0.79
D2015	BIF	3.3	9.4	5	7.7	0.77	3	0.48	0.55	0.75	0.13	0.88	0.21	0.87	0.11	0.62
D2016	Ore	3	12.5	3.5	6.8	0.83	4.1	0.94	0.9	1.49	0.24	1.39	0.34	0.84	0.13	0.83
D2017	Hematite+Chlorite	67.2	30.6	15.7	30.4	3.82	16.4	4.43	3.4	5.1	0.86	4.93	1.01	2.9	0.42	2.69
D2018	Chlorite	61.1	11.6	6.9	9.1	0.95	3.2	0.74	0.4	1.36	0.27	1.88	0.39	1.11	0.17	1.09
D2019	BIF	2.8	12.1	8.1	11.8	1.29	5.9	1.37	1.1	1.88	0.22	1.26	0.29	0.74	0.09	0.59
D2020	BIF	2.8	3.7	2.4	3.4	0.41	1.6	0.42	0.42	0.54	0.08	0.47	0.13	0.34	0.04	0.3
D001	Sericite/Paragonite	82.8	10.6	7.3	16.8	1.83	7.3	1.46	0.47	1.53	0.28	1.79	0.4	1.17	0.16	1.12
D001-2	Hematite+Sericite	73.2	9.5	5.5	12	1.52	6.4	1.99	1.02	2.48	0.42	2.15	0.43	1.16	0.16	1.06
S102	Fe-Chlorite	369.9	40.8	24.2	51	5.75	23.1	4.79	2.3	4.9	0.82	5.52	1.22	3.74	0.59	4.04
S104	Ore	4.5	9.5	5	6.4	0.71	3.1	0.68	0.65	0.86	0.16	0.98	0.24	0.74	0.1	0.66
S105	Ore	3.5	53.8	10.2	32.1	4.86	28.4	7.91	6.52	10.42	1.24	6.58	1.37	3.27	0.36	1.99
S106	BIF	2.7	7	2.9	6	0.8	4.6	1.01	0.8	1.25	0.16	0.84	0.17	0.48	0.06	0.4
S107	Ore	3.7	14.3	6	7	0.79	3.1	0.67	0.64	1.05	0.19	1.28	0.37	0.98	0.15	0.9
S3010	Ore	4	16.2	5	7.8	0.99	5.7	1.54	1.36	2	0.27	1.63	0.41	1.1	0.13	0.82
S3010-2	Fe-Chlorite	79.8	49.7	14.8	30.9	3.63	15	2.92	2.03	3.71	0.65	4.34	1.17	3.46	0.49	3.07
S3011	BIF	3.4	5.5	2.5	4.2	0.41	1.9	0.4	0.4	0.51	0.08	0.5	0.13	0.37	0.06	0.34
S3012	Ore	3.4	9.1	2.2	4	0.43	1.5	0.51	0.47	0.78	0.14	0.77	0.2	0.61	0.08	0.64
S3014	Ore	7.3	12.6	3.4	6.3	0.82	4.3	1.11	0.81	1.42	0.22	1.4	0.32	1.11	0.15	0.91
S3018	Ore	8.5	17.6	5.8	11.7	1.75	7.9	2.36	2.17	3.03	0.43	2.46	0.51	1.35	0.2	1.2
MT2001	Sericite+Chlorite	59.3	7	5.2	11.6	1.53	6.5	1.58	0.7	1.71	0.25	1.56	0.29	0.82	0.13	0.84
MT2003	BIF	2.4	4.6	5.1	9.1	0.91	3.2	0.73	0.44	0.66	0.09	0.57	0.13	0.36	0.05	0.29
MT3002	Sericite+Chlorite	74	7.6	5.7	12.6	1.57	6.7	1.06	0.46	1.15	0.23	1.62	0.31	0.94	0.17	1.09
MT3003	Sericite+Chlorite	72.2	7.2	5.2	13.1	1.71	7.1	1.6	0.54	1.57	0.26	1.55	0.28	0.9	0.14	0.94
MT3004	BIF	4.3	8.5	4.6	7.9	0.93	4	0.69	0.46	0.9	0.14	0.96	0.22	0.63	0.1	0.65
MT3007	Fe-Chlorite	224.9	18.7	11.3	23.7	2.72	10.8	2.15	0.87	2.44	0.43	2.76	0.57	1.88	0.31	2.15
MT3008	BIF	7.2	7.7	5.2	8.2	0.94	3.4	0.61	0.56	0.74	0.13	0.83	0.19	0.61	0.09	0.57
MT-SCPR6	Hematite+Sericite	62.3	12.2	8	16.6	2.14	9.3	1.92	0.8	2.06	0.36	2.19	0.46	1.33	0.18	1.26
MT-CS1	Chlorite	81.4	8.7	2.4	6.2	0.82	3.8	1.25	0.36	1.57	0.27	1.68	0.33	0.99	0.18	1.18
MT-CSS5	Sericite+Chlorite	119.5	16.9	11.3	23.4	3.05	13.4	2.37	0.79	2.69	0.48	2.93	0.65	1.93	0.29	1.89
MT-CSPR5	Hematite+Sericite	74.7	12.6	7.1	17.5	2.45	12.2	3.18	1.38	3.49	0.51	3.11	0.53	1.42	0.2	1.3
MT-CS2	Sericite+Chlorite	110.4	12.3	19.9	42.9	5.06	20.7	2.7	0.77	2.08	0.32	1.96	0.42	1.25	0.2	1.44
MT-LBIF8	BIF	13	14.1	10	14.9	1.67	5.9	1.2	0.86	1.38	0.22	1.41	0.37	1.11	0.15	1.1
CHBIF10	Chert	246.7	17.6	14.7	28.9	3.47	12.8	2.84	1	2.96	0.49	2.92	0.64	2.01	0.28	2.07
D-CS4	Debris Flow	72	14.4	29.7	67.6	8.23	32.1	4.71	1.17	4.02	0.52	2.96	0.57	1.6	0.21	1.41
S-CS9	Fe-Chlorite	91.1	25.3	4.1	7	0.81	3.3	0.99	0.81	1.83	0.36	2.78	0.7	2.25	0.34	2.16
S-SCS3	Sericite+Chlorite	74	12.3	8.1	14.9	1.69	6.9	1.39	0.7	1.66	0.3	2.01	0.45	1.34	0.18	1.44

	Method	LF200	TC000	TC000	AQ200	AQ200	AQ200	AQ200	AQ200	AQ200	AQ200	AQ200	AQ200	AQ200	AQ200	AQ200	AQ200	AQ200
	Analyte	Lu	TOT/C	TOT/S	Mo	Cu	Pb	Zn	Ni	As	Cd	Sb	Bi	Ag	Au	Hg	Tl	Se
	Unit	PPM	%	%	PPM	PPM	PPM	PPM	PPM	PPM	PPM	PPM	PPM	PPM	PPB	PPM	PPM	PPM
	Detection Limit	0.01	0.02	0.02	0.1	0.1	0.1	1	0.1	0.5	0.1	0.1	0.1	0.1	0.5	0.01	0.1	0.5
Sample	Lithology																	
D003	Sericite/Paragonite	0.23	0.05	<0.02	0.3	7.5	0.7	29	89.1	<0.5	<0.1	<0.1	<0.1	<0.1	<0.5	<0.01	<0.1	<0.5
D004	Ore	0.78	0.04	<0.02	0.5	2.3	2.2	17	48.4	5.5	<0.1	0.6	<0.1	<0.1	1.4	<0.01	<0.1	<0.5
D004-2	Fe-Chlorite	0.41	<0.02	<0.02	0.2	0.3	0.6	144	75.3	0.6	<0.1	<0.1	<0.1	<0.1	1.3	<0.01	<0.1	<0.5
D2001	Ore	0.05	0.02	<0.02	2.1	1.9	0.9	3	18.6	1.6	<0.1	0.3	<0.1	<0.1	1.4	<0.01	<0.1	<0.5
D2009	Ore	0.06	<0.02	<0.02	1.1	6.1	1.2	6	21.4	2	<0.1	0.5	<0.1	<0.1	2.5	<0.01	<0.1	<0.5
D2010	Hematite+Chlorite	0.28	<0.02	<0.02	0.6	0.8	1.1	126	79	0.9	<0.1	0.1	<0.1	<0.1	<0.5	<0.01	<0.1	<0.5
D2014	Ore	0.11	<0.02	<0.02	0.6	2.7	0.4	4	4.7	1.1	<0.1	0.5	<0.1	<0.1	<0.5	<0.01	<0.1	<0.5
D2015	BIF	0.11	<0.02	<0.02	2	3.1	0.5	4	4.1	1.3	<0.1	0.3	<0.1	<0.1	0.7	<0.01	<0.1	<0.5
D2016	Ore	0.11	0.04	<0.02	1.5	166.3	0.8	5	14.4	2.1	<0.1	0.6	<0.1	<0.1	1.9	<0.01	<0.1	<0.5
D2017	Hematite+Chlorite	0.41	0.02	<0.02	0.1	3.3	7.1	154	146.4	2.5	<0.1	0.4	<0.1	<0.1	2.1	<0.01	<0.1	<0.5
D2018	Chlorite	0.17	<0.02	<0.02	0.3	2.3	0.3	108	40.3	<0.5	<0.1	<0.1	<0.1	<0.1	1.5	<0.01	<0.1	<0.5
D2019	BIF	0.09	<0.02	<0.02	0.9	13.9	0.7	14	45.7	1.5	<0.1	0.3	<0.1	<0.1	<0.5	<0.01	<0.1	<0.5
D2020	BIF	0.04	0.03	<0.02	2.1	8.6	0.7	13	7.1	2.8	<0.1	0.5	<0.1	<0.1	1.8	<0.01	<0.1	<0.5
D001	Sericite/Paragonite	0.17	<0.02	<0.02	1.3	6.9	0.1	24	57.5	<0.5	<0.1	<0.1	<0.1	<0.1	<0.5	<0.01	<0.1	<0.5
D001-2	Hematite+Sericite	0.17	0.02	<0.02	0.9	49.3	2.3	20	53.5	13.8	<0.1	0.1	<0.1	<0.1	0.5	<0.01	<0.1	<0.5
S102	Fe-Chlorite	0.63	0.04	<0.02	0.1	1.2	2.5	156	158.7	<0.5	<0.1	<0.1	<0.1	<0.1	<0.5	<0.01	<0.1	<0.5
S104	Ore	0.1	0.02	<0.02	1.2	8.5	0.7	2	10	2.6	<0.1	0.4	<0.1	0.1	7.3	<0.01	<0.1	<0.5
S105	Ore	0.24	<0.02	<0.02	1	11.5	1.2	6	24.4	6.9	<0.1	0.5	<0.1	<0.1	0.8	0.01	<0.1	<0.5
S106	BIF	0.05	<0.02	<0.02	1.4	10	0.5	9	26.9	2.7	<0.1	0.4	<0.1	<0.1	<0.5	<0.01	<0.1	<0.5
S107	Ore	0.12	<0.02	<0.02	1.4	13.9	0.7	3	10.4	2.6	<0.1	0.7	<0.1	<0.1	1.7	<0.01	<0.1	<0.5
S3010	Ore	0.13	<0.02	<0.02	1.1	1.8	1.2	16	37.1	4.4	<0.1	0.6	<0.1	<0.1	0.7	<0.01	<0.1	<0.5
S3010-2	Fe-Chlorite	0.46	<0.02	<0.02	1.2	2.4	0.3	159	89.6	<0.5	<0.1	<0.1	<0.1	<0.1	<0.5	<0.01	<0.1	<0.5
S3011	BIF	0.06	<0.02	<0.02	1.9	3.8	0.6	8	3.6	2	<0.1	0.4	<0.1	<0.1	1.1	<0.01	<0.1	<0.5
S3012	Ore	0.08	<0.02	<0.02	1.1	2.5	0.9	6	11.6	1.4	<0.1	0.4	<0.1	<0.1	0.5	<0.01	<0.1	<0.5
S3014	Ore	0.13	<0.02	<0.02	1.5	2.3	0.8	22	29.8	2.3	<0.1	0.2	<0.1	<0.1	1	<0.01	<0.1	<0.5
S3018	Ore	0.2	<0.02	<0.02	1	7.8	0.9	5	41.5	4.7	<0.1	0.7	<0.1	0.4	98.9	<0.01	<0.1	<0.5
MT2001	Sericite+Chlorite	0.14	0.16	<0.02	0.6	3.3	0.9	51	358.2	0.8	<0.1	0.1	<0.1	<0.1	1.9	<0.01	<0.1	<0.5
MT2003	BIF	0.05	0.06	<0.02	3	8.2	0.8	8	13.5	1.8	<0.1	0.3	<0.1	<0.1	2.2	<0.01	<0.1	<0.5
MT3002	Sericite+Chlorite	0.17	<0.02	<0.02	0.2	1.1	0.9	38	31.1	<0.5	<0.1	<0.1	<0.1	<0.1	<0.5	<0.01	<0.1	<0.5
MT3003	Sericite+Chlorite	0.13	0.08	<0.02	0.5	5.3	0.4	77	194.3	<0.5	<0.1	<0.1	<0.1	<0.1	<0.5	<0.01	<0.1	<0.5
MT3004	BIF	0.1	<0.02	<0.02	1.3	2.1	0.5	7	3.2	1.5	<0.1	0.2	<0.1	<0.1	<0.5	<0.01	<0.1	<0.5
MT3007	Fe-Chlorite	0.35	0.03	<0.02	0.3	0.5	0.9	143	43	<0.5	<0.1	<0.1	<0.1	<0.1	7.3	<0.01	<0.1	<0.5
MT3008	BIF	0.09	<0.02	<0.02	3.1	2.3	0.5	10	5.6	1.4	<0.1	0.1	<0.1	<0.1	1.4	<0.01	<0.1	<0.5
MT-SCPR6	Hematite+Sericite	0.2	<0.02	<0.02	0.4	11.8	10.5	38	91.1	3.7	<0.1	0.5	<0.1	<0.1	0.6	<0.01	<0.1	<0.5
MT-CS1	Chlorite	0.21	<0.02	<0.02	0.1	3.2	1.5	132	137.3	0.6	<0.1	<0.1	<0.1	<0.1	<0.5	<0.01	<0.1	<0.5
MT-CSS5	Sericite+Chlorite	0.32	<0.02	<0.02	<0.1	1.2	0.8	32	46.1	<0.5	<0.1	<0.1	<0.1	<0.1	0.6	<0.01	<0.1	<0.5
MT-CSPR5	Hematite+Sericite	0.21	0.04	<0.02	0.1	3.6	6	54	153	0.5	<0.1	0.1	<0.1	<0.1	0.7	<0.01	<0.1	<0.5
MT-CS2	Sericite+Chlorite	0.23	<0.02	<0.02	<0.1	2.1	2	42	31.3	<0.5	<0.1	<0.1	<0.1	<0.1	<0.5	<0.01	<0.1	<0.5
MT-LBIF8	BIF	0.16	<0.02	<0.02	<0.1	2.3	1.6	12	15.1	1.1	<0.1	0.2	<0.1	<0.1	<0.5	<0.01	<0.1	<0.5
CHBIF10	Chert	0.34	0.02	<0.02	<0.1	0.7	2	94	29.8	<0.5	<0.1	<0.1	<0.1	<0.1	<0.5	<0.01	<0.1	<0.5
D-CS4	Debris Flow	0.21	0.25	0.63	0.2	6224.8	1	98	220.7	<0.5	<0.1	<0.1	<0.1	1.8	1.3	0.09	<0.1	3.5
S-CS9	Fe-Chlorite	0.33	<0.02	<0.02	<0.1	24.2	0.8	152	116.6	<0.5	<0.1	<0.1	<0.1	0.1	<0.5	<0.01	<0.1	<0.5
S-SCS3	Sericite+Chlorite	0.19	<0.02	<0.02	<0.1	21.5	2.7	51	48.9	<0.5	<0.1	<0.1	<0.1	<0.1	<0.5	<0.01	<0.1	<0.5

APPENDIX C

RESULTS OF ISOCON ANALYSES

	Sericite +/- Paragonite (D001 & D003)	Secondary Sericite (MT-2001, 3002, 3003, CSS5, S-SCS3, CS2)	slope	scale	Scaled Data (D001 & D003)	Scaled Data (MT-2001)		% Change Al2O3, TiO2, Hf, Zr Isocon	% Change Constant Mass	% Change Constant Volume
SiO2%	65.6	54.4	0.83	0.4	26.24	21.76	Constant Al, Ti Hf, Zr	-22.6	-17.07	-12.71
Al2O3%	17.22	18.71	1.09	1	17.22	18.71	1.07	1.4	8.64	14.36
Fe2O3%	8.4	11.47	1.37	1	8.4	11.47	Constant Mass Isocon	27.54	36.65	43.84
MgO%	0.98	4.16	4.26	1	0.98	4.16	1	298.07	326.5	348.94
CaO%	0.07	0.1	1.56	40	2.6	4.07	Constant Volume Isocon	45.98	56.41	64.64
Na2O%	1.18	0.05	0.04	10	11.75	0.52	0.95	-95.9	-95.6	-95.37
K2O%	2.35	5.32	2.27	4	9.38	21.27		111.68	126.79	138.73
TiO2%	0.74	0.8	1.07	10	7.4	7.95		0.27	7.43	13.09
P2O5%	0.02	0.05	2.95	40	0.7	2.07		175.56	195.24	210.78
MnO%	0.04	0.05	1.43	1	0.04	0.05		33.34	42.86	50.38
Cr2O3%	0.02	0.03	1.45	1	0.02	0.03		35.7	45.39	53.04
Sc_PPM	22.5	30	1.33	1	22.5	30		24.45	33.33	40.35
LOI%	3.35	4.68	1.4	1	3.35	4.68		30.48	39.8	47.16
Ba	132	433.83	3.29	0.1	13.2	43.38		206.76	228.66	245.96
Be	0.5	1.17	2.33	1	0.5	1.17		117.78	133.33	145.61
Co	17.95	20.12	1.12	1	17.95	20.12		4.6	12.07	17.97
Cs	4.3	7.9	1.84	2	8.6	15.8		71.48	83.72	93.39
Ga	12.4	15.88	1.28	1	12.4	15.88		19.55	28.09	34.83
Hf	2.05	2.27	1.11	2	4.1	4.53		3.2	10.57	16.39
Nb	4.1	3.67	0.89	6	24.6	22		-16.53	-10.57	-5.86
Rb	71.45	234.6	3.28	0.1	7.15	23.46		206.46	228.34	245.62
Sn	0.5	0.5	1	1	0.5	0.5		-6.67	0	5.26
Sr	71	13.4	0.19	1	71	13.4		-82.38	-81.13	-80.13
Ta	0.3	0.27	0.89	1	0.3	0.27		-17.04	-11.11	-6.43
Th	0.8	0.7	0.88	1	0.8	0.7		-18.33	-12.5	-7.89
U	0.2	0.1	0.5	1	0.2	0.1		-53.33	-50	-47.37
V	97.5	167.5	1.72	0.1	9.75	16.75		60.34	71.79	80.84
W	0.48	0.43	0.89	1	0.48	0.43		-16.49	-10.53	-5.82
Zr	83.3	84.9	1.02	0.4	33.32	33.96		-4.87	1.92	7.29
Y	10.45	10.55	1.01	2	20.9	21.1		-5.77	0.96	6.27
La	6.9	9.23	1.34	1	6.9	9.23		24.9	33.82	40.86
Ce	15.85	19.75	1.25	1	15.85	19.75		16.3	24.61	31.16
Pr	1.84	2.44	1.32	2	3.68	4.87		23.52	32.34	39.3
Nd	7.8	10.22	1.31	2	15.6	20.43		22.25	30.98	37.88
Sm	1.63	1.78	1.1	6	9.75	10.7		2.43	9.74	15.52
Eu	0.49	0.66	1.36	12	5.82	7.92		27.01	36.08	43.24
Gd	1.69	1.81	1.07	6	10.11	10.86		0.26	7.42	13.07
Tb	0.29	0.31	1.06	10	2.9	3.07		-1.3	5.75	11.31
Dy	1.92	1.94	1.01	6	11.49	11.63		-5.53	1.22	6.55
Ho	0.41	0.4	0.99	12	4.86	4.8		-7.82	-1.23	3.96
Er	1.26	1.2	0.95	6	7.53	7.18		-11	-4.65	0.37
Tm	0.18	0.19	1.03	10	1.8	1.85		-4.07	2.78	8.19
Yb	1.23	1.27	1.04	2	2.46	2.55		-3.38	3.52	8.97
Lu	0.2	0.2	0.98	16	3.2	3.15		-8.22	-1.67	3.51
Mo	0.8	0.24	0.3	1	0.8	0.24		-71.81	-69.79	-68.2
Cu	7.2	5.75	0.8	4	28.8	23		-25.46	-20.14	-15.94
Pb	0.4	1.28	3.21	1	0.4	1.28		199.45	220.83	237.72
Zn	26.5	48.5	1.83	0.2	5.3	9.7		70.82	83.02	92.65
Ni	73.3	118.32	1.61	0.06	4.4	7.1		50.66	61.41	69.91
As	0.25	0.34	1.37	1	0.25	0.34		27.56	36.67	43.86
Au	0.25	0.58	2.33	1	0.25	0.58		117.78	133.33	145.61
Se	0.25	0.25	1	1	0.25	0.25		-6.67	0	5.26

	Mg-Chlorite (MT-CS1)	Secondary Sericite (MT-2001, 3002, 3003, CSS5, S-SCS3, CS2)	slope	scale	Scaled Data (MT-CS1)	Scaled Data (MT-2001)		% Change Al2O3, Hf, Zr Isocon	% Change Constant Mass	% Change Constant Volume
SiO2%	41.69	54.4	1.3	0.6	25.01	32.64	Al2O3, Hf, Zr Isocon	20.14	30.48	37.35
Al2O3%	16.47	18.71	1.14	1	16.47	18.71	1.0861	4.59	13.59	19.57
Fe2O3%	21.79	11.47	0.53	1	21.79	11.47	Constant Mass Isocon	-51.53	-47.35	-44.58
MgO%	10.55	4.16	0.39	1	10.55	4.16	1	-63.71	-60.58	-58.51
CaO%	0.2	0.1	0.51	40	8	4.07	Constant Volume	-53.2	-49.17	-46.49
Na2O%	0.01	0.05	5.17	1	0.01	0.05	0.95	375.71	416.67	443.86
K2O%	0.06	5.32	88.6	4	0.24	21.27		8061.29	8763.89	9230.41
TiO2%	1.11	0.8	0.72	10	11.1	7.95		-34.06	-28.38	-24.61
P2O5%	0.13	0.05	0.4	40	5.2	2.07		-63.41	-60.26	-58.16
MnO%	0.14	0.05	0.36	1	0.14	0.05		-67.12	-64.29	-62.41
Cr2O3%	0.03	0.03	1.27	1	0.03	0.03		16.51	26.54	33.2
Sc_PPM	26	30	1.15	1	26	30		6.24	15.38	21.46
LOI%	7.6	4.68	0.62	1	7.6	4.68		-43.26	-38.38	-35.13
Ba	17	433.83	25.5	0.1	1.7	43.38		2249.68	2451.96	2586.27
Be	0.5	1.17	2.33	1	0.5	1.17		114.84	133.33	145.61
Co	41.1	20.12	0.49	1	41.1	20.12		-54.93	-51.05	-48.48
Cs	0.4	7.9	19.8	2	0.8	15.8		1718.45	1875	1978.95
Ga	16.5	15.88	0.96	1	16.5	15.88		-11.37	-3.74	1.33
Hf	2.1	2.27	1.08	6	12.6	13.6		-0.62	7.94	13.62
Nb	3.9	3.67	0.94	6	23.4	22		-13.44	-5.98	-1.03
Rb	2.9	234.6	80.9	0.1	0.29	23.46		7348.43	7989.66	8415.43
Sn	0.5	0.5	1	1	0.5	0.5		-7.93	0	5.26
Sr	4.1	13.4	3.27	1	4.1	13.4		200.92	226.83	244.03
Ta	0.2	0.27	1.33	1	0.2	0.27		22.76	33.33	40.35
Th	0.4	0.7	1.75	1	0.4	0.7		61.13	75	84.21
U	0.1	0.1	1	1	0.1	0.1		-7.93	0	5.26
V	216	167.5	0.78	0.1	21.6	16.75		-28.6	-22.45	-18.37
W	0.25	0.43	1.7	1	0.25	0.43		56.52	70	78.95
Zr	81.4	84.9	1.04	0.4	32.56	33.96		-3.97	4.3	9.79
Y	8.7	10.55	1.21	1	8.7	10.55		11.65	21.26	27.65
La	2.4	9.23	3.85	2	4.8	18.47		254.23	284.72	304.97
Ce	6.2	19.75	3.19	2	12.4	39.5		193.3	218.55	235.31
Pr	0.82	2.44	2.97	2	1.64	4.87		173.41	196.95	212.58
Nd	3.8	10.22	2.69	2	7.6	20.43		147.55	168.86	183.01
Sm	1.25	1.78	1.43	6	7.5	10.7		31.36	42.67	50.18
Eu	0.36	0.66	1.83	2	0.72	1.32		68.8	83.33	92.98
Gd	1.57	1.81	1.15	6	9.42	10.86		6.15	15.29	21.35
Tb	0.27	0.31	1.14	10	2.7	3.07		4.58	13.58	19.56
Dy	1.68	1.94	1.15	4	6.72	7.75		6.23	15.38	21.45
Ho	0.33	0.4	1.21	12	3.96	4.8		11.6	21.21	27.59
Er	0.99	1.2	1.21	8	7.92	9.57		11.29	20.88	27.24
Tm	0.18	0.19	1.03	10	1.8	1.85		-5.37	2.78	8.19
Yb	1.18	1.27	1.08	2	2.36	2.55		-0.64	7.91	13.59
Lu	0.21	0.2	0.94	16	3.36	3.15		-13.77	-6.35	-1.42
Mo	0.1	0.24	2.42	1	0.1	0.24		122.51	141.67	154.39
Cu	3.2	5.75	1.8	4	12.8	23		65.44	79.69	89.14
Pb	1.5	1.28	0.86	1	1.5	1.28		-21.23	-14.44	-9.94
Zn	132	48.5	0.37	0.2	26.4	9.7		-66.17	-63.26	-61.32
Ni	137.3	118.32	0.86	0.1	13.73	11.83		-20.66	-13.83	-9.29
As	0.6	0.34	0.57	1	0.6	0.34		-47.57	-43.06	-40.06
Au	0.25	0.58	2.33	1	0.25	0.58		114.84	133.33	145.61
Se	0.25	0.25	1	1	0.25	0.25		-7.93	0	5.26

	Sericite (MT-2001, 3002, 3003, CS2, CSS5, S-SCS3)	Fe-Chlorite (SCS-9, S3010-2, & D004-2)	slope	scale	Scaled Data (MT-CSS5 & MT-CS2)	Scaled Data (SCS-9, S3010-2, & D004-2)		% Change Al, Ti Isocon	% Change Constant Hf, Zr	% Change Constant Mass	% Change Constant Volume
SiO2%	54.4	29.75	0.55	0.5	27.2	14.88	Constant Al2O3, TiO2	-51.24	-44.81	-45.3	-42.39
Al2O3%	18.71	20.64	1.1	1	18.71	20.64	1.12	-1.66	11.32	10.33	16.2
Fe2O3%	11.47	28.36	2.47	1	11.47	28.36	Constant Mass Isocon	120.39	149.47	147.25	160.41
MgO%	4.16	10.06	2.42	1.6	6.65	16.1	1	115.72	144.18	142	154.89
CaO%	0.1	0.08	0.79	1	0.1	0.08	Constant Volume Isocon	-29.86	-20.6	-21.31	-17.12
Na2O%	0.05	0.05	0.9	1	0.05	0.05	0.95	-19.49	-8.86	-9.68	-4.87
K2O%	5.32	1.41	0.27	4	21.27	5.65	Constant Hf, Zr	-76.31	-73.19	-73.43	-72.01
TiO2%	0.8	0.91	1.14	1	0.8	0.91	0.99	1.66	15.07	14.05	20.12
P2O5%	0.05	0.01	0.1	1	0.05	0.01		-91.37	-90.24	-90.32	-89.81
MnO%	0.05	0.19	3.8	1	0.05	0.19		238.72	283.42	280	300.23
Cr2O3%	0.03	0.02	0.72	1	0.03	0.02		-35.65	-27.15	-27.8	-23.96
Sc_PPM	30	28	0.93	1	30	28		-16.8	-5.83	-6.67	-1.7
LOI%	4.68	8.27	1.77	1	4.68	8.27		57.34	78.1	76.51	85.91
Ba	433.83	149	0.34	1	433.83	149		-69.39	-65.35	-65.66	-63.83
Be	1.17	3.33	2.86	1	1.17	3.33		154.68	188.29	185.71	200.92
Co	20.12	43.97	2.19	1	20.12	43.97		94.82	120.53	118.56	130.19
Cs	7.9	4.37	0.55	1	7.9	4.37		-50.73	-44.23	-44.73	-41.78
Ga	15.88	13.03	0.82	1	15.88	13.03		-26.86	-17.2	-17.94	-13.58
Hf	2.27	2.23	0.99	6	13.6	13.4		-12.17	-0.58	-1.47	3.77
Nb	3.67	3.93	1.07	4	14.67	15.73		-4.38	8.24	7.27	12.98
Rb	234.6	55.93	0.24	1	234.6	55.93		-78.75	-75.94	-76.16	-74.89
Sn	0.5	0.67	1.33	1	0.5	0.67		18.85	34.53	33.33	40.43
Sr	13.4	22.03	1.64	1	13.4	22.03		46.57	65.91	64.43	73.18
Ta	0.27	0.27	1	1	0.27	0.27		-10.86	0.9	0	5.32
Th	0.7	0.73	1.05	1	0.7	0.73		-6.62	5.71	4.76	10.34
U	0.1	0.33	3.33	1	0.1	0.33		197.13	236.33	233.33	251.08
V	167.5	102.33	0.61	1	167.5	102.33		-45.54	-38.36	-38.91	-35.65
W	0.43	0.33	0.78	1	0.43	0.33		-30.09	-20.86	-21.57	-17.39
Zr	84.9	84.63	1	0.1	8.49	8.46		-11.14	0.58	-0.31	4.99
Y	10.55	38.07	3.61	0.5	5.28	19.03		221.63	264.07	260.82	280.03
La	9.23	8.8	0.95	1	9.23	8.8		-15.05	-3.84	-4.69	0.38
Ce	19.75	17.07	0.86	1	19.75	17.07		-22.97	-12.81	-13.59	-8.99
Pr	2.44	1.97	0.81	1	2.44	1.97		-27.76	-18.23	-18.96	-14.65
Nd	10.22	8.03	0.79	0.5	5.11	4.02		-29.91	-20.66	-21.37	-17.18
Sm	1.78	1.77	0.99	1	1.78	1.77		-11.53	0.15	-0.75	4.54
Eu	0.66	1.32	1.99	10	6.6	13.17		77.83	101.29	99.49	110.11
Gd	1.81	2.67	1.47	6	10.86	16		31.33	48.66	47.33	55.17
Tb	0.31	0.5	1.62	20	6.13	9.93		44.36	63.41	61.96	70.58
Dy	1.94	3.59	1.85	1	1.94	3.59		65.09	86.88	85.21	95.07
Ho	0.4	0.95	2.37	2	0.8	1.89		110.96	138.8	136.67	149.26
Er	1.2	2.93	2.45	2	2.39	5.86		118.25	147.05	144.85	157.88
Tm	0.19	0.42	2.29	20	3.7	8.47		103.97	130.89	128.83	141.01
Yb	1.27	2.68	2.11	8	10.19	21.47		87.84	112.63	110.73	121.95
Lu	0.2	0.4	2.03	16	3.15	6.4		81.3	105.22	103.39	114.22
Mo	0.24	0.48	2	1	0.24	0.48		78.28	101.8	100	110.65
Cu	5.75	8.97	1.56	1	5.75	8.97		39	57.35	55.94	64.24
Pb	1.28	0.57	0.44	1	1.28	0.57		-60.64	-55.45	-55.84	-53.49
Zn	48.5	151.67	3.13	1	48.5	151.67		178.75	215.53	212.71	229.36
Ni	118.32	93.83	0.79	1	118.32	93.83		-29.31	-19.98	-20.69	-16.47
As	0.34	0.37	1.07	1	0.34	0.37		-4.34	8.28	7.32	13.03
Au	0.58	0.6	1.03	1	0.58	0.6		-8.32	3.78	2.86	8.33
Se	0.25	0.25	1	1	0.25	0.25		-10.86	0.9	0	5.32

	Primary Sericite (D003)	Hematitte Alt. (MT-SCPR6)	slope	scale		% Change Al2O3, TiO2, Zr Isocon	% Change Constant Mass
SiO2%	60.26	39.84	0.66	0.6	Al2O3, TiO2, Zr Isocon	-10.72	-33.89
Al2O3%	19.21	14.55	**0.76**	2	0.74	2.28	-24.26
Fe2O3%	9.91	36.42	3.68	0.6	Constant Mass Isocon	396.27	267.51
MgO%	1.5	1.84	1.23	10	1	65.65	22.67
CaO%	0.06	0.07	1.17	1		57.54	16.67
Na2O%	1.17	0.15	0.13	10		-82.69	-87.18
K2O%	2.91	1.71	0.59	6		-20.65	-41.24
TiO2%	0.83	0.62	0.75	12		0.87	-25.3
P2O5%	0.005	0.02	4	1		440.15	300
MnO%	0.05	0.08	1.6	1		116.06	60
Cr2O3%	0.02	0.02	1	1		35.04	0
Sc_PPM	28	29	1.04	0.8		39.86	3.57
LOI%	4	4.6	1.15	1		55.29	15
Ba	159	139	0.87	0.2		18.05	-12.58
Be	0.5	6	12	1		1520.46	1100
Co	16.8	16	0.95	1		28.61	-4.76
Cs	5.2	6.2	1.19	4		61.01	19.23
Ga	13.1	12.3	0.94	1		26.79	-6.11
Hf	2.1	1.5	0.71	6		-3.54	-28.57
Nb	3.6	2.9	0.81	4		8.78	-19.44
Rb	93.2	62.7	0.67	0.4		-9.15	-32.73
Sn	0.5	0.5	1	1		35.04	0
Sr	29.2	29.3	1	0.8		35.5	0.34
Ta	0.3	0.2	0.67	1		-9.97	-33.33
Th	0.9	0.6	0.67	1		-9.97	-33.33
U	0.3	0.2	0.67	1		-9.97	-33.33
V	90	170	1.89	0.2		155.07	88.89
W	0.25	0.25	1	1		35.04	0
Zr	83.8	62.3	0.74	0.6		0.39	-25.66
Y	10.3	12.2	1.18	1		59.95	18.45
La	6.5	8	1.23	2		66.2	23.08
Ce	14.9	16.6	1.11	1		50.45	11.41
Pr	1.85	2.14	1.16	10		56.21	15.68
Nd	8.3	9.3	1.12	2		51.31	12.05
Sm	1.79	1.92	1.07	10		44.85	7.26
Eu	0.5	0.8	1.6	20		116.06	60
Gd	1.84	2.06	1.12	10		51.18	11.96
Tb	0.3	0.36	1.2	20		62.05	20
Dy	2.04	2.19	1.07	10		44.97	7.35
Ho	0.41	0.46	1.12	20		51.51	12.2
Er	1.34	1.33	0.99	10		34.03	-0.75
Tm	0.2	0.18	0.9	20		21.53	-10
Yb	1.34	1.26	0.94	10		26.98	-5.97
Lu	0.23	0.2	0.87	20		17.42	-13.04
Mo	0.3	0.4	1.33	10		80.05	33.33
Cu	7.5	11.8	1.57	1		112.46	57.33
Pb	0.7	10.5	15	10		1925.57	1400
Zn	29	38	1.31	0.8		76.95	31.03
Ni	89.1	91.1	1.02	0.4		38.07	2.24
As	0.25	3.7	14.8	1		1898.56	1380
Au	0.25	0.6	2.4	1		224.09	140
Se	0.25	0.25	1	1		35.04	0

	Jasper/Hematite BIF (D2009 & S106)	Ore Breccia (D2001 & D2014)	slope	scale	Scaled Data (D2009 & S106)	Scaled Data (D2001 & D2014)		% Change V-HREE Isocon	% Change Constant Mass	% Change Constant Volume
SiO2%	28.65	0.58	0.02	1	28.65	0.58	V-HREE Isocon	-98.16	-97.98	-96.96
Al2O3%	0.91	0.23	0.25	40	36.4	9.2	1.1	-77.07	-74.73	-62.09
Fe2O3%	68.6	98.37	1.43	0.4	27.44	39.35	Constant Mass Isocon	30.07	43.4	115.09
MgO%	0.35	0.02	0.04	40	13.8	0.6	1	-96.06	-95.65	-93.48
CaO%	0.52	0.27	0.51	60	31.2	15.9	Constant Volume Isocon	-53.78	-49.04	-23.56
Na2O%	0.03	0.01	0.4	1	0.03	0.01	0.67	-63.72	-60	-40
K2O%	0.02	0.01	0.5	1	0.02	0.01		-54.65	-50	-25
TiO2%	0.01	0.01	0.4	1	0.01	0.01		-63.72	-60	-40
P2O5%	0.33	0.18	0.54	60	19.8	10.65		-51.21	-46.21	-19.32
MnO%	0.02	0.02	0.75	1	0.02	0.02		-31.97	-25	12.5
Cr2O3%	0.01	0	0.75	1	0.01	0		-31.97	-25	12.5
Ni_PPM	56	42.5	0.76	1	56	42.5		-31.16	-24.11	13.84
Sc_PPM	1.5	0.75	0.5	1	1.5	0.75		-54.65	-50	-25
LOI%	0.55	0.3	0.55	1	0.55	0.3		-50.53	-45.45	-18.18
Ba	7	6	0.86	1	7	6		-22.25	-14.29	28.57
Be	0.75	0.5	0.67	1	0.75	0.5		-39.53	-33.33	0
Co	5.75	1.2	0.21	1	5.75	1.2		-81.07	-79.13	-68.7
Cs	0.05	0.13	2.5	1	0.05	0.13		126.76	150	275
Ga	1	0.98	0.98	1	1	0.98		-11.56	-2.5	46.25
Hf	0.05	0.05	1	1	0.05	0.05		-9.3	0	50
Nb	0.13	0.35	2.8	1	0.13	0.35		153.97	180	320
Rb	0.38	0.08	0.2	1	0.38	0.08		-81.86	-80	-70
Sn	0.5	0.5	1	1	0.5	0.5		-9.3	0	50
Sr	14.45	4.4	0.3	1	14.45	4.4		-72.38	-69.55	-54.33
Ta	0.05	0.08	1.5	1	0.05	0.08		36.06	50	125
Th	0.1	0.1	1	1	0.1	0.1		-9.3	0	50
U	0.25	0.05	0.2	1	0.25	0.05		-81.86	-80	-70
V	29.5	32	1.08	1	29.5	32		-1.61	8.47	62.71
W	2.5	2.35	0.94	1	2.5	2.35		-14.74	-6	41
Zr	2.75	2.4	0.87	1	2.75	2.4		-20.84	-12.73	30.91
Y	9.55	9.3	0.97	2	19.1	18.6		-11.67	-2.62	46.07
La	5.5	2.65	0.48	4	22	10.6		-56.3	-51.82	-27.73
Ce	8.9	4.45	0.5	1	8.9	4.45		-54.65	-50	-25
Pr	1.05	0.66	0.63	6	6.27	3.93		-43.15	-37.32	-5.98
Nd	5.25	3.15	0.6	2	10.5	6.3		-45.58	-40	-10
Sm	1.19	0.8	0.67	4	4.76	3.2		-39.02	-32.77	0.84
Eu	0.95	0.81	0.85	16	15.2	12.96		-22.66	-14.74	27.89
Gd	1.57	1.15	0.73	10	15.65	11.5		-33.35	-26.52	10.22
Tb	0.19	0.18	0.92	1	0.19	0.18		-16.46	-7.89	38.16
Dy	1.05	1.11	1.05	20	21	22.1		-4.54	5.24	57.86
Ho	0.23	0.24	1.02	16	3.68	3.76		-7.32	2.17	53.26
Er	0.61	0.72	1.18	10	6.1	7.2		7.06	18.03	77.05
Tm	0.08	0.1	1.33	12	0.9	1.2		20.94	33.33	100
Yb	0.5	0.6	1.21	10	4.95	6		9.94	21.21	81.82
Lu	0.07	0.08	1.14	20	1.4	1.6		3.66	14.29	71.43
Mo	1.15	1.35	1.17	1	1.15	1.35		6.48	17.39	76.09
Cu	11.95	2.3	0.19	2	23.9	4.6		-82.54	-80.75	-71.13
Pb	0.6	0.65	1.08	1	0.6	0.65		-1.74	8.33	62.5
Zn	11.5	3.5	0.3	2	23	7		-72.39	-69.57	-54.35
Ni	36.3	11.65	0.32	1	36.3	11.65		-70.89	-67.91	-51.86
As	2.1	1.35	0.64	1	2.1	1.35		-41.69	-35.71	-3.57
Sb	0.35	0.4	1.14	1	0.35	0.4		3.66	14.29	71.43
Au	0.25	0.83	3.3	1	0.25	0.83		199.32	230	395
Se	0.25	0.25	1	1	0.25	0.25		-9.3	0	50

	Hematite Ore Breccia (D2001 & D2014)	Ore Breccia + Chlorite (S3014, S3010, & D004)	slope	scale	Scaled Data (D2001 & D2014)	Scaled Data (S3014, S3010, & D004)		% Change Constant Mass	% Change Constant Volume
SiO2%	0.58	2.2567	3.89	4	2.32	9.03		289.08	271.39
Al2O3%	0.23	1.69	7.35	10	2.3	16.9		634.78	601.38
Fe2O3%	98.37	93.0867	0.95	0.2	19.67	18.62	Constant Mass Isocon	-5.37	-9.67
MgO%	0.015	0.83	55.33	10	0.15	8.3	1	5433.33	5181.82
CaO%	0.265	0.31	1.17	40	10.6	12.4	Constant Volume Isocon	16.98	11.66
Na2O%	0.01	0.0167	1.67	1	0.01	0.02	1.05	66.67	59.09
K2O%	0.0075	0.0083	1.11	1	0.01	0.01		11.11	6.06
TiO2%	0.005	0.0317	6.33	1	0.01	0.03		533.33	504.55
P2O5%	0.1775	0.2	1.13	40	7.1	8		12.68	7.55
MnO%	0.015	0.0533	3.56	1	0.02	0.05		255.56	239.39
Cr2O3%	0.0045	0.006	1.33	1	0	0.01		33.33	27.27
Ni_PPM	42.5	64.3333	1.51	1	42.5	64.33		51.37	44.49
Sc_PPM	0.75	3.3333	4.44	1	0.75	3.33		344.44	324.24
LOI%	0.3	1.4667	4.89	1	0.3	1.47		388.89	366.67
Ba	6	7.3333	1.22	1	6	7.33		22.22	16.67
Be	0.5	1.5	3	1	0.5	1.5		200	186.36
Co	1.2	8.9333	7.44	1	1.2	8.93		644.44	610.61
Cs	0.125	0.0667	0.53	1	0.13	0.07		-46.67	-49.09
Ga	0.975	2.6667	2.74	1	0.98	2.67		173.5	161.07
Hf	0.05	0.25	5	1	0.05	0.25		400	377.27
Nb	0.35	1.2167	3.48	1	0.35	1.22		247.62	231.82
Rb	0.075	0.05	0.67	1	0.08	0.05		-33.33	-36.36
Sn	0.5	0.8333	1.67	1	0.5	0.83		66.67	59.09
Sr	4.4	7.3667	1.67	10	44	73.67		67.42	59.81
Ta	0.075	0.1167	1.56	1	0.08	0.12		55.56	48.48
Th	0.1	0.1667	1.67	20	2	3.33		66.67	59.09
U	0.05	0.0667	1.33	20	1	1.33		33.33	27.27
V	32	49.6667	1.55	1	32	49.67		55.21	48.15
W	2.35	1.4	0.6	0.6	1.41	0.84		-40.43	-43.13
Zr	2.4	9.7333	4.06	1	2.4	9.73		305.56	287.12
Y	9.3	36.8333	3.96	2	18.6	73.67		296.06	278.05
La	2.65	5	1.89	1	2.65	5		88.68	80.1
Ce	4.45	8.4667	1.9	6	26.7	50.8		90.26	81.61
Pr	0.655	1.0967	1.67	4	2.62	4.39		67.43	59.82
Nd	3.15	5.6333	1.79	4	12.6	22.53		78.84	70.71
Sm	0.8	1.6233	2.03	2	1.6	3.25		102.92	93.69
Eu	0.81	1.2933	1.6	1	0.81	1.29		59.67	52.41
Gd	1.15	2.6067	2.27	1	1.15	2.61		126.67	116.36
Tb	0.175	0.4733	2.7	1	0.18	0.47		170.48	158.18
Dy	1.105	3.4067	3.08	10	11.05	34.07		208.3	194.28
Ho	0.235	0.8933	3.8	6	1.41	5.36		280.14	262.86
Er	0.72	2.84	3.94	10	7.2	28.4		294.44	276.52
Tm	0.1	0.39	3.9	6	0.6	2.34		290	272.27
Yb	0.6	2.28	3.8	6	3.6	13.68		280	262.73
Lu	0.08	0.3467	4.33	10	0.8	3.47		333.33	313.64
Mo	1.35	1.0333	0.77	1	1.35	1.03		-23.46	-26.94
Cu	2.3	2.1333	0.93	1	2.3	2.13		-7.25	-11.46
Pb	0.65	1.4	2.15	1	0.65	1.4		115.38	105.59
Zn	3.5	18.3333	5.24	1	3.5	18.33		423.81	400
Ni	11.65	38.4333	3.3	1	11.65	38.43		229.9	214.9
As	1.35	4.0667	3.01	1	1.35	4.07		201.23	187.54
Sb	0.4	0.4667	1.17	1	0.4	0.47		16.67	11.36
Au	0.825	1.0333	1.25	1	0.83	1.03		25.25	19.56
Se	0.25	0.25	1	1	0.25	0.25		0	-4.55